2021

Silicon-basedI nanostructures: Growth and Characterizations of Si2Te3 nanowires and nanoplates

Jiyang Chen

SILICON-BASED NANOSTRUCTURES: GROWTH AND CHARACTERIZATIONS OF Si_2Te_3 NANOWIRES AND NANOPLATES

by

Jiyang Chen

A Dissertation Submitted in Partial Fulfillment of the Requirements

for the Degree of Doctor of Philosophy

Major: Engineering

The University of Memphis

May 2021

Acknowledgements

First, I would like to thank my thesis advisor Dr. Thang Hoang, Professor in the Department of Physics and Materials Science at The University of Memphis. He reassures me when I have a dilemma. He consistently encourages and inspires me in terms of my research work and steers me in the right direction. I appreciate all his kind help. Without him, this thesis and all my work could not be done.

I would also like to thank my thesis committee members Dr. Xiao Shen, Dr. Jingbiao Cui, Dr. Ranganathan Gopalakrishnan, and Dr. Gladius Lewis for their insightful comments and encouragement, which help improve my research and the quality of this thesis. Thanks also to Dr. Sanjay Mishra for his kind support and fruitful discussions through various experimental equipment and measurements.

I would like to thank my fellow students for their feedback, cooperation, and of course friendship.

Last but not least, I would like to thank my wife and my family for supporting me spiritually throughout writing this thesis and my life in general.

Preface

This dissertation is driven by the needs of a study of the emerging 2-D semiconductor nanomaterial Si_2Te_3.The study is established in both sample fabrications and the properties characterization.

- Aspects of text, figures and tables in Chapter 4 were published in AIP Advances, Volume 8, December 2018, 125008, titled 'Resistive switching in Si2Te3 nanowires' (https://doi.org/10.1063/1.5060675).
- Aspects of text, figures and tables in Chapter 5 were published in J. Applied Physics, Volume 125, January 2019, 024306, titled 'Probing the dynamics of photoexcited carriers in Si2Te3 nanowires' (https://doi.org/10.1063/1.5053932).
- Aspects of text, figures and tables in Chapter 6 were published in Scientific Reports, November 2020, 19205(2020), titled 'Anisotropic optical properties of single Si2Te3 nanoplates' (https://doi.org/10.1038/s41598-020-76265-1).

Abstract

Recent advances in materials science have enabled the fabrication of nanostructured semiconductors with one, two or three reduced dimensions. These nanomaterials have a number of new interesting properties and functionalities which do not exist in their macroscopic counterparts. In this research project, we focus on the investigation of the structural, electrical and optical properties of nanostructured silicon telluride (Si_2Te_3), which is a new class of layered nanomaterial with unprecedented structural variabilities. In a Si_2Te_3 semiconductor compound, the Te atoms are hexagonally close-packed while Si atoms form Si-Si dimers and fill two-thirds of the allowed sites in-between the packed Te atoms. It has theoretically been predicted that several possible orientations of Si-Si dimer could lead to strikingly different structural, electrical and optical properties of Si_2Te_3 nanostructures.

Various Si_2Te_3 nanostructures including vertical, titled, and horizontal nanoplates, nanoribbons, and nanowires were fabricated by using the chemical vapor deposition technique. The structures, compositions of various Si_2Te_3 nanostructures are being investigated by electron microscopy, X-ray photoelectron emission, energy dispersive X-ray spectroscopy. Optical properties of these nanostructures are being investigated by polarized micro-photoluminescence, Raman and reflection measurements at different temperatures and excitation powers. Electrical switching properties of single Si_2Te_3 nanowires are investigated by using electrochemical method.

We expect to develop a comprehensive understanding of properties of Si_2Te_3 nanostructures and to provide useful information on using these new nanomaterials as building blocks for optoelectronic and chemical sensing.

Table of Contents

List of Figures

Chapter 1. Introduction

Introduction to low dimensional materials

In the past few decades, hundreds of novel nanostructured materials have been demonstrated. Physical characteristics such as a large surface area/volume ratio and reduced dimensionality of nanostructured materials ultimately affect the materials' properties and performances. Indeed, nanostructured materials have been becoming increasingly important and have attracted a great interest from both the fundamental research community and industrial sectors. A major feature that discriminates various types of nanostructures is their dimensionality. Pokropivny and Skorokhod [1] have proposed a modified classification scheme for nanostructured materials, in which zero-dimensional (0-D), one-dimensional (1-D), two-dimensional (2-D), and three-dimensional (3-D) materials are clarified. Traditionally, 0-D, 1-D, and 2-D nanostructures are associated with quantum dots, nanowires, and nanoplates, respectively. According to Pokropivny and Skorokhod, nanostructured materials can be broadly classified by the number of their nanoscopic dimensions. Figure 1 shows example scanning electron microscopic (SEM) images of different dimensional materials. In this thesis, we will focus our studies on 1-D and 2-D forms of silicon telluride (Si_2Te_3) nanostructures.

(a) 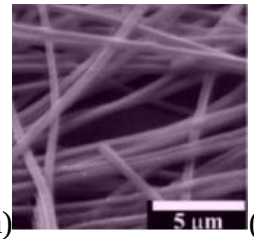

(b) 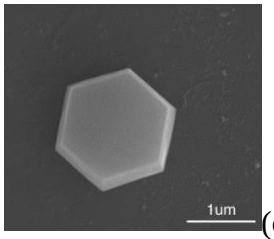

(c) 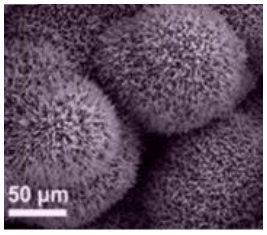

Figure 1: Example SEM images of materials at different dimensions (a) 1-D nanowires [2]. (b) 2-D nanoplates. (c) 3-D structures [3].

Introduction to 1-D and 2-D structures

Widely accepted threshold for a material to be termed as nano is smaller than 100 nm in at least one dimensional [4]. 1-D nanostructured materials are defined such that two dimensions of the materials are nano-sized while the third dimension can extend to micrometer length scale [5], such as nanoribbons, nanotubes and nanowires. 1-D nanostructured materials are ideal systems for exploring a large number of novel phenomena at the nanoscale and investigating the size dependence of functional properties. They are also expected to play an important role for both interconnects and building blocks in fabricating electronic [6], optoelectronic [7], and electrochemical energy devices with nanoscale dimensions. 1-D nanostructured materials such as carbon nanotubes have attained a significant attention after the pioneering work by Iijima [8]. Indeed, 1-D nanostructured materials have profound impacts on fundamental understandings as well as potential applications in future generations of electronic and optoelectronic devices.

2-D materials are classified as very thin materials with single layer or several layers of atoms, which have become one of the most intensive research areas in the field of materials science in recent years due to their unique structures and properties. 2-D nanostructured materials constitute a unique class of materials in which the atomic layers are weakly bonded together by the van der Waals interaction [9]. Indeed, the weak van der Waals interaction between layers may allow a great flexibility for the integration of different materials without the limitation of the lattice mismatch. Due to few surface dangling bonds, 2-D materials exhibit excellent electronic properties that are not readily achieved in semiconductors of other forms.

The study of 2-D materials began with the birth of graphene. In 2004, graphene was first demonstrated by the A.K. Geim et al. through the 'ripping tape' method, which quickly triggered a global research craze on 2-D materials [9]. As a 2-D material, graphene has a hexagonal honeycomb structure composed of carbon atoms in a single proton in the form of sp^2. Graphene is a fundamental component of several allotropes of other carbons [10]. For example, graphene can stack layer by layer to form 3-D graphite. Moreover, a rolled graphene can form a 1-D carbon nanotube. Also, the winded and closed graphene can create a spherical structure named as fullerene or buckyball (0-D). Due to its excellent electrical conductivity and ultra-thin atomic layer thickness, graphene has the potential to be widely used in transparent electrodes. For this reason, the graphene could be used to replace semiconductors such as indium tin oxide, which significantly improves the flexibility, ductility, and foldability of devices [11]. Compared with indium tin oxide, graphene offers a lower production cost and an easier mass production of transparent conductive electrodes for GO/rGO. These properties have attracted researchers' interest tremendously.

After the discovery of the graphene, many other new 2-D materials have also been discovered, such as boron nitride, transition metal dichalcogenides (TMDCs), and black phosphorus. More importantly, these new classes of semiconductor layered materials have electronic bandgap energies ranging from ultra-violet (UV) to near infrared which make them attractive for many applications in nano-electronic and nano-photonics.

At present, 2-D TMDCs with a medium bandgap are the most widely studied, and its photoelectric response band covers the visible band and near-infrared band [12]. For example, the transition metal sulfide such as molybdenum disulfide (MoS_2), which is a semiconductor material that has hexagonal crystal structure. The material can be synthesized into a variety of

inorganic structures, such as single-armed nanotubes [13], multi-armed nanotubes [14], and variety thickness nanosheets [16]. The bandgap of MoS_2 layered structure varies from 1.2eV to 1.9eV, which matches the energy of visible light and promises potential applications for photovoltaics [17]. The monolayer structure of MoS_2 shows a direct bandgap and results in a high luminous efficiency, which has a critical application prospect in the solar cell and photoelectric fields [18]. In 2011, the federal institute of technology in Lausanne, Switzerland, predicted the MoS_2 monolayer is to be used in the manufacture of smaller and more efficient electronic chip. Since 2011 MoS_2 monolayers have shown great advantages in the nanoelectronics applications. Indeed, it is expected to play a great potential in nanotechnology such as nanoscale transistors [19], light-emitting diodes [20], and solar cells [21], etc… On the other hand, because MoS_2 has a much lower mobility than that of graphene. Therefore, MoS_2 is often used in combination with graphene in practical applications [22][23][24][25].

In addition to MoS_2, boron nitride (h-BN) is also a new class of 2-D insulator material. The 2-D h-BN has a hexagonal cellular planar structure of alternating nitrogen and boron atoms [26], which is similar to the graphene structure. The bandgap of boron nitride is as high as 6.0 eV [27], and its photon emission is in the ultraviolet band [28]. Therefore, as distinct from graphene, h-BN can be used as an excellent insulator. Indeed, this material is commonly used as a dielectric layer in complex circuits. By combining with other 2-D materials, the optical and electrical properties of the device are enhanced. For example, growing graphene films on the h-BN surface will effectively improve the mobility of carriers in graphene [29][30][31]. Because of the deep ultraviolet band response and its superior chemical

stability, h-BN has a great potential application as an anti-oxidation coating and superhydrophobic [32].

Recent advanced research has also discovered several other classes of 2-D materials and they are not yet fully explored. Exploring their unique electrical and optical properties will lay out a foundation understanding and lead to next device generations with exotic properties and functionalities. For instance, transparent electrodes are essential components of photoelectronic devices such as solar cells, light-emitting diodes, and electronic displays.

In this thesis we study Si_2Te_3 nanoplates (NPs), which are emerging as a new class of 2-D layered semiconductor. Depending on synthesis conditions, the layered Si_2Te_3 nanostructures could form 2-D NPs or nanowires by the stacking of many NPs along the z-axis.

Fabrication of 1-D materials

As mentioned previously, 1-D nanostructured materials are classified such that two dimensions of the materials are reduced to nanometer size while the third dimension can extend to micrometer scale. The primary morphologies include nanotubes, nanorods, nanowires, and nanobelts. Recently, various methods have been reported to fabricate 1-D nanomaterials, such as arc discharge method, chemical vapor deposition method, laser sputtering method, and template method. These methods are briefly discussed in the sections below.

Arc discharge method

Arc discharge method is the most original method used to prepare carbon nanotubes. It can also be used to prepare other 1-D nanomaterials. For example, the fabrication of carbon nanotubes involves two different sizes of graphite precursor rods which are placed in an inert

gas reaction chamber filled with absolute pressure. The massive surface area of the larger rod is the cathode, and the small rod is the anode. The distance between the two poles is approximately one millimeter. From an original report, Ebbesen et al. fabricated nanotubes at a direct current of 100 A, a voltage of 18 V, and the fabrication pressure at 66650 Pa. A large number of carbon nanotubes are obtained in the discharge method [33].

Chemical vapor deposition method

Chemical vapor deposition (CVD) method usually refers to the process of chemical reaction and condensation of reactants to produce specific products. It has commonly been applied to synthesize both the 1-D and 2-D materials. A detailed CVD method will describe in the 2-D materials fabrication below. For 1-D nanomaterial fabrication, the CVD method is also related to a vapor-liquid-solid transition process.

In an earlier work by Yang et al., MgO and carbon powders were used to fabricate MgO nanowire arrays [34]. In such a case, both the precursors are load into a graphite boat, placed inside a tubular furnace and heated the mixed powders to 1200℃ under the protection of a high purity flowing Ar gas. The generated MgO vapor was transported to the nanowire growth zone far away from the mixed powders by the flowing Ar gas, and aligned MgO nanowires grown directly on a substrate. In another work by Zhang et al., where Si nanowire fabrication was demonstrated [35]. The annealed 95% Si and 5% Fe precursors were placed in a quartz tube. An Ar gas as the carrier gas was introduced into the quartz tube in one end and pumped out on the other end at a constant rate. After the whole system was kept at 1200 ℃ for 20 hours, hundreds of micrometer long Si nanowires were successfully fabricated.

Laser sputtering method

Laser sputtering method is also a vital method to prepare 1-D nanomaterials. The laser sputtering equipment includes a laser source, condenser, target, tube furnace, cooling ring, vacuum pump, and airflow valve. Laser sputtering is initially used to prepare carbon nanotubes. It also be used to prepare various 1-D nanomaterials, such as BN nanotubes, Si nanowires, and other semiconductor nanowires. Yang et al. have reported the fabrication of Si nanowires by using the pulse laser evaporation method [36]. The high energy pulsed laser beam with wavelength of 248 nm was used to bombard a mixed powder target, which contains Si, Fe, Ni, and Co precursors. Si nanowires were obtained with a diameter of 15 nm and length from tens to hundreds of micrometers.

Liquid phase synthesis method

Liquid phase synthesis is also known as the wet chemical method. It is a combination of the hydrothermal synthesis, the solvothermal method, and the microemulsion method. The liquid phase synthesis method has a reasonable control over the nucleation, growth, and size limitation of the crystal. In the liquid phase reaction, a high concentration of reaction liquid precursors will be conducive to the precipitation of heterogeneous nuclei with a high stability. Liquid phase synthesis can also diversify the products by changing solvents and introducing suitable surfactants. For example, Khusaimi et al. synthesized ZnO nanorods in an aqueous solution by using gold nanoparticles as seeds on a silicon substrate [37]. It is found that the concentration of zinc ions in the solution greatly influences the crystal size and growth orientation of the nanorods.

Fabrication of 2-D materials

Several fabrication methods of 2-D materials are categorized as physical and chemical synthesis processes. Common methods include mechanical exfoliation [38], chemical

exfoliation [39], and chemical vapor deposition [40][41]. Sections below briefly describe these methods.

Mechanical exfoliation

Because of the weak Van der Waals force that bonds layers of the 2-D materials, the mechanical exfoliation method refers to the use of external mechanical force or kinetic energy to peel off a monolayer or a few-layers of 2-D thin films from their bulk materials. In practice, the "tape stripping" method [38] is commonly employed to peel off 2-D thin films.

Indeed, the first ever discovered 2-D materials, graphene, was demonstrated by Geim and Novoselov et al. by using the mechanical exfoliation from graphite precursor [9]. The authors concluded that monolayer graphene was produced by repeatedly sticking the scotch tape on the bulk material. This procedure is illustrated in Figure 2. The layered structures prepared by this mechanical exfoliation method has a very low defect density and excellent quality. This is useful for studying fundamental physical properties of graphene, in particular, and 2-D materials in general. At present, the maximum size of graphene prepared by the mechanical exfoliation method is as large as 100 μm in lateral size [39]. On the other hand, the mechanical exfoliation method also poses a limitation in industrial applications due to a challenge from the large-scale production.

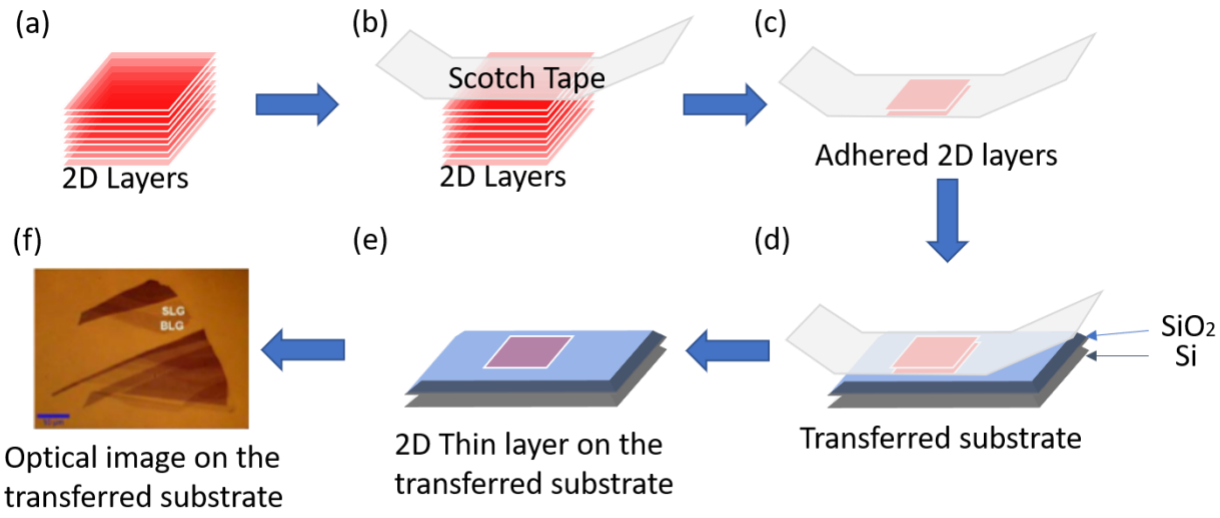

Figure 2: Illustration of mechanical exfoliation technique to fabricate 2-D materials. (a) 2-D material layers stacked to form bulk material; (b) A scotch tape is applied to the top of the layered-structure; (c) Few-layers 2-D structures adhered on the scotch tape; (d) The scotch tape then transfers 2D layers to substrate; (e) Left-over 2-D layers after removing the scotch tape; (f) Optical image of the graphene monolayer on the transferred substrate [42].

After the graphene was successfully exfoliated, many other research groups have also successfully prepared other 2-D material films such as MoS_2 [43] and WeS_2 by using the scotch tape technique [44].

Chemical exfoliation

The chemical exfoliation method typically uses a solution with metal ions which have a small atomic radius to intercalate 2-D materials' neighboring layers. After intercalation, the atoms can break the weak van der Waals force between the neighbor layers. This method is illustrated in Figure 3. The chemical exfoliation processes for different 2-D materials could be different. For example, graphene oxide (GO) monolayer or a few-layer structures can be produced by oxidizing and interlacing graphite [45]. The weak van der Waals force between graphene layers will be dominated by strong oxidants such as concentrated sulfuric acid and nitric acid. After several simple processes such as sonication, centrifugation, and washing, a uniform GO solution can be obtained. The oxygen-containing functional groups carried on the

surface can then be removed by a variety of cutting agents. The various size and quality GO can be prepared by controlling the conditions during the reaction. In another example of TMDCs, a neutral solution containing lithium-ion or magnesium-ion is used for intercalation [46]. In such a case, thin layers of TMDCs are obtained after a series of processes involving sonication and centrifugation.

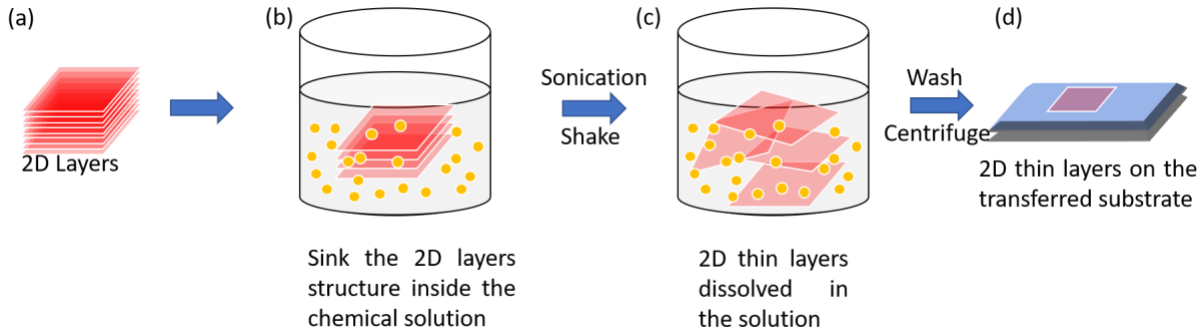

Figure 3: Illustration of chemical exfoliation to synthesis 2-D materials. (a) 2-D materials layers stacked as a bulk material; (b) Bulk material is placed in a chemical solution where small diameter ions can intercalate into the layers; (c) The van der Waals force between the neighboring layers is broken by sonication and shaking process, hence, thinner layers are dissolved into the chemical solution; (d) After washing and centrifugation process, 2-D layered structures are spin coated on to a new substrate.

Chemical vapor deposition

The CVD can also be used to produce high-quality 2-D materials. Excellent crystallinity and large-area thin film are the main advantages of the materials prepared using the CVD method. The 2-D materials can be successfully grown by heating precursors, which transforms the target atoms into vapor phases and then deposit them on to a substrate. This method can be applied to a wide range of sources, including gases (such as acetylene for graphene growth [47] and sulfur vapor for MoS_2 growth [48]), liquids (such as benzene for graphene growth [49]) and solid precursors (such as molybdenum oxide for molybdenum

disulfide growth [50]). Metals or silicon-based materials are commonly used as substrates for the synthesis process because they are stable at high temperatures. At present, the most common substrate materials are monocrystalline silicon (Si) and silicon dioxide (SiO_2). However, the selection of different substrates may vary. For example, studies show copper substrates can easily be used to produce graphene monolayers. During preparation, the process stops when a layer of graphene is deposited on the copper foil. Besides, the copper substrate requires relatively low carbon source, pressure, and temperature in the preparation process [51]. Because the CVD method can produce a relatively small number of defects, large surface area of 2-D materials, it has been widely applied in micro-electronic devices fabrication. Indeed, it is the most promising 2-D material preparation method. However, the CVD method also shows several drawbacks in thin-film manufacturing. For example, the use of CVD process requires strict control of the pressure during preparation and lacks the capability to introduce impurity atoms [40]. Moreover, the transfer of the generated materials is difficult, and the precursor's conversion rate is low. Expensive equipment, complex growth process, and a cumbersome transfer process are additional drawbacks of this method.

Potential applications of 1-D materials

The physical properties of a material form the basis for the material's applications. The unique physical and chemical properties of 1-D nanomaterials provide new opportunities to design new generations of devices that can transform traditional electronic products. 1-D nanomaterials show several unique properties that are suitable for applications requiring high ratio of surface area to volume, a substantial surface effect, and quantum effect. Also, they are sensitive to gas and have a low response to temperature. Particularly, 1-D metal oxides have high crystallinity [54][55], anisotropic crystal growth [56], and various crystal structures [57]

and morphologies [58]. The miniaturization and intellectualization of materials, high integration of components, high-density storage, and ultrafast charge transfer provide a broad range of applications of 1-D nanomaterials. Several specific applications of 1-D nanomaterials are introduced below.

High efficiency energy conversion device

Batteries with regenerative capacity are widely used in mobile phones, small household appliances, electric shavers, and micro-instruments. With the decrease in size of digital cells, their integration capability is growing rapidly, and instrument sizes are further reduced. At present, the size of a capacitor can be as small as nanometer scale and therefore the materials used for the components must also be in the nanoscale. This allows not only the high energy density of the battery but also further miniaturizes the battery size, which provides an opportunity for the application of 1-D materials in the battery field. In 1999, the composite 1-D nanostructured material was successfully developed as the working electrode of the lithium battery [59]. Such a working electrode provides an excellent conductivity so a high efficiency Li-ion battery can quickly charge and release.

Thermal catalysis

1-D metal nanostructures are very active and can be used as a combustion supporting agent in fuel. It can also be doped with high-energy-density materials, such as explosives, to increase explosion efficiency. In the same way, the 1-D metal nanostructures are also used as an initiator. Again, for 1-D nanomaterials the high surface-volume ratio can promote a high reaction efficiency. At present, 1-D Ag and Ni nanostructures have been used as combustion promoters in rocket fuel [60].

Lasing application of 1-D nanomaterials

1-D nanomaterials exhibit unique optical properties that can be used for nanophotonic components such as nano-lasers. For example, Huang et al. have successfully demonstrated a nanolaser by using ZnO nanowire arrays [61]. ZnO nanowires with a diameter of 20-150 nm and a length of about 10 μm were grown on a sapphire substrate by using the CVD method. At room temperature, these nanowires naturally form laser resonators. The interface between a nanowire and sapphire and the surface of the free end of the nanowire become reflection surfaces of the resonator. Under a pump laser excitation, the nanowires exhibit a lasing emission peak with a full width at half maximum of 17 nm. This initial work has attracted a tremendous attention and placed 1-D nanomaterials in a great potential for application in optoelectronics.

Furthermore, it has been demonstrated that by selecting nanowire materials of different electronic properties, it is possible to generate light emitting diodes (LEDs) that cover a broad band from ultraviolet to the near-infrared region.

Potential applications of 2-D materials

Recent research progress has demonstrated that 2-D semiconducting TMDs are promising candidates for a wide range of applications in micro- and nano-electronics [52], optoelectronics [53] and nanoelectromechanical systems [62] due to their intrinsic electronic and optical properties. Particularly, thin film TMDs show unique electro-optical properties because electrons are confined in a single layer. Moreover, several previous reports have demonstrated notable physical properties of these 2-D TMDs such as high carrier mobility [63], high current density [64], broadband optical absorption [65], high tensile strength [66] and reasonable thermal conductivity [67].

In the next paragraphs, we will discuss several applications of 2-D materials from their electronic and optical perspectives.

Potential electronic applications

At present, there are still several technical barriers preventing the use of 2-D materials in real-life applications such as the contact resistance [68] with metal electrodes and the Schottky barrier [69]. Nevertheless, here we will discuss the main physical properties of the 2-D materials with their potential applications.

Before the discovery of 2-D materials, the smallest possible high - performance transistor was 22 nm [70]. Even at that size, the performance of the device did not show a significant improvement related to the size reduction due to a limitation in the charge carrier mobility degradation. The newly discovered 2-D materials, on the other hand, show a reliable electrostatic control of the channel by the gate voltage with the thickness reduction down to single or several layers of atoms [71]. Indeed, in 2-D materials a high carrier mobility was demonstrated [72]. 2-D materials therefore hint at a possibility for ultrathin field effect transistors with extraordinary performances which can significantly boost the capabilities of future generations of electronic devices.

Digital electronics

Currently, complementary metal oxide semiconductors (CMOS) are widely used for digital electronics [73]. In practice, common digital electronics is designed by using billions of silicon metal oxide semiconductor field-effect transistors (MOSFETs) as the logical circuits. The key to a proper function of CMOS devices is the digital switching behavior.

Figure 4 (a) shows a simple sandwich structure which is composed of an array of crossbars. Once a potential between the electrodes increases to the supply voltage *Vs*, the current will be switched to a large value. The original current is called as the *off-state* current and the switched current is called as the *on-state* current. This phenomenon is referred as the switching behavior and the current switching and recover process are referred as set and reset, respectively. Figure 4 (b) and 4 (c) illustrate two typical switching behaviors by using 2-D TMDCs. In Figure 4 (b), the set process occurs when the positive potential applied from 0 to the *Vs* and the reset process occurs when the potential swaps back to 0 V. Both set and reset processes are shown when a positive potential applied. This switching behavior is referred as unipolar switching [74]. In another situation, as shown in Figure 4 (c) where the reset occurs when the potential swap to a negative value and the I-V measurement shows a symmetric change. This latter case is referred as bipolar switching [75].

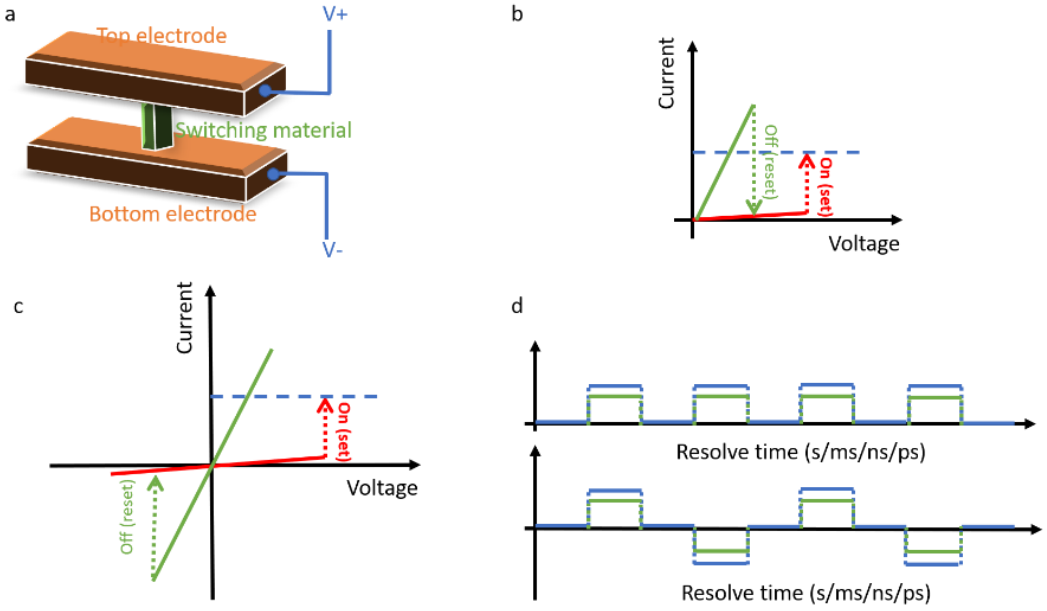

Figure 4: Switching behavior of digital electronics. (a) Sketch of the device; (b)-(c) two types of switching behavior for set and reset processes. (d) voltage scanning procedure for two switching behaviors shown in (b) and (c).

For any digital electronic application, the ratio of the on-state and off-state currents (I_{on}/I_{off}) and the switching speed between the set and reset processes are the two main considerations that influence a device performance. Typically, the reported on/off current ratio for 2-D materials is between 104 and 107 [76]. It is important to emphasize that such a current ratio can only be achieved for the semiconductor with a wide enough bandgap of at least 400 to 500 meV [77]. Furthermore, the fastest switching speed could be resolved in pico-seconds for 2-D materials [78]. The switching behavior of 2-D materials therefore could be applied to electronic devices such as transistors and memory devices.

Later in this thesis we will investigate electronic properties of the Si_2Te_3 nanomaterials. Our result indicates a significant switching behavior of Si_2Te_3, which promises potential applications of this material for electronic nanodevices.

Semiconducting 2-D field-effect transistors

The field-effect transistors (FETs) are the basic building blocks of modern electronic devices. All electronic devices such as computers and mobile phones are built base on working principle of FETs. An FET is a voltage control device, and its function is determined by two specific parameters. The gate-source voltage (V_{GS}) and the drain current (I_D) (as illustrated by Figure 5). In principle, the I_D is the current that flows through the channel between the drain and source electrodes, which is controlled by the V_{GS}. The current I_D flows through width-varying path, which is caused by the change of the reverse deviation of the PN junction and an expansion of the depletion layer. In the unsaturated region of V_{GS}=0, the expansion of the depletion layer is not very large. As V_{GS} increases the depletion layer extends from the gate to the drain hence I_D becomes saturated because part of the channel is being blocked.

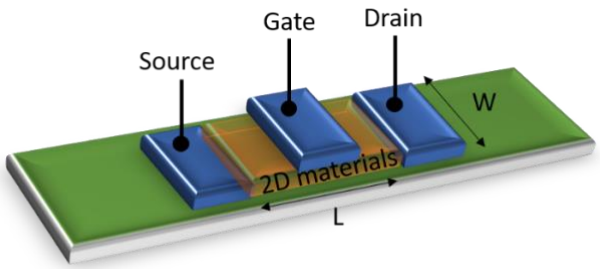

Figure 5: Schematic of a FET device. There are gate, drain, and source terminals, which roughly correspond to the base, collector, and emitter of bipolar transistors [75].

In the last few decades great efforts have been made to improve the speed and miniaturization of FETs. However, when the channel length is reduced to a few nanometers, the performance of silicon-based transistor devices is reduced significantly. Compared with traditional silicon, the 2-D semiconductors, with their wide range of band gap energies, show great potential as next-generation channel materials. Graphene, the first discovered 2-D material, does not fulfill requirements of FETs because of the zero bandgap, large I_{off} and the I_{on}/I_{off} ratio is less than 10 [79]. On the other hand, other 2-D TMDs materials such as MoS_2, WSe_2 show suitable electronic bandgaps in the range from 1 to 2 eV, which have a potential that they behave as switches with low I_{off}. A recent study has shown that a MoS_2-channel FET can offer a large I_{on}/I_{off} ratio up to 10^4 [80].

Radio frequency electronics

Radio frequency (RF) electronics has long been an application of FETs. Recently, 2-D semiconductor materials have been applied to RF electronics as well as analog devices [81]. The benefits from the ultra-thin and the dangling bonds in 2-D materials could help reduce the gate length the FETs down to 1 nm [82]. A schematic of an RF electronic device which bases on the FETs is shown in Figure 6. Unlike an original requirement for digital applications of

the FETs, the RF electronics does not require a large I_{on}/I_{off} ratio but rather focuses on the transit frequency (f_T) and the maximum oscillation frequency (f_{max}).

The f_T is expressed as

$$f_T = \frac{g_m}{2\pi C_G}$$

and the f_{max}

$$f_{max} = \frac{f_T}{2\sqrt{\frac{R_G+R_S}{r_d}+2\pi f_T R_G C_{GD}}}.$$

where g_m is the transconductance, R_G is the gate resistance, R_s is the source resistance, R_D is the drain resistance, C_G is the gate capacitance, C_{GS} is the gate to source capacitance and C_{GD} is the source to gate capacitance. The main point to improve the ability of an RF transistor is to increase the oscillation frequency and reduce the dimensional size of its electronics.

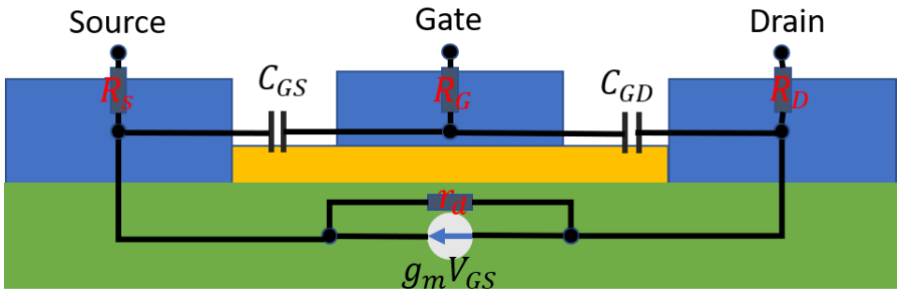

Figure 6: Schematics of a 2-D MOS transistor.

Recent studies of 2-D materials in RF electronics have paid attention to graphene and MoS_2. An initial work has shown the transit frequency f_T of the graphene-based RF transistor could excess 400 GHz [83]. In any case, the gapless property of graphene results in a limitation in the saturation behavior of the current in an RF device. The current saturation in

the RF device limits the voltage and the power gains. Therefore, the maximum oscillating frequency f_{max} is less than f_T, and the performance of the graphene-based RF devices is less than expected. On the other hand, 2-D MoS_2 semiconductor shows excellent intrinsic properties for FETs. The exfoliated monolayer MoS_2 FETs reduce the thickness of the device to 1 nm scale. The mobility of the MoS_2 monolayer is exceeding $80(cm^2/Vs)$ [84], and the direct bandgap result in a promising voltage gain. The electron saturation velocity for MoS_2 monolayer structure is theoretically predicted to be greater than $3 \times 10^6\, cm/s$[69]. Based on these properties, a sub-micrometer channel length of MoS_2 FETs is sufficient to afford the f_T in GHz frequency range. It has also been shown a transit frequency f_T of 2 GHz and f_{max} of 2.2 GHz at a 240 nm MoS_2 gate length [85].

Potential optical applications

Novel 2-D materials hold various exotic optical properties, such as the number of layers associated with light absorption, photoluminescence, Raman spectroscopy, and nonlinear optical response processes. As the number of layers increase, the peak emission energies, intensity, and linewidths of these spectra may vary. Various new optical features may emerge, which relates to the layer thickness. When the incident excitation power is low, the 2-D materials will exhibit linear optical properties. However, when the 2-D layered materials are exposed to a high incident excitation power, the high-order nonlinear effects of the 2-D materials occur. In practice, the third-order nonlinear optical response process is the most common and easy to be excited. Here, we will introduce the linear and non-linear optical properties of the 2-D layer materials. We will also discuss several significant applications of the 2-D materials from their optical property perspective.

Linear optical properties

The linear optical properties are the main characteristics of 2-D materials, such as the refractive index and absorptivity of the materials in the event of low power light (such as a laser) excitation [86]. The light intensity of the incident laser is weak and does not have enough influence to trigger high-order optical nonlinear effects in the materials. In such a case, the response of the materials to excitation is proportional to the intensity of the excitation and therefore it is referred to as linear. In this case, the properties of 2-D materials will mostly depend on the compositions. As an example of a linear response: the refractive index of a 2-D material, which is an important optical parameter to for potential applications in nano-photonics, may vary significantly under the influence of external electromagnetic fields of different wavelengths. Thus, a systematic study of the linear optical properties of 2-D materials with different structures will deepen our fundamental understanding as well as provide a guide to potential applications of materials.

Several electronic properties of 2-D materials such as field-effect, anomalous quantum hall effect, tunable conductivity and other electronic properties have extensively been studied. However, the basic optical properties, especially the refractive indices, are still less studied. The problem is mainly due to the very thin cross section of the 2-D materials (only a few atomic layers) and the substrate is often scattered so there is not yet an effective way to characterize their refractive indices.

Non-linear optical properties

2-D materials have become a promising class of non-linear optical materials due to their sizeable non-linear polarity rate, ultra-fast optical response, and high optical input threshold. Significant attention has been paid to their potential applications in optical limiting devices. The optical limiting effect usually refers to a saturate behavior of the linear

relationship between the output and the input light intensities. When the incident light intensity reaches a certain threshold, the output light intensity increases slowly and becomes saturated. Therefore, it is necessary to have two critical factors: the first is to be stimulated by an intense light, and the second is that the material must have a specific non-linear response ability. The several most common non-linear phenomena include second and third harmonic generations, frequency conversion processes such as four-wave mixing, sum of frequencies and saturable absorption in the 2-D materials [87]. The non-linearity is a vital performance parameter in optical communication and saturable absorber applications.

Photocatalysis applications

The application of semiconductors in photocatalysis technology has been applied widely. Semiconductor photocatalysis offers stable chemical properties, substantial oxidation-reduction, no adsorption saturation, long service life and low cost. Indeed, semiconductor materials have become an important research topic in the field of photocatalysis as hydrogen production by photo-hydrolysis of water and photocatalytic degradation of dyes. Recent discovered 2-D layered nanomaterials also hold benefits for photocatalysis applications because of dimensional reduction. For example, a larger surface area in 2-D materials may provide more sites for catalytic reactivity. Excellent mechanical properties can ensure the continuity of catalysis. High thermal conductivity allows for thermal diffusion in the reaction. Compared with the instability or low activity of the traditional photocatalysts in water during visible light irradiation, these 2-D materials are more stable and have higher catalytic activities. Additionally, 2-D materials have a wide range of tunable bandgaps, which depend on the number of atomic layers. The wide range of band gap energy therefore permits a wide

range of absorbable light wavelengths, which significantly boosts the photocatalytic efficiency.

The photocatalytic efficiency of many 2-D materials may be affected by recombination processes. For example, 2-D phosphorene has a tunable bandgap in the range 0.3~2.29 eV [94] and can absorb photons from visible light to infrared wavelengths. However, the photo-generated electron-hole pairs have a relatively high recombination rate, resulting in a poor catalytic performance. Another example is g-C_3N_4. g-C_3N_4, a material which has an excellent thermal stability up to about 600℃ and holds excellent chemical inertness to the acid, alkali, and organic solvents [89]. The low-cost and the high specific-surface-area indicates that g-C_3N_4 is a promising non-metal catalyst. However, g-C_3N_4 in practice exhibits a poor conductivity and lowered photocatalytic properties due to its large bandgap (2.7 eV) [90], a large contact resistance, and a high inter-band recombination rate. The last example is the MoS_2 layered material. 2-D MoS_2 can absorb light in a narrow wavelength range and cannot make full use of sunlight. It also has high catalytic activity only at the edge, but no activity on the base surface. Therefore, a single-layer MoS_2 can only achieve a low photocatalytic activity [91].

Recently, novel composites of heterogeneous photocatalysis based on 2-D layered materials have widely been studied because they have large specific surface areas, tunable bandgap energy, and most importantly they inhibit photogenerated carriers from recombination. Recent research results show the photocatalytic activity of 2-D material heterostructures is higher than that of individual 2-D material components. By engineering the heterostructures, more efficient charge separation can be achieved. For example, a heterojunction between phosphenes and graphene not only effectively reconstruct the bandgap

alignment, but also significantly improve the photocarrier mobility of photocatalysts due to the high electron mobility of graphene. McCreery et al. have also investigated carbon nitride (g-C_3N_4)/ZrS_2 heterojunction, which shifts the light absorption edge from 550 nm to 350 nm (absorption edge of single-layer g-C_3N_4), and demonstrated excellent catalytic performance as photodissociation of aquatic hydrogen [92]. Iqbal et al. have used MoS_2/CdS heterojunction by an in-situ assembly of stripped low-layer MoS_2 and CdS nanocrystals [99]. A hydrogen production performance study showed that the photoinduced charge was separated and transferred rapidly in the heterojunction, which enhanced the photocatalytic hydrogen production activity. The hydrogen production rate reached 140 $\mathrm{mmol\ g_{CdS}}^{-1}\mathrm{h}^{-1}$, and the quantum yield at 420 nm was 66% [93]. The above studies show that 2-D materials heterojunction photocatalyst is an effective way to improve the catalyst's photocatalytic activity and will play an essential role in the field of photocatalysis.

Photodetector applications

Photodetectors are widely used in various fields of military and commercial products. The working principle of photodetectors relies on a change in the conductivity of a materials upon a light absorption. The three main steps of working photodetector are:

1) charge carriers are generated by incident light

2) transport of charge carriers

3) charge carriers generate current signal.

The leading indicators to evaluate a photodetector are quantum efficiency, light sensitivity, photoconductive gain, light/dark current ratio and response time.

The unique crystal structure of 2-D materials allows them to form flexible ultrathin films. Because of their atomic thicknesses, 2-D materials can easily be charged by static electricity, and its optical response characteristics can be tuned. Therefore, in recent years, 2-D materials have been widely used in optoelectronic devices. For example, the response speed of a WSe_2 monolayer based detector can reach ten picoseconds, which is suitable for high-speed photodetection. The response of a MoS_2 transistor can reach 880 A/W, which can also become a high-response detector. Further, a TMDC such as WS_2 has advantages of tunable bandgap, high carrier mobility, and proper band alignment which can be used to suppress the dark currents in mixed light detectors. 2-D nanostructured perovskite materials also exhibit high photoluminescent efficiency [94], quantum size effect, long electron diffusion length, and more considerable exciton binding energy [95]. These characteristics make them highly competitive for potential applications in optoelectronic devices. On the other hand, like photocatalysis application, 2-D materials with atomic thickness have a high transmittance rate, which makes them inefficient in term of light absorption. As an example, graphene detectors can be used for photoelectric detection, but its response rate is relatively low [96]. TMDC compounds have a high response rate. A newly discovered class of TMDC materials is black phosphorus which has a potential to achieve a high response rate. Black phosphorus has a bandgap that can be tuned over a wide range depending on the numbers of atomic layers and has been demonstrated to have practical applications for infrared frequency detection at room temperature [97]. Finally, as before, a large-scale production of high quality 2-D materials can pose a challenge.

Background of Si_2Te_3 nanostructures

Si_2Te_3 was first studied in 1953 [137]. During the following two decades, several groups investigated the physical properties of the bulk Si_2Te_3 such as the crystal structures, electrical, thermal, and optical properties. [99] [100] [101] [102] [103] [134] [135] [137]. Nanostructured Si_2Te_3 was not studied until 2015. Ploog firstly clarified the Si_2Te_3 crystal structure by measure the X-ray diffraction for a 0.54 × 0.40 × 0.12 mm bulk material [99]. Si_2Te_3 exhibits a layered, trigonal crystal structure with lattice constants a = 7.429 and c = 13.471 Å [98]. The Te atoms form a hexagonal close packed lattice and the Si atoms appear to form dumbbells (or dimers) between Te layers [99]. The crystals yield an easy cleavage plane that is perpendicular to the c axis, due to a weak bonding between those Te layers where no Si atoms are placed. The lattices of the Si_2Te_3 structures are shown in Figure 7 (a). Four possible orientations of a Si dimer are shown in Figures 7 (b) - (e). Figures 7 (b) – (d) show the Si dimer orientations parallel to one of the three [1000] directions in three different angles, Figure 7 (e) shows the out-of-plane orientation along the c-axis direction. Additionally, in Si_2Te_3 only ¼ of the Si dimers take the c-axis direction. The other ¾ of the Si dimers are oriented as shown in Figure 7 (b) – (d). The variability of the Si dimer orientations lead to different physical properties as we will demonstrate in this thesis.

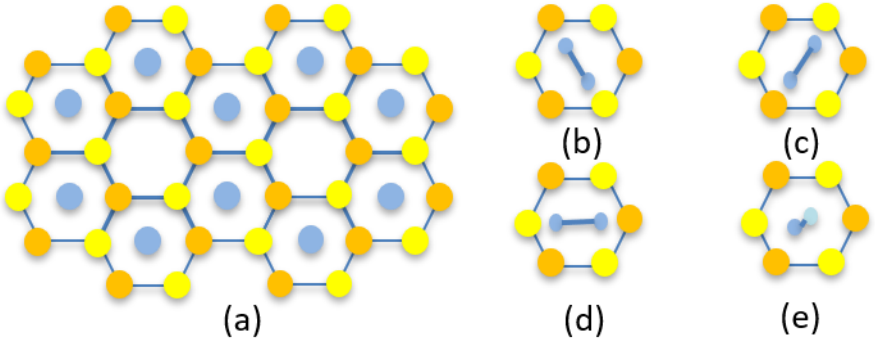

Figure 7: Crystal structure of Si_2Te_3. (a) Top view of hcp Te layers: (b-e) Four possible orientations of the Si-Si dimers, shown in blue. (b-d) In-plane orientations: Si dimer is parallel to one of the three [1100] directions. (e) Out-of-plane orientation.

Several studies during the 1970s showed that bulk Si_2Te_3 appeared to be a p-type semiconductor with indirect or direct electronic band structures [100]. Rau and Kannewurf initially reported the essential chemical stability of the Si_2Te_3 single crystal [134], then proved by Erlandsson and Birkholz by using an Auger spectrometer [135]. The surface of single-crystal Si_2Te_3 would react with water vapor then decompose into SiO_2 and Te. The decomposition process of the Si_2Te_3 could be directly observed by using an optical microscope. A clean sample surface appears in red color and shows semi-transparent, then has a metallic grey surface due to decomposition. The reaction formula is:

$$Si_2Te_3 + H_20 \rightarrow 2SiO_2 + Te + 2H_2Te + 2H_2$$

Hence, the single-crystal Si_2Te_3 is not stable in the atmosphere and lacks the protection technique. Literature report for this intrinsic material is relatively limited. Indeed, only a few groups have reported fundamental properties of intrinsic Si_2Te_3.

In 1976, Ziegler and Birkholz performed a thermoelectric measurement of the bulk Si_2Te_3 and reported that the hole concentration at 400K is 10^9 cm^{-3} [102]. The hole mobility of the bulk Si_2Te_3 parallel or normal to the c-axis is 10^{-2} $cm^2V^{-1}s^{-1}$ and 10^2 $cm^2V^{-1}s^{-1}$, respectively, which define Si_2Te_3 as a p-type semiconductor material. Bauer and Birkholz have reported fundamental electrical properties of Si_2Te_3 single-crystal [103]. Direct current (DC) conductivity and alternating current (AC) conductivity of the bulk Si_2Te_3 sample were measured at various temperature ranges. Si_2Te_3 shows an ohmic behavior at low electric fields and non-ohmic behavior at higher electric fields. The non-ohmic behavior is related to the conductance switching, which relates to the Si-Si dimer orientations. Indeed, this switching behavior has motivated us to investigate electrical properties of low dimensional Si_2Te_3 nanostructures. Furthermore, Bauer and Birkholz observed that the intrinsic carrier activation

energy changes from 1.04 eV to 1.43 eV for a temperature transition at 620 K, which is a result of the activated carrier mobility due to a hopping process. Zwick and Rieder investigated the optical absorption properties of bulk Si_2Te_3 and yielded a direct band-gap energy of 2.13 eV at room temperature and 2.34 eV at 4.2 K [101]. Ziegler and Birkholz also investigated the photoelectric properties of bulk Si_2Te_3, and their photocurrent measurements showed a maximum absorption at 2.2 eV with a couple of other bands at 1.9 eV and 1 eV [102]. The photoexcited carrier dynamics and the trap density are first discussed by Ziegler and Brikholz [102], however, the result of their study is contradictory with the theoretical calculation. The conflicting result could be related to the complexity of the crystal structure of Si_2Te_3. In this thesis, we will investigate the carrier dynamics for the 2-D nanoplates and nanowires (Chapters 5 and 6) and relate to the Si-Si dimer orientation.

Since 1980s, a few groups have investigated various properties of Si_2Te_3 in both bulk and layered structures [97, 98, 99, 100, 101, 102, 103, 104]. Recently (since 2015), as motivated by Keuleyan et al. who report an experimental method to synthesize the layered Si_2Te_3 nanowires and nanoplates, several groups have revisited this Si_2Te_3 material [105, 106]. For example, Shen et al. have reported a theoretical investigation showing a tunable bandgap and band structures of layered Si_2Te_3 by changing the orientation of Si dimmers [107].

Motivation of the study in Si_2Te_3 nanostructures

As mentioned earlier, the Si_2Te_3 is highly susceptible to react with moisture in the air to produce SiO_2 and Te. The compound after the reaction does not create a protective layer on the sample's surface, preventing further reaction. Due to cost and the technical barriers, the protection of the Si_2Te_3 materials is hard to achieve. Hence, from 1953 to 2015 very few

reports on Si_2Te_3 were made. However, with protection techniques developed, several low-cost methods could protect these Si_2Te_3 nanostructures. The spin-coating of polymer film on the surface of these materials facilitated the study of electrical properties. A dense transparent oxide layer of zinc oxide or aluminum oxide is generated on the surface of the sample by atomic layer deposition for optical research. Also, samples can be stored well by placing them in a vacuum chamber or a glove box filled with nitrogen.

In 2015, the Sean group from Brown University successfully grew Si_2Te_3 nanomaterials of different sizes and shapes through the chemical vapor deposition method [105]. Hence, it brought this material into the existing family of nanomaterials. Despite this, there are still lack of groups involved in the study of this material. So far, only our research team and Sean's team have successfully conducted systematic studies on the growth of different shapes of Si_2Te_3 nanomaterials. The control of source temperature, substrate temperature, growth time, pressure, and gas flow rate can obtain 2-D nanosheets with different morphologies. 1-D Si_2Te_3 NWs were also synthesized similarly to 2-D NPs but with the use Au nanoparticles as catalysis [109].

Further, the Raman spectroscopic study showed the band edge emission of the 2-D Si_2Te_3 NPs [105]. Si_2Te_3 nanostructures such as Si_2Te_3 NPs can be grown at low temperature (~600^oC) and without use of Au catalysts and have a potential for Si-based CMOS-compatible devices. Substitutional doping and intercalation of the Si_2Te_3 2-D NPs were reported by Wang et al. [136]. Substitutional doping with Ge results in a lower band gap and alters the optical phonon modes, thus leading to strongly red-shift of the PL emission [136]. Intercalation with Ge leads to a sharp ultraviolet resonance at 4.3 eV [136]. The unique structural characteristics and chemically tunable platform of Si_2Te_3 nanostructures could be used to control the

physical characteristics of the materials for possible applications in optoelectronics and thermoelectric. However, recent research related to the Si dimer orientation and the property change related to dimensional decreases is discussed fairly.

In our research, two aspects are of most interest. First, the physical properties change as the function of the dimension reduction from the bulk material. For 2-D materials, the thickness decrease will bring about changes in different physical properties, such as MoS_2. The material's bandgap transit from an indirect bandwidth to a direct bandwidth from bulk material to a monolayer film structure. Second, most crucial point is the impact of the variety of Si dimer's orientation on the material properties. Si_2Te_3 has a unique crystal structure that compares with other semiconductor materials, and the orientation of Si dimer will also have a significant impact on the properties of this material. In 2016, Shen reported the electronic band gap of 2-D Si_2Te_3 varies from 1.6 eV to 1.8 eV depending on the Si dimer orientations [106], and different orientations can adjust the material band gap from an indirect band gap to a direct band gap. The adjust of the band gap is unique and not found in other 2-D semiconductor materials. Once the fundamental properties are controlled by adjusting the Si dimer orientation, Si_2Te_3 will have a good application prospect. In this study, we preformed the properties estimation of the Si_2Te_3 in various nanostructures. The material shows the potential to be applied to digital devices. For example, 1-D Si_2Te_3 nanowires with a uniform orientation can be used as resistance random access memory device. Although it was introduced in the previous paragraphs that 1-D nanowires can be used as hydrogenation and photocatalytic materials because of their huge area-to-volume ratio, considering the special chemical properties of Si_2Te_3 that react with H_2O, we don't think this is good application here. The 2-D large-area thin film can be used for optical sensors and solar cells.

Given many interesting properties and potential applications of Si_2Te_3 nanostructures, our focus in this work will be devoted to the experimental investigation of growth mechanisms as well as using various characterization techniques to develop a comprehensive understanding. Structural, electrical, electronic and optical properties of both Si_2Te_3 NWs and NPs will be explored. Several papers [108, 109, 110] were published and several related research projects are under way.

Chapter 2. Experimental techniques

Chemical vapor deposition method

Chemical vapor deposition (CVD) is a powerful method to synthesis low dimensional materials. Generally, a variety of precursor materials are placed in a vacuum reactor, and the solid precursors are vaporized through high temperature and low pressure. The reactions occur through carrier gases and deposit on to substrates. Low dimensional materials with different morphologies can be obtained by controlling precursors' temperature, substrate temperature, carrier gas pressure, flow rate, reaction time and catalysts. Due to its low-cost and simple operation, CVD is widely applied in industrial and research experimental settings [40].

In this work, the Si_2Te_3 nanostructures are grown by a single step CVD and tellurium and silicon powders are used as precursors.

Scanning electron microscopy and energy dispersive X-ray spectroscopy

A scanning electron microscope (SEM) is a type of microscopic appearance observational method that lies between a transmission electron microscope (TEM) and an optical microscope. When a very fine beam of high-energy incident electrons bombards a sample surface, the excited region produces a series of signal including secondary electrons, auger electrons, characteristic and continuous spectrum x-rays, backscattered electrons, transmitted electrons, and electromagnetic radiation in the region of visible, ultraviolet, and infrared light. By scanning the sample with the electron beam, various physical information can be collected [111].

Energy dispersive X-ray spectroscopy (EDS), generally used as a part of the SEM. It is an element content analysis instrument to obtain the composition and content of the sample

by analyzing the characteristic X-rays generated by the electron beam bombardment on the sample surface. It is mainly used to analyze the composition of the elements in the test materials. The advantages of this method are fast speed analysis and simple operation. It can be used as an auxiliary tool for SEM to carry out composition analysis without affecting the high resolution. A high-performance X-ray energy spectrometer can simultaneously conduct a quantitative analysis of a specific test point.

In this work, we use the SEM and EDS to visually characterize the morphologies of Si_2Te_3 nanomaterials under different growth conditions.

Optical spectroscopy

Optical spectroscopy is a powerful, non-destructive technique used to investigate electronic and optical properties of Si_2Te_3 nanomaterials. These include Raman spectroscopy, photoluminescence, time resolved photoluminescence, reflection and absorption spectroscopies.

Raman spectroscopy

Raman spectroscopy is a very important characterization method to determine crystal structures their vibrational modes. It relies on inelastic scattering, or Raman scattering of monochromatic light, usually from a laser in the visible, near infrared, or near ultraviolet range from a test sample. Laser photons interact with molecular/atomic vibrations, which result in phonons of different frequencies, and emerge as photons at different energies. The emerged photons can have a lower energy (Stock scattering) or higher energy (anti-Stock scattering), which are shown in Figure 8 [112]. In this work, we will only focus on the Stock Raman scattering processes.

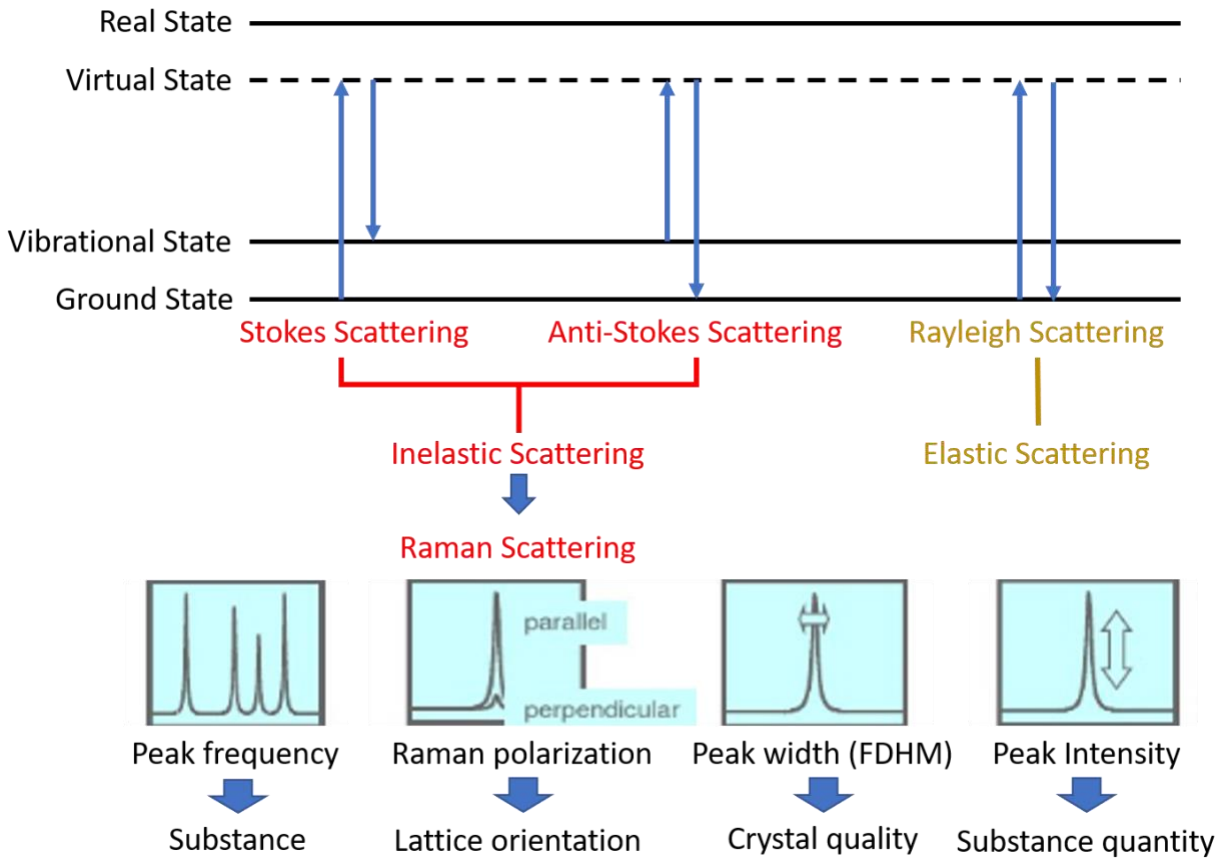

Figure 8: Sketch to illustrate Raman scattering processes. A Raman scattering profile from the sample would reveal physical properties of the material.

Photoluminescence spectroscopy

Photoluminescence (PL) spectroscopy, refers to a substance under the excitation of light where electrons are excited to the conduction band (of a semiconductor) leaving holes in the valence band. The electrons and holes reach the lowest unoccupied excited states (in the intrinsic semiconductors, these are the bottom and top of the conduction and valence bands) through various relaxation processes. Electrons and holes can bind together and form quasi-equilibrium states or excitons. After a short period of time (typically in the nanosecond range), electrons and holes recombine to emit photons and this process is regarded as PL emission. These emitted photons can have different frequencies due to different energy levels within a semiconductor and form an emission spectrum which can easily be detected using a

combined set of spectrometer and camera [113]. The PL measurement is a nondestructive test method, which can quickly and conveniently characterize the defects, impurities, electronic and optical properties of semiconductor materials.

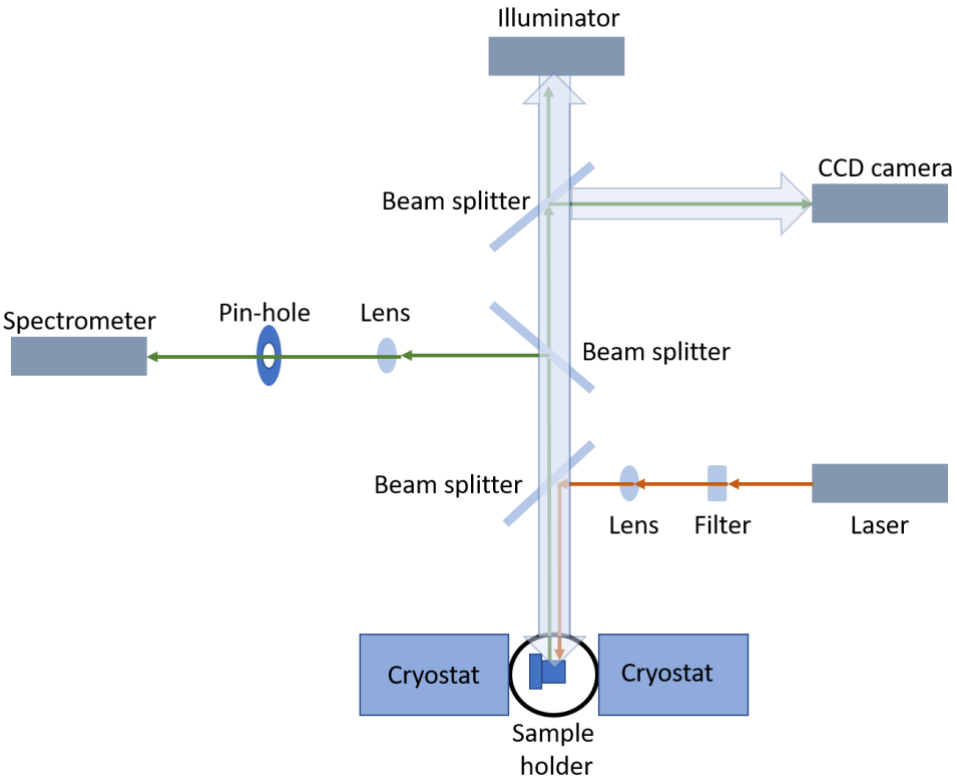

Figure 9: Schematic of a set up for PL measurements. The sample is placed in the cryostat and could be cooled down from room temperature to 7K.

UV-Vis spectroscopy

The UV-Vis spectroscopy analysis is an effective method to study the composition, structure, and substances of materials, which is according to the measurement of the absorption spectrum [114]. The semiconductor materials hold varieties of the molecular, atomic, and lattice structure. The materials will selectively absorb a specific wavelength or energy of external radiation. The absorption wavelength is directly related to the energy level transition and the molecular vibration. Therefore, each substance will have its particularly fixed absorption spectrum curve when different wavelengths of light pass through the object.

The semiconductor material absorbs photons with energy higher than its bandgap. The absorption spectrum of the materials can be processed by measuring the absorbance of the incident light at different wavelengths. The lattice structure and content of the materials can be studied according to the absorption spectrum's characteristics, such as peak strength, wavelength position and bandwidth.

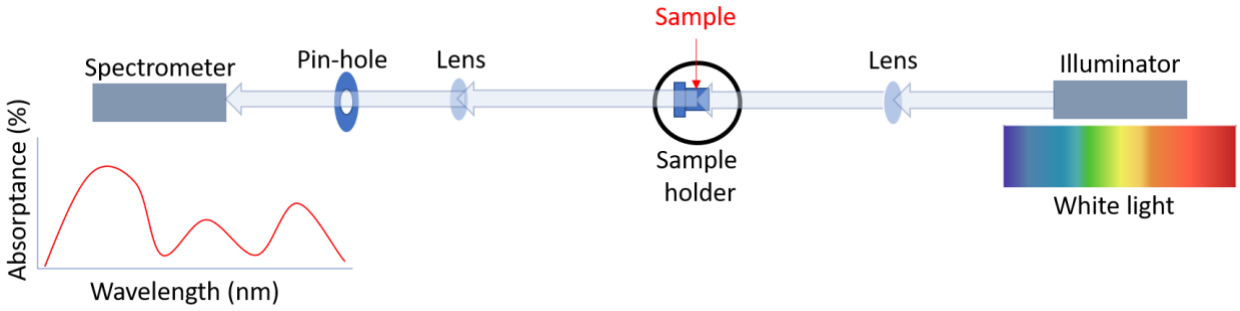

Figure 10: Schematic of a set up for the UV-Vis spectroscopic measurement. The sample is synthesized on the transparent substrates, such as glass, quartz, and sapphire.

Reflection spectroscopy

The reflection spectroscopy analysis is a special type of the UV-vis spectroscopy [115]. Once an incident light exposed on the sample, three processes can occur, which are reflection, transmission and absorption. In term of physical description, these parameters are mentioned as the reflectance (R), transmittance (T) and the absorptance (A), which are all presented in term of percentage of the incident light. The sum of the reflectance, transmittance, and the absorptance are equal to 1. In our study, the substrate is silicon or silicon oxide wafer hence the transmittance of the incident light is nearly zero and the sum of the reflectance and the absorptance should equal to 1. The physical mechanism is same as the UV-vis spectroscopy, deduct the reflectance of the sample would ratiocinate the absorptance.

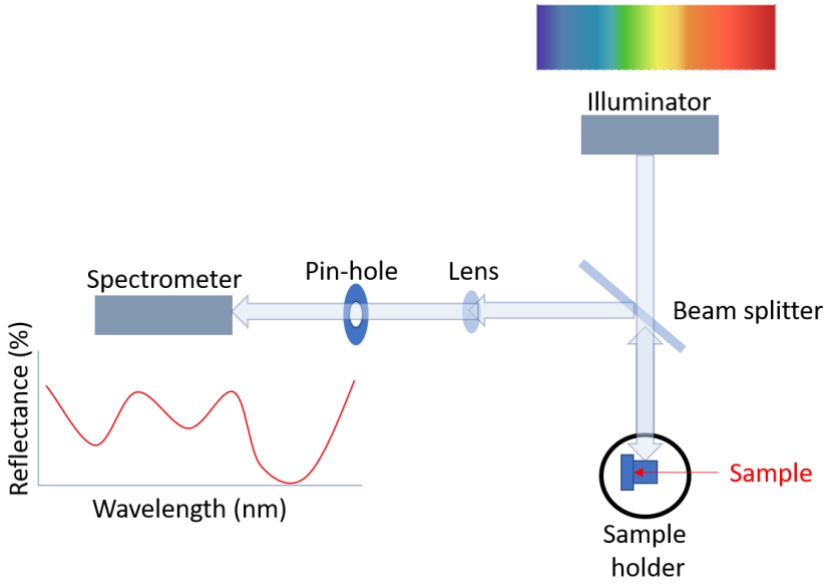

Figure 11: Schematic of a set up for a reflection measurement. The sample is synthesized on the opaque substrates, such as single crystal silicon, silicon oxide wafer or metal.

Single nanostructure spectroscopy

The confocal microscopy is employed in order to achieve individual sampling of single nanostructures. The mechanism is magnifying the collected image from the sample through one or more lenses and then refocusing the image through an intermediate plane where a small pin hole is placed. The pin hole allows one to select a single nanostructure at a time for further analyzing. The obtained image and spectrum of a single nanostructure can be directly observed through an imaging camera or stored in a computer. Figure 12 illustrates the working principle of an optical setup for single nanostructure measurements.

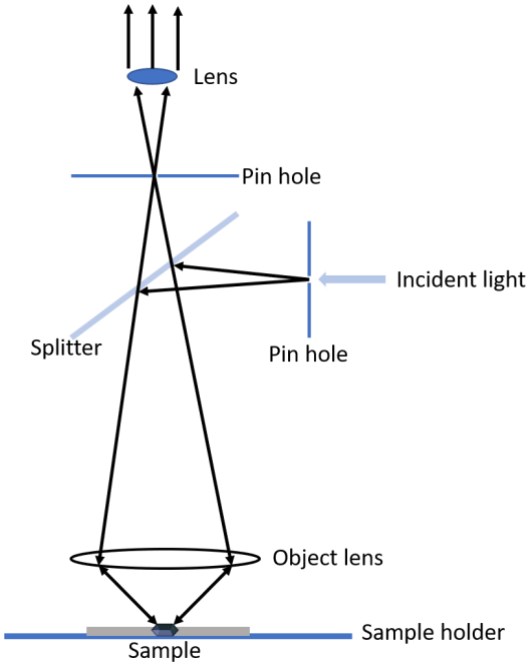

Figure 12: Schematic of the set up for a confocal spectroscopic measurement.

Nevertheless, the single nanostructure spectroscopic technique still be limited by the optical diffraction limits which is approximately around 300 nm for a typical visible light source. However, this limitation does not affect our measurements for Si_2Te_3 samples. The length of the synthesized nanowires is a few tens of micrometers, and the diameter of nanoplates is also a few tens of micrometers.

Polarization spectroscopy

The polarization spectroscopy is a spectroscopic technique based on the polarization of the light. Polarization spectroscopy is not an independent spectroscopic measurement technique [116]. It is associated with common spectrometric measurements, such as the Raman spectroscopy, UV-Vis spectroscopy, and PL spectroscopy. In our study, with polarizers added to optical paths, we can analyze polarization spectra of light emitted from samples, such as the polarized PL spectrum, polarized Raman spectrum, and polarized

reflection spectrum. Two typical types of measurements are employed for the polarization spectroscopy.

1) Excite a sample by a polarized incident light and then collect a corresponding emission spectrum.

2) Excite the sample by an unpolarized incident light, then collect emission spectra from the sample in polarized states.

Figure 13 illustrates a setup for polarization spectroscopic measurements.

Recent studies have revealed that 2-D materials exhibit unique anisotropic optical properties due to their crystal structures. For example, the polarized-Raman spectrum and polarized-PL spectrum of the 2-D MoS_2 [117], ReS_2 [118], WS_2 [119] materials all reveal the anisotropic optical behavior which relates to their crystal structures. Therefore, the polarization spectroscopy measurements are important to understand optical and electronic properties of the 2-D materials.

In our study, we employed the polarized-reflection and the polarized-Raman measurements to investigate the anisotropic dielectric constants and the Si-Si dimer orientations, which are directly related to the Si_2Te_3 crystal structures.

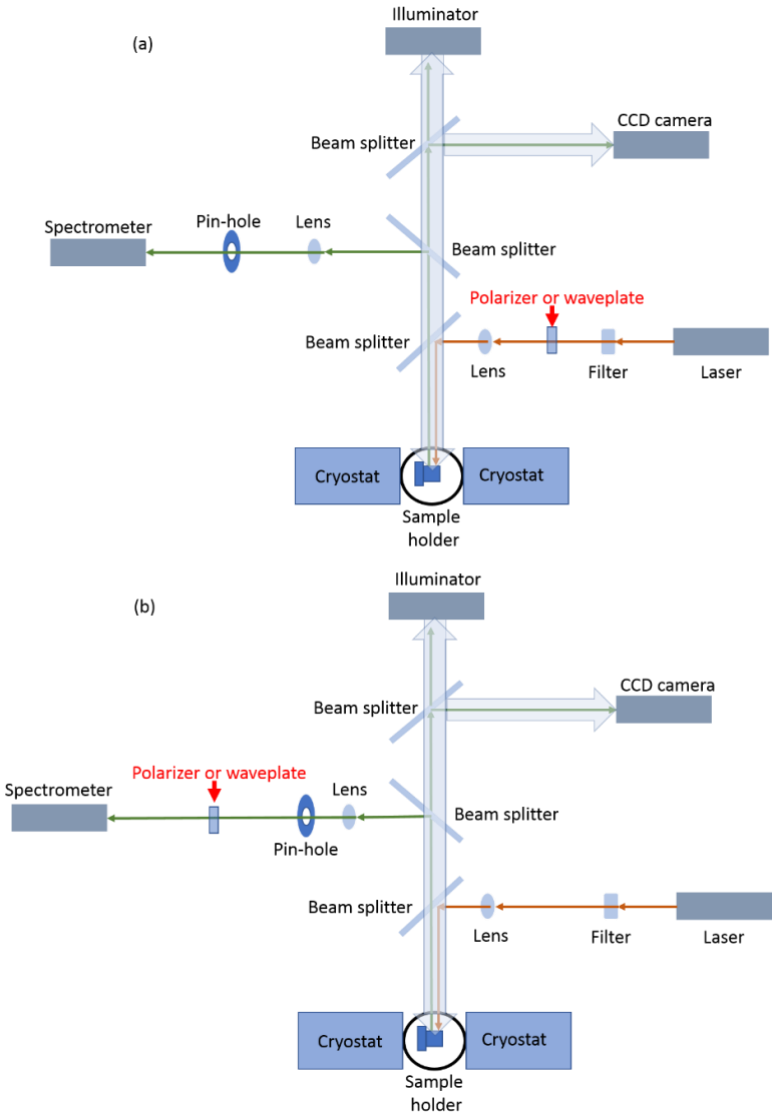

Figure 13: Schematic of a polarization spectroscopic setup. (a) Excite a sample by a polarized incident light and then collect a corresponding emission spectrum. (b) Excite the sample by an unpolarized incident light and then analyze the emission spectrum for different polarization components.

Time-resolved spectroscopy

Time-resolved spectroscopy is a spectroscopic technique used to observe the relationship between physical transient processes and time. In this method, the sample is exposed using a very short pulsed light source, and the photon emission is collected in each short pulse period. The emission photons are measured in an extremely short period, with the order of nanosecond (1 nanosecond $=1\times10^{-9}$ seconds) or picosecond (1 picosecond $=1\times10^{-12}$

seconds). In a typical time-resolved spectroscopic setup, a short-pulsed laser source is used for the excitation and a photon counter module is used for timing analysis.

Time-resolved spectroscopy is widely employed to study various physical and chemical processes such as energy transfer between molecules, internal electron transfer in molecules, dynamical processes of chemical reactions, and fundamental processes in photobiology. These processes are typically happening in a concise time range and hard to observe by the other techniques. Furthermore, another advantage of the time-resolved spectroscopy is a minimal damage to the measured sample. Hence, this spectroscopic technique can be employed to study both liquid and solid samples.

As mentioned in the previous section (2.3.2), when a semiconductor is excited by a laser beam with photon energy higher than its bandgap, electrons in the valence band will be excited to the conduction band leaving holes in the valence band. Electrons and holes then interact with each other to form quasiparticles called excitons or electron-hole pairs, and the semiconductor is a non-equilibrium state. The non-equilibrium carriers then relax rapidly to the bottom of the corresponding bands through various scattering processes and finally emit PL at a specific time. Different time frames of emitted photons may be associated with different carrier dynamics that occur within the semiconductor. For two-dimensional semiconductor materials, both doping and defects greatly influence the PL spectral and carrier lifetime characteristics. Time-resolved photoluminescence spectroscopy can then be used to understand the carrier relaxation processes and the spatial diffusion.

For our study in this thesis, the time-resolved spectroscopy is used to understand the Si_2Te_3 nanomaterial's carrier dynamics at various temperatures and laser excitation powers.

X-Ray diffractometer

In this study, an X-ray diffractometer is used to investigate the structural properties of Si_2Te_3 nanostructures. An X-ray diffractometer uses of diffraction principle and accurately determine crystal structures, texture and stress of substances. The wavelength of the X-ray is in the order of the distance between the atomic planes of a crystal. The crystal can act as a space diffraction grating as an X-ray beam impinge. Scattered X-ray beam is detected and information about the crystal is elucidated. Specifically, the superposition of the diffracted waves causes the intensity of the rays to be constructive or destructive depending on the crystal directions. The crystal structures can be obtained by analyzing the diffraction results [120].

Atomic force microscopy

The atomic force microscopy (AFM) is making use the van der Waals force interaction between atoms to study the surface characteristics of non-liquid samples [121]. The force between the two atoms (one on an AFM tip and the other on the sample surface) will vary with the distance between them. The relationship between the force and the distance is illustrated in Figure 14 (a). When one atom is close to the other atom, the repulsion force of the electron cloud is greater than the attraction between the nucleus and the electron cloud. On the contrary, if two atoms are separated from each other for a certain distance, the repulsion force of the electron cloud will be smaller than the attraction force between the nucleus and the electron cloud. Therefore, the resultant force behaves as a gravitation force. In terms of energy, the distance between atoms and the interaction energy between atoms can also be verified by Lennard Jones formula [122].

$$E_{pair}(r) = 4\varepsilon[(\frac{\sigma}{r})^{12} - (\frac{\sigma}{r})^{6}]$$

ε and σ are the constants for a material. From this equation, the interaction energy between atoms on a tip and on the sample's surface with respect to the distance can tentatively be described by a curve as shown in Figure 14 (a). In a practical AFM system, the interaction between the AFM probe and the sample's surface is used to reconstruct the surface's morphology with a sub-nanometer precision. Figure 14 (b) schematic show how an AFM system work. The repulsion and attraction forces are employed in practice for two operational modes:

(1) Contact mode: a surface profile is constructed by changing of atomic repulsion force. The distance between the probe and the specimen is about several Å.

(2) Non-contact mode: a surface profile is constructed when the distance between the probe and the specimen is about tens to hundreds of Å (attraction force).

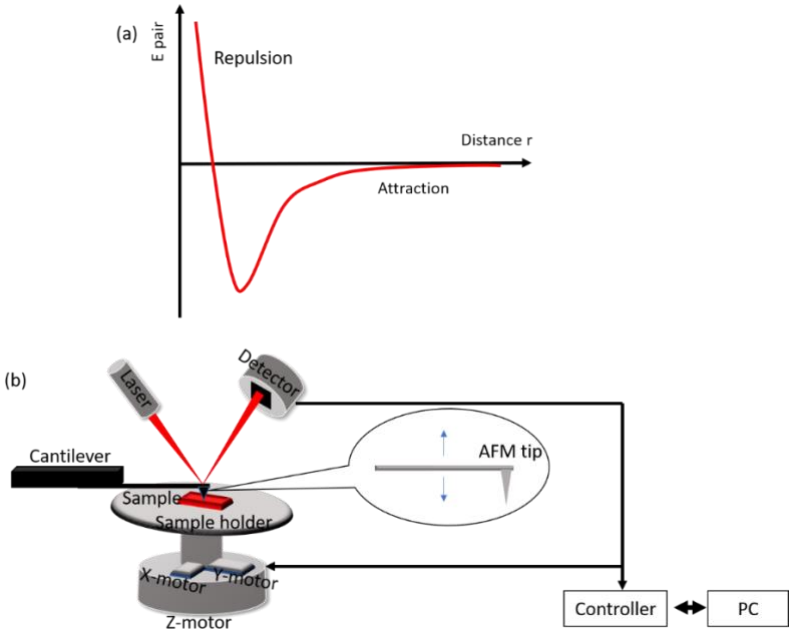

Figure 14: Working mechanism of the AFM. (a) Interaction energy between two atoms varies with the distance between them. (b) Sketch showing the working principle of the AFM.

Electrical contact measurements by using an electrochemical station.

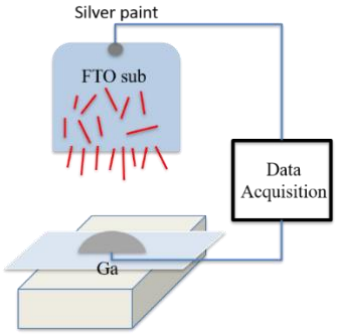

Figure 15: Schematic of an I-V measurement of single nanowires.

An electrochemical station is used to investigate the electrical properties of single Si_2Te_3 nanowires. A potential is applied to two ends of a nanowire and the current through the nanowire can be read out. By varying the applied voltage, an I-V curve can be obtained as schematically shown in Figure 15. As we will detail later, two different resistant states of Si_2Te_3 nanowires are demonstrated by scanning the applied voltages.

Chapter 3. Synthesis and morphology control of Si_2Te_3 nanostructures

The first step of this research project is the synthesis of the Si_2Te_3 nanostructures. Once Si_2Te_3 nanostructures are synthesized, characterization techniques are used to explore physical properties of a variety of morphologies of the Si_2Te_3 nanostructures. In this chapter, we will discuss in detail the synthesis of Si_2Te_3 nanoplates (NPs) and the nanowires (NWs) by using the CVD method.

NWs and NPs synthesized by the CVD method.

The CVD is a powerful technique to synthesize 1-D and 2-D materials. As one of the most popular synthesis techniques, the CVD technique is demonstrated to successfully fabricate graphene [123] and TMDC materials [124][125][126]. So far, several important parameters for the controlled growth of the 2D layered nanostructures are revealed, such as the carrier gases, precursors, growing temperatures and screw dislocation etc. [125]. A large number of 2-D layered nanostructures and their heterostructures, including MoS_2 [127][128] and graphene [129], have been successfully grown by the CVD method. For Si_2Te_3, which is an emerging TMDC, only a few groups have reported to successfully synthesize its nanostructures including NWs and NPs.

In this study, Si_2Te_3 NWs and NPs are synthesized in a 24-inches tube furnace (MTI 1200X) by using tellurium (30 mesh, 99.997%, Aldrich) and silicon powders (325 mesh, 99%, Aldrich) as source materials. Te and Si powders are placed in a ceramic crucible and loaded into the high temperature tube furnace. SiO_2/Si and Au coated SiO_2/Si substrates (spin coated with Au nanoparticles) are placed downstream of the nitrogen (N_2) gas flow in the furnace (Figure 16). The substrates are kept at 500 to 700 °C while the source materials are heated at 750 to 900 °C. N_2 gas is used as a carrier gas to keep the chamber pressure from the

mTorr to hundreds of Torr range. The N_2 flow rate is set by a mass flow controller from 15 sccm (standard cubic centimeters per minute) to 40 sccm for growing of various morphological structures. The furnace is then heated at a heating rate of 20 °C/min and the source heating distance is 6 inches apart. Before the furnace reaches the reaction temperature, the precursors are placed inside the quartz tube and far away from the heating area. As soon as the temperature reaches a desired value, the precursors are pulled into the heating area for the reaction and quickly cooled back to room temperature after the reaction is finished within a specific target time.

Tellurium vaporizes at relatively low temperatures (Tm = 450 °C) and to form Te_2. Si, on the other hand, does not vaporize (Tm = 1400 °C) at the temperature and pressure described above. However, Si can react with Te_2 vapor to produce SiTe which is carried by N_2 gas to the Si/SiO_2 substrates [95].

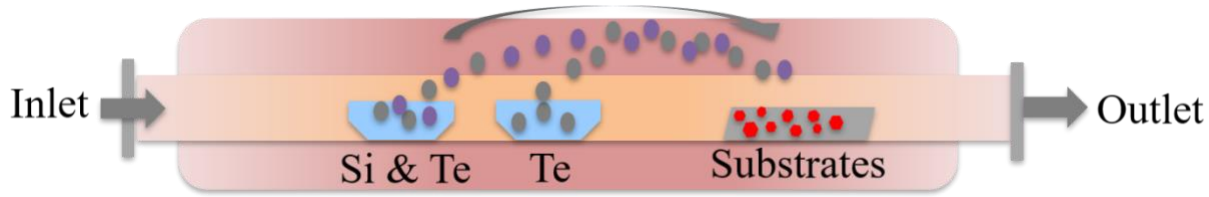

Figure 16: Schematic of the set up for Chemical Vapor Deposition method.

Morphological controls of NPs and NWs

The CVD synthesis process is determined by a matrix of parameters that influence different growth conditions and morphology of Si_2Te_3 nanostructures. For instance, precursor density, source temperature, nitrogen gas flowing rate, growing time, substrate temperature, and pressure inside the growing chamber are essential parameters to control the morphology.

Morphological control of Si_2Te_3 NPs by different growing parameters

As mentioned in the previous sections, the various morphological forms of Si_2Te_3 NPs can be synthesized by the CVD method. In the next paragraphs, we will discuss in detail each parameter's influence on the NP morphology.

Precursor selection for Si_2Te_3 NP synthesis

The precursor selection is the most important step in determining the reaction process inside the CVD furnace chamber. Recent works related to the synthesis of TMDCs such as MW_x (M is the transition metal precursor, the W is the chalcogenides, and the x is the ligand number for the substance) often choose MO_x (M oxide) or MCl_x (M chloride) as the transition metal precursor and the chalcogenide powder as the chalcogenide precursor. Similarly, for Si_2Te_3 tellurium power (Te), tellurium oxide (TeO_2), and tellurium tetrachloride ($TeCl_4$) are selected as tellurium sources, and the silicon (Si) powder is used as a silicon source [125].

The melting point for the TeO_2 is at 732^{o}C. The melting point for single crystal Si powder varies from 800^{o}C to 1500^{o}C for different meshes in ambient (smaller mesh has a lower melting point). In this study, 30 mesh Si powder is determined to offer a lower melting point for the reaction. It is noted that for temperatures from 800^{o}C to 1200^{o}C and pressures from 10^{-2} torr to 760 torr precursors will not react with each other to form Si_2Te_3 nanostructures. On the other hand, the melting point for Te powder is 449.5^{o}C. When the furnace is heated up to 800^{o}C, silicon will melt and react with tellurium vapor to form SiTe vapor, then SiTe reacts with a superfluous of Te vapor and adheres to the substrates to form Si_2Te_3. This explains the reason for mixing two precursors and loading into the furnace together as shown in Figure 16.

Another type of tellurium source is tellurium tetrachloride ($TeCl_4$), which is more difficult to use as a precursor to synthesis the Si_2Te_3 with a single step CVD process. $TeCl_4$ has a melting point at 224°C, and a boiling point at 380°C. The large temperature gap between melting points of tellurium and silicon precursors makes it hard to maintain the tellurium precursor inside the furnace during the whole heating process. A recent work by Kwak et al. [130] has demonstrated that Si_2Te_3 nanoplates can be synthesized by using the $TeCl_4$ precursor but must be accompanied by gold catalysts. This therefore is more complicated than the single-step CVD process.

In conclusion, in this study, tellurium and silicon powders are chosen to synthesize Si_2Te_3 nanostructures by using a single-step CVD.

Source and substrate temperature dependent NP morphology

Both the source and substrate temperatures are important parameters for the synthesis of the Si_2Te_3 NPs. Because of the single heating zone tube furnace used in our apparatus to synthesize NPs, a temperature change in the source materials from the center heating will cause a change to the substrate's temperature, too. The temperature zone designed for the source materials is from 750 to 900°C. However, the best temperature to complete the synthesis is from 800°C to 850°C. On the one hand, if the source temperature is lower than 800°C, the silicon powder cannot react with the tellurium powder to form SiTe, and therefore cannot react with the superfluous tellurium vapor to deposit Si_2Te_3. In such a case only tellurium deposits on the substrate as indicated by the SEM image in Figure 17 (a). If the source temperature is higher than 850°C, the vaporization process of the tellurium powder will be completed in few seconds and be pumped out as the exhaust. The melting process of

the silicon powder could not complete in such a short time frame, therefore, only tellurium could be observed on the substrate as indicated by the SEM in Figure 17 (b).

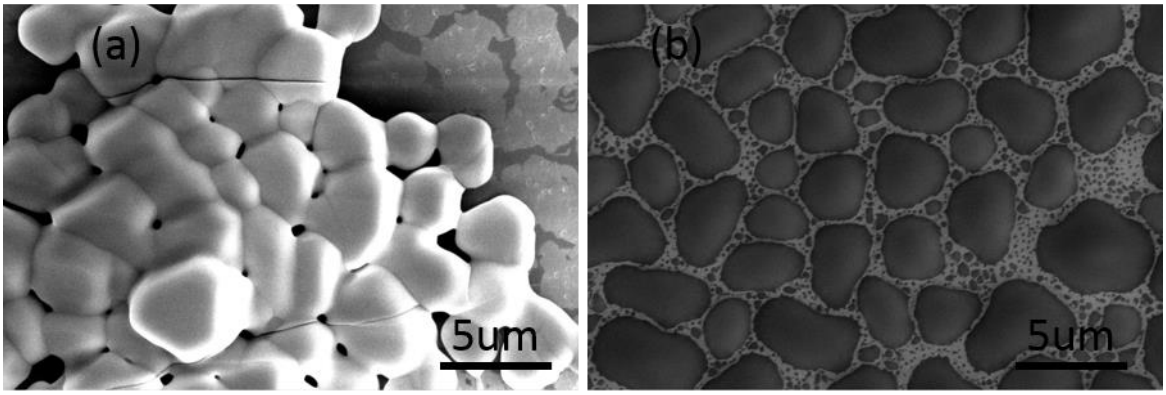

Figure 17: SEM images of samples grown at different precursor temperatures (a) At 750^{o}C precursor temperature, only tellurium deposits on the substrate; (b) At 900^{o}C precursor temperature, also only tellurium deposits on the substrate.

Figure 18 shows SEM images of nanoplates which were grown at various precursor temperatures and the substrate temperatures. All samples were synthesized at 25 sccm nitrogen gas flowing rate and 5 minutes growing period. The vertical direction shows the precursor temperatures at 800^{o}C, 825^{o}C and 850^{o}C and the horizontal direction shows the substrate temperatures from 800^{o}C to 600^{o}C and a 50^{o}C decrease for each step. When the precursor temperature is set at 800^{o}C, by varying the substrate temperature from 700^{o}C to 800oC, the flocculent structure deposited on the substrates are all tellurium. By decreasing the substrate temperature to 650^{o}C, ununiform Si_2Te_3 nanostructures develops on the substrates with size at around 200 nm. When the substrate temperature decreases further to 600^{o}C, very few tellurium powders adhere to the substrate. When the precursor temperature increases to 825^{o}C and 850^{o}C, the growth mechanism of the nanoplates is clearly revealed. With the precursor temperature increases from 800^{o}C to 850^{o}C, the silicon powder actively reacts with the tellurium to form SiTe vapor. For the substrate temperature higher than 700^{o}C, the superfluous tellurium vapor will deposit on the substrate and form liquid tellurium. When the

substrate temperature is lower than 700ºC, SiTe vapor sticks on the surface of the substrates in liquid form and then reacts with the tellurium to produce the Si_2Te_3 nanostructures. The flocculent structure deposits on the top of the nanoplates for substrate temperatures lower than 700ºC, and when the precursor temperature is higher than 825ºC, the superfluous tellurium vapor deposits during the cooling process.

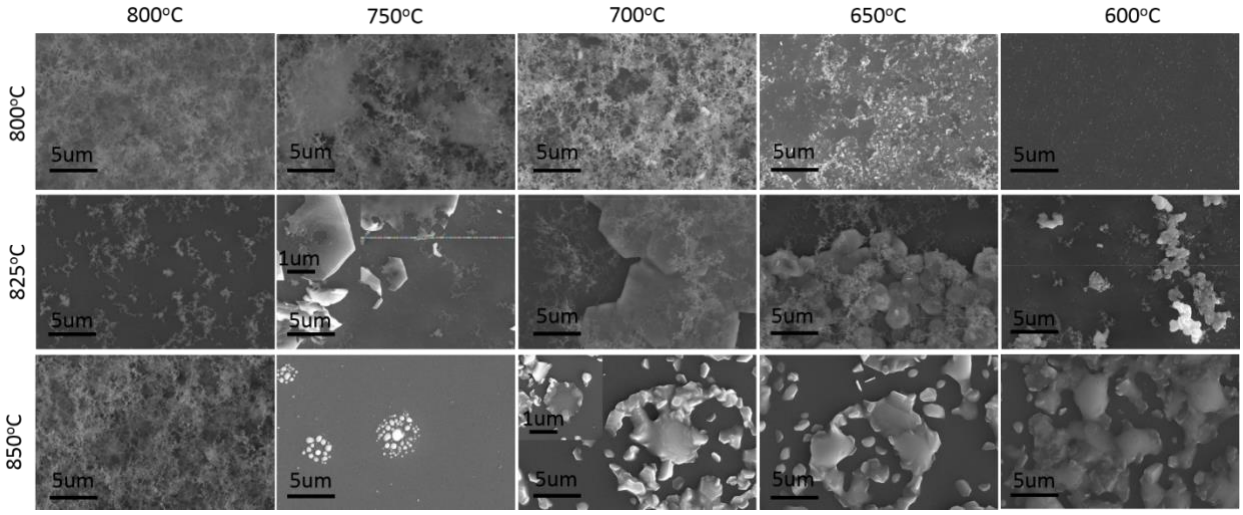

Figure 18: SEM images of different structures for various precursor and substrate temperatures. The vertical direction shows precursor temperatures at 800, 825 and 850ºC the horizontal axis shows substrates temperature from 600ºC to 800ºC with a 50ºC increment step.

Carrier gas flowing rate dependent NP morphology.

Figure 19 shows SEM images of NPs which were grown at two different flowing rates and the various substrate temperatures from 550ºC to 800ºC. The growing parameters for these two sets of samples were the same except the flowing rate. The vertical axis shows the substrate temperatures, and the horizontal axis shows the two flowing rates at 20 sccm and 25 sccm. These were two exceptional growing conditions in our study. Other flowing rates that were used to synthesis NPs were at 10 sccm, 15 sccm, 30 sccm, 40 sccm and 50 sccm. From SEM imaging studies, two groups of results were concluded from these flowing parameters.

Different morphologies of the nanoplates were observed for flowing rates below 20 sccm and above to 25 sccm. Detailed results are discussed below.

As shown in Figure 19, three interesting differences could be observed from these two groups of SEM studies. Firstly, when the substrate temperature is at 750^{o}C, a 25 sccm flowing rate only results in a poor tellurium deposition. However, a 20 sccm flowing rate results in small nanoparticles on the sample surface. These small nanoparticles do not always exhibit hexagonal shape. And, from EDS mapping of the SEM measurement, the atomic ratio of the Si and Te is higher than that for the sample grown at 25 sccm. This means that the silicon atomic ratio is larger for the 20 sccm flowing rate than that of the 25 sccm flowing rate. It is worth to note that the EDS mapping results might be influenced by the fact that the Si substrate might contribute to the atomic ratio. Secondly, for substrate temperatures at 700^{o}C and 650^{o}C, any difference in morphologies through the SEM imaging studies is not significant. For both cases, large and small NPs are observed, and these could be explained such as the substrate temperatures at 700^{o}C and 650^{o}C are more suitable for the growth of the Si_2Te_3 NPs. Indeed, within this temperature range the poor tellurium reacts with SiTe vapor to form as Si_2Te_3 NPs. In any case, there is a couple of differences for samples grown under these two different flowing rates that can be concluded from SEM images. The density of the large NPs for the 20 sccm flowing rate is higher than that the 25 sccm flowing rate, and the shape of the NPs grown at 20 sccm is sharper. Finally, when the substrate temperature decreases to 600^{o}C, only tellurium is deposited on the substrate for the sample which is grown at 25 sccm while for the 20 sccm flowing rate a large number of hexagonal NPs are observed on the substrate. The size of these NPs is around 500 nm in diameter and 100 nm thick.

At smaller flowing rates, the carrier gas relative speed inside the furnace is slower. Therefore, the transportation speed of the precursor is relatively slow which results in a longer reaction time between the SiTe vapor and the tellurium superfluous vapor. In such a case one could observe different morphologies of Si_2Te_3 nanostructures at various substrate temperatures. Moreover, the slow flowing rate is not suitable for synthesis of high density NPs due to a limitation of the vapor distribution over a large distance. Thus, in conclusion, the flowing rate affect both the morphology of Si_2Te_3 NPs including their size and density distribution.

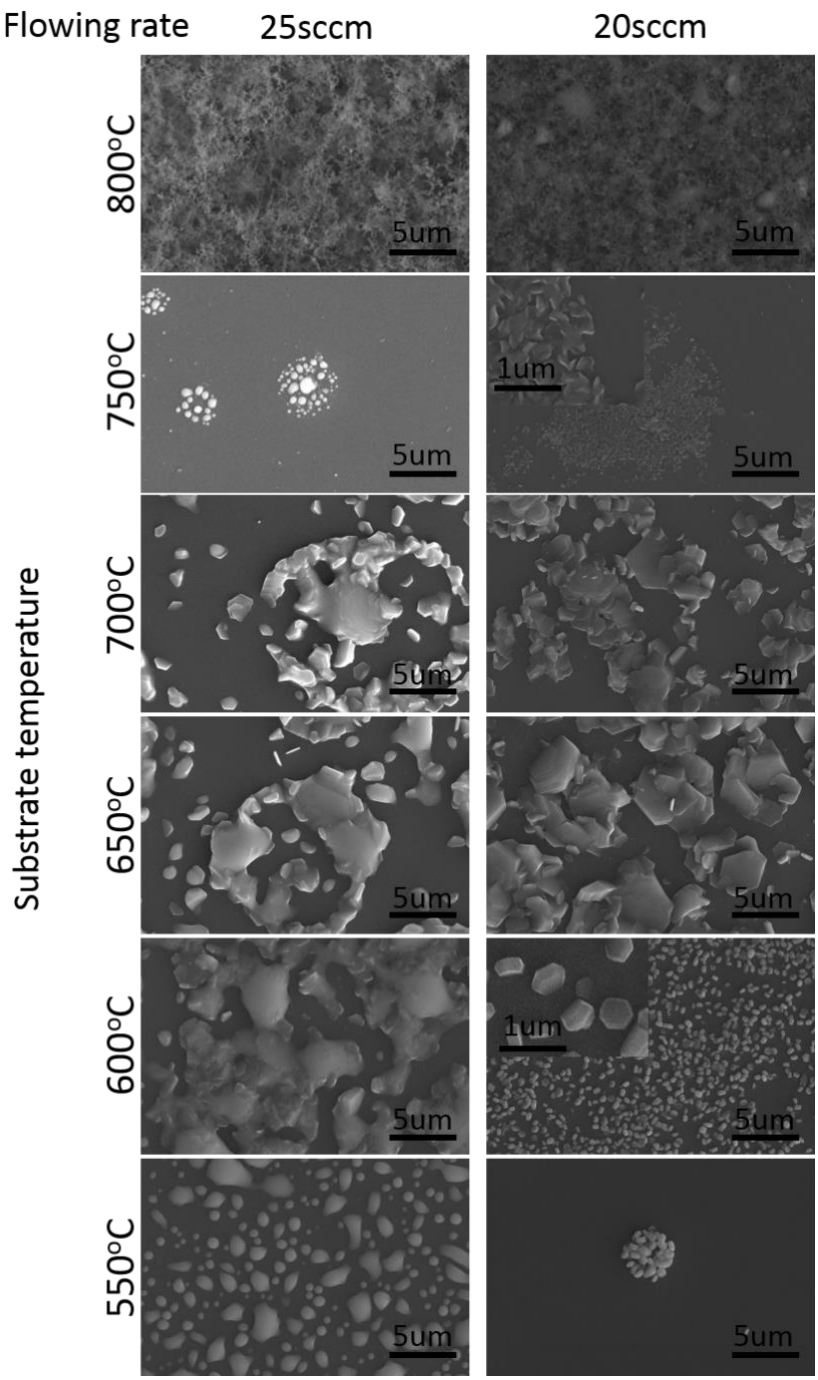

Figure 19: SEM images of NPs synthesized at two different flowing rates and various substrate temperatures. The vertical axis shows the substrate temperatures from 550°C to 800°C at a 50°C increment. The horizontal axis shows the flowing rates at 25 sccm and 20 sccm.

NP morphological control by growth time.

Figure 20 compares SEM images of the NPs which were grown at two different growing times and various substrate temperatures from 550^{o}C to 800^{o}C. The precursor temperature, flowing rate and chamber pressure were set at 850^{o}C, 25 sccm and 5 torr, respectively. It is observed that a growing time of 5 minutes offer better NPs. As it is also shown in Figure 20, the shorter growing time will reduce the reaction time between the silicon powder and tellurium powder. Therefore, less SiTe vapor can be produced during the short growing time which leads to less NPs can be formed through the process. This behavior becomes clearer for substrate temperatures at 600, 700 and 750^{o}C, which show a significant effect for the reduction of the growing time. When the reaction time is longer than 5 minutes the morphology of NPs can have irregular shapes. The reason is due to the fact that a longer growing time will allow more tellurium powder to evaporate and then reacts with the silicon precursor. Through the cooling process, the superfluous tellurium powder will cover on top of NPs and develop irregularly shaped nanostructures.

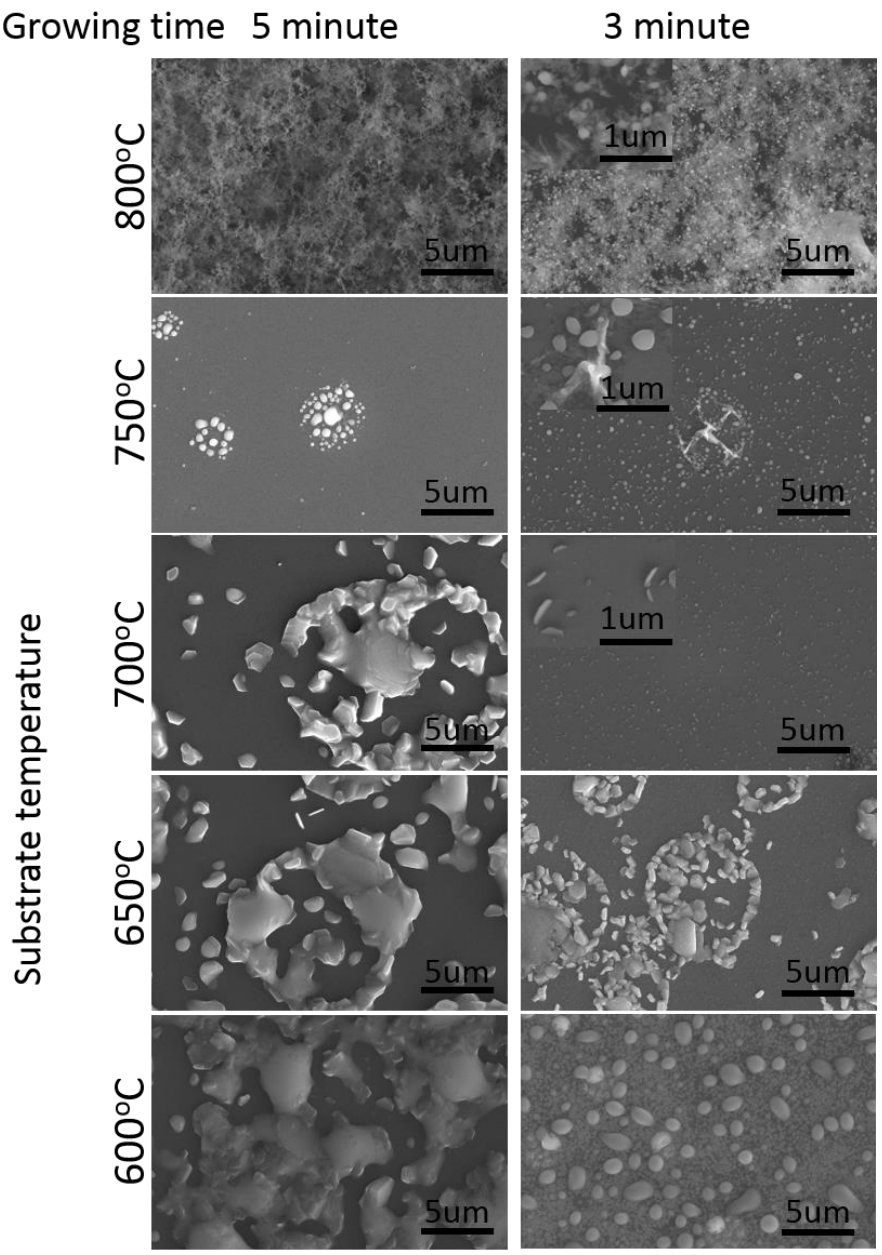

Figure 20: Growth time and substrate temperature dependences: SEM images of NPs synthesized at two different growing times and various substrate temperatures. Vertical direction indicates substrate temperatures (600°C to 800°C at a 50°C increment) while horizontal direction indicates growing times.

NP morphological control by chamber pressure.

Figure 21 shows SEM images of NPs which were grown at two different chamber pressures and several substrate temperatures. Figure 21 (a) and (b) show the samples synthesized at chamber pressure at 5 torr and substrate temperatures at 650°C and 600°C,

respectively. The NPs morphologies for these two different substrate temperatures look very similar. The NP's diameter is around 1 μm, and the thickness of the nanoplates is less than 50 nm. Figure 21 (c) and (d) show the samples that were synthesized at a higher chamber pressure of 200 torr and substrate temperatures at 650°C and 600°C, respectively. Compared with the 5 torr pressure case, the NPs synthesized at a 650°C/200 torr are around 10 μm diameter and a thickness of less than 5 nm. The phenomenon is related to the higher pressure influence of the precursor evaporation and seed process. A high pressure will affect the melting and evaporation points of the precursors. Hence, the quantity of evaporated precursors is different from that of the lower pressure case. Also, the SiTe seed reaction speed is not much influenced by the pressure. Therefore, a higher pressure will produce larger NPs. Furthermore, at a high chamber pressure and a low substrate temperature it is more favorable for Te precursor to adhere to the substrate to form Si_2Te_3 NPs. This is seen by the fact that at 200 torr and 600°C substrates temperature the resulted Si_2Te_3 NPs exhibit a 10 μm diameter and a few hundred nanometers thick.

In conclusion, a low pressure is suitable for the synthesis of small NPs while a high pressure is suitable for the synthesize of large NPs.

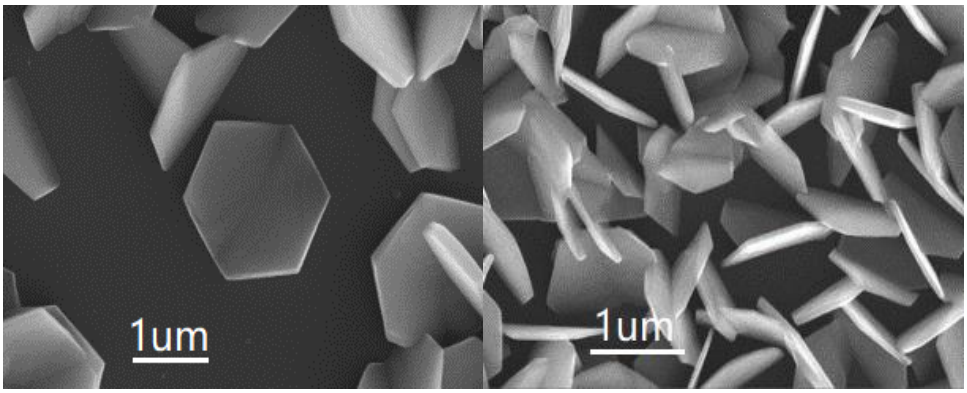

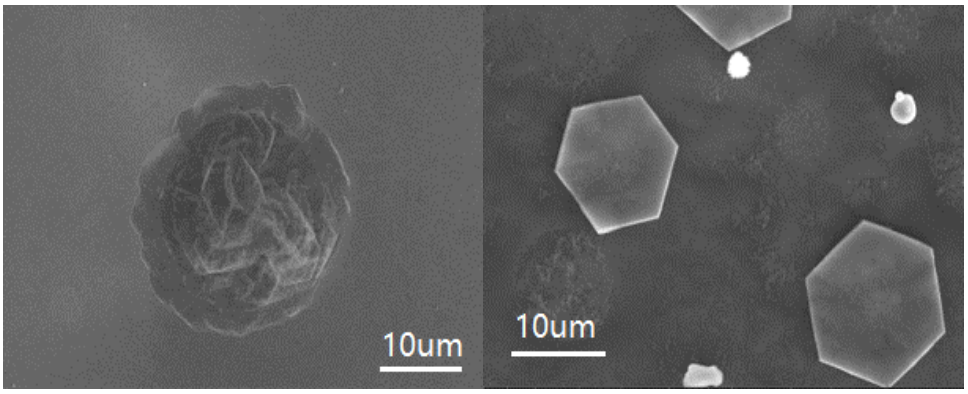

Figure 21: SEM images of NPs synthesized at different chamber pressures and substrate temperatures (a) 650ºC substrate temperature and 5 torr chamber pressure, (b) 600ºC substrate temperature and 5 torr chamber pressure, (c) 650ºC substrate temperature and 200 torr chamber pressure, (d) 650ºC substrate temperature and 200 torr chamber pressure.

Morphological control of Si_2Te_3 NWs by different growth parameters

Compared with the synthesis process of Si_2Te_3 NPs, the synthesis of Si_2Te_3 NWs is more sensitive to a substrate's temperature and flowing rate. The wire-like nanostructures are grown at specific flowing rates and substrate temperatures and the growth mechanism is more complicated than the synthesis of Si_2Te_3 NPs. In the sections below, a detailed description of the synthesis of Si_2Te_3 NWs is presented.

Catalysis selection for Si_2Te_3 NW synthesis

Recent studies have demonstrated the synthesis of the atomic layers TDMCs and their vertical, lateral heterostructures [131][132][133] where metal catalysts can act as an important role for various synthesis mechanisms. Zeng et al. have reported the fundamentals of various catalysts that influenced the growth mechanism of the 2-D material overlayers on both experimentally and theoretically [134].

The growing mechanism of the catalysts assisted layered nanostructures synthesis can be concluded in four elementary steps. First, the vaporized precursor is adsorbed on the surface of the melted metal catalysts. Second, the adsorbed precursor is dissolved into the bulk of the metal catalyst. Third, the dissolved precursor will be nucleated as the seed

molecules, then segregated from bulk toward the surface with the enriched precursor vapor. Final, the precursor vapor nucleates and grows on the surface of the metal catalysts. The adjustment of the growing parameters, such as the carrier gas flowing rate, pressure, precursor temperature and the substrates temperature will control the morphologies of the layered nanostructures or their heterostructures.

In our studies, two different important catalytic processes affect the morphology of the NWs. First, at substrate temperature lower than 600°C, a self-catalyzed process from Te powder will produce small size NWs with a few micrometers in length and hundreds of nanometers in diameter. Second, at a substrate's temperature higher than 600°C, Au catalysts form a liquid alloy phase which can rapidly adsorb vapors to get to a supersaturation level. Subsequently, crystal growth can occur from nucleated seeds at the liquid-solid interface and produce the layered structure through 2-D NPs in the vertical direction.

Source and substrate temperature dependent NW morphology

Besides the catalyst, precursor heating and substrate temperatures are the two main parameters among other synthesis parameters. As we already mentioned before, the precursor temperature should match two primary requirements such that it supports the silicon precursor to react with the tellurium precursor and to evaporate enrich tellurium powder to form a vapor phase. Therefore, for the NW growth the precursor and substrate temperatures are chosen to be the same for the NPs synthesis. For the synthesis of Si_2Te_3 NWs, we first spin coated 10 nm Au catalyst nanoparticles on the surface of a substrate with a 4000 rpm (round per minute) rotational speed. Following steps and growth parameters are identical to the synthesis of the Si_2Te_3 NPs. Figure 22 shows SEM images of the wire-like nanostructures which were synthesized at various precursor and substrate temperatures. When the precursor heating

temperature is set at 800°C and the substrate temperature is varied from 600°C to 800°C, only irregular shaped tellurium structures are deposited. This is similar to the synthesis of the Si_2Te_3 NPs that when the substrate temperature is kept at 800°C, only the tellurium powder is deposited on the substrate. When the substrate temperature is lowered to 700°C, Si_2Te_3 NWs could be observed on the substrate. These NWs are a couple of hundred nanometers in diameter and few micrometers in length. Furthermore, the catalyst Au nanoparticles can be seen on one end of the NWs. The NW growth mechanism can be explained as follow: the melted Au catalysts adsorb the SiTe vapor then dissolve it into the bulk of the metal catalyst. The dissolved SiTe atoms are segregated from bulk to the bottom surface of the Au catalyst then nucleates as the seed and react with the enriched tellurium powder to produce the Si_2Te_3 wire-like nanostructures. The Au catalyst nanoparticles are then pushed upward as NWs grow. If we decrease the substrate temperature further to 600°C, the amount of tellurium powder is not enough to react with the SiTe seed to develop the NWs. Because of this, the amorphous structures with uneven surface are observed for substrate temperature at 600°C. Similarly, spherical structures with the uneven surface are observed at 550°C.

A higher precursor heating temperature will produce more tellurium and SiTe vapors. As shown in second column in Figure 22 for the precursor temperature at 825°C, long Si_2Te_3 NWs with a rough surface are observed. The rough surface is caused by the rich tellurium vapor deposition on the NW side wall during the cooling process. When the substrate temperature decreases to 750°C, the lateral and vertical layered nanostructures are formed. It appears that the hat-like Au nanospheres appear on one end of the layered nanostructures, and the layered nanostructures are built up by many hexagonal Si_2Te_3 NPs. For substrate temperatures at 700°C and 650°C, more NPs stack to form tower-like layered nanostructures.

When the substrate temperature decreases further to below 600°C, the result is same as for the precursor heating temperature at 800°C (Figure 22, first column).

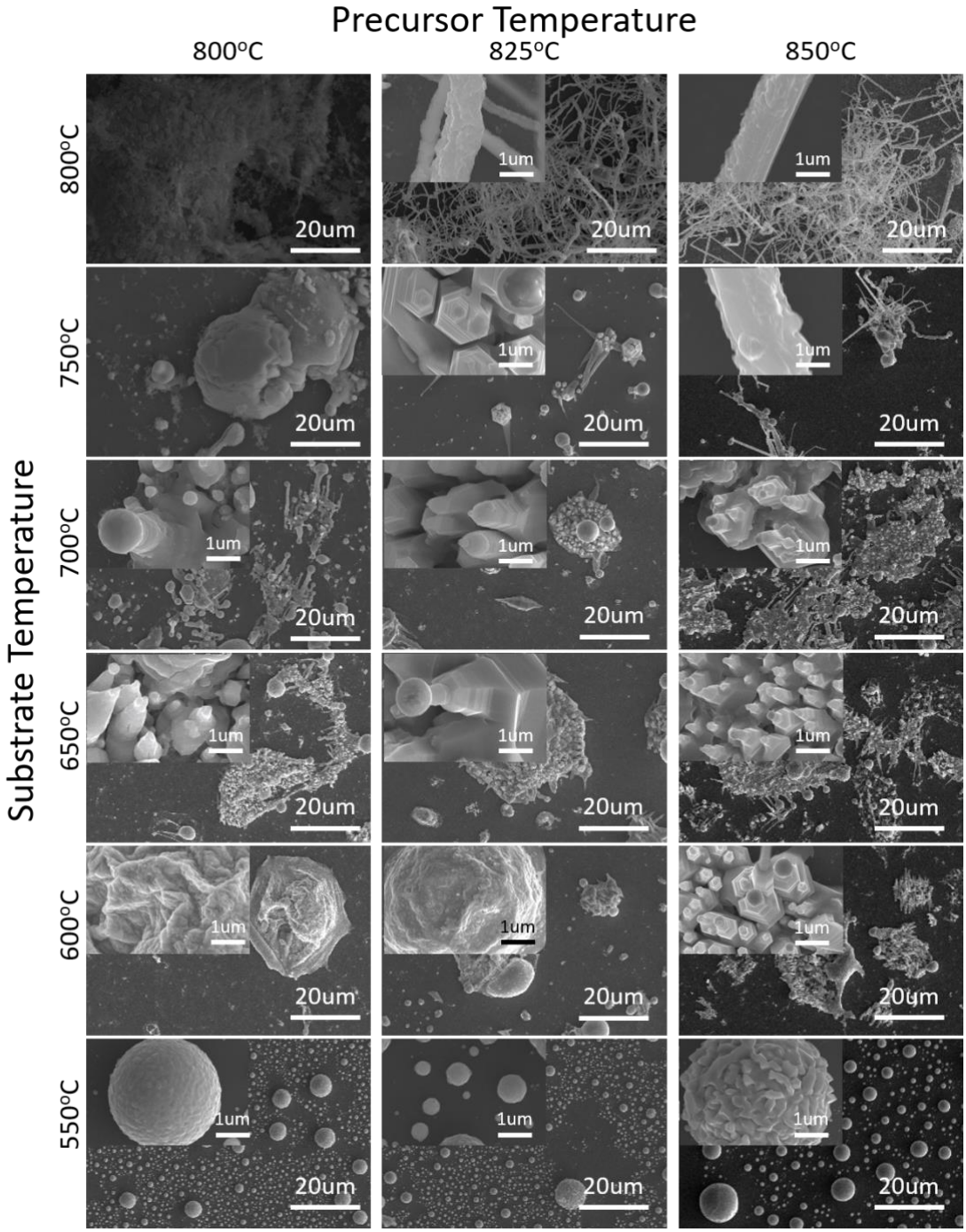

Figure 22: SEM images of Si_2Te_3 NWs synthesized at three different precursor heating and substrate temperatures. The vertical direction shows the substrate temperatures from 550°C to 800°C at a 50°C increment. The horizontal direction indicates the precursor heating temperatures at 800°C, 825°C, and 850°C.

Finally, when the precursor temperature is increased to 850^{o}C the morphologies of tower-like layered nanostructures are almost the same as for 825^{o}C case for the substrate temperature that is higher than 650^{o}C. However, the higher precursor heating temperature will evaporate higher amounts of the source materials. As a result, the layered 2-D tower-like nanostructures could still be observed for the substrate temperature at 600^{o}C. For substrate temperature at 550^{o}C spherical structures look less smooth when compare with previous cases, i.e. precursor temperatures at 800^{o}C and 825^{o}C. This indicates again that more precursor materials are adsorbed by the melted Au catalyst but could not produce Si_2Te_3 NWs due to the low substrate temperature.

Carrier gas flowing rate dependent NW morphology.

Figure 23 shows morphological changes of Si_2Te_3 NWs which were controlled by various nitrogen carrier gas flowing rates. Similar to the synthesis of Si_2Te_3 NPs, the carrier gas flowing rate is fixed at 15 sccm, 20 sccm and 25 sccm. In this current experiment, all samples were synthesized at a precursor temperature of 850^{o}C and 5 minutes growing time. An overview of various carrier gas flowing rates at different substrate temperatures shows that a change of the flowing rate will produce a gradient of precursor vapor density and its moving speed. Therefore, the morphologies of these nanostructures show a large divergence even at a same substrate temperature. A regularity of morphology controlled by the flowing rate is therefore hard to obtain. One of the main reasons is the nitrogen gas which is at room temperature when being pumped into the vacuum chamber. As a result, this nitrogen carrier gas will alter the temperature of the precursor gradient inside the chamber and this process is very hard to monitor and control.

As shown in the first column of Figure 23, at 15 sccm flowing rate and 700^{o}C substrate temperature, uniform Si_2Te_3 microwires are formed from layered (see inset). The diameter of these wires varies from 1 to 2 micrometers, and the length of the wires could extend to tens of micrometers. Also, the Au catalysts appear on the end of the wires as expected. When the substrate temperature decreases to 650^{o}C, the layered NPs form zig-zag structure and the tapped direction is same as when the substrate temperature at 700^{o}C. When the substrate temperature decreases to 600^{o}C, tower-like structures start to appear. These lateral tower-like structures are crowed by the Si_2Te_3 NPs. The mechanism of the formation of these tower-like structures is significantly different from the formation of Au catalyst assisted wire-like structures. The inset (Figure 23, 15 sccm/600^{o}C) indicates that the Au catalyst spherical structure does not present at the end of these structures. This means that the tower-like layered structures are produced by a self-catalyzed process from tellurium powder during the cooling process. Si_2Te_3 NPs are synthesized during the transportation of the nitrogen carrier gas, and the slow growing rate of these NPs is related to the low flowing rate. As the furnace lid is opened to quickly cool down the substrate for the cooling process, the liquid phase Au catalyst can quickly return to a solid phase and interrupted the catalysis process. It is following that, from carrier gas, Si_2Te_3 NPs continue to self-assemble as the tower-like structures and directly deposit on the substrate.

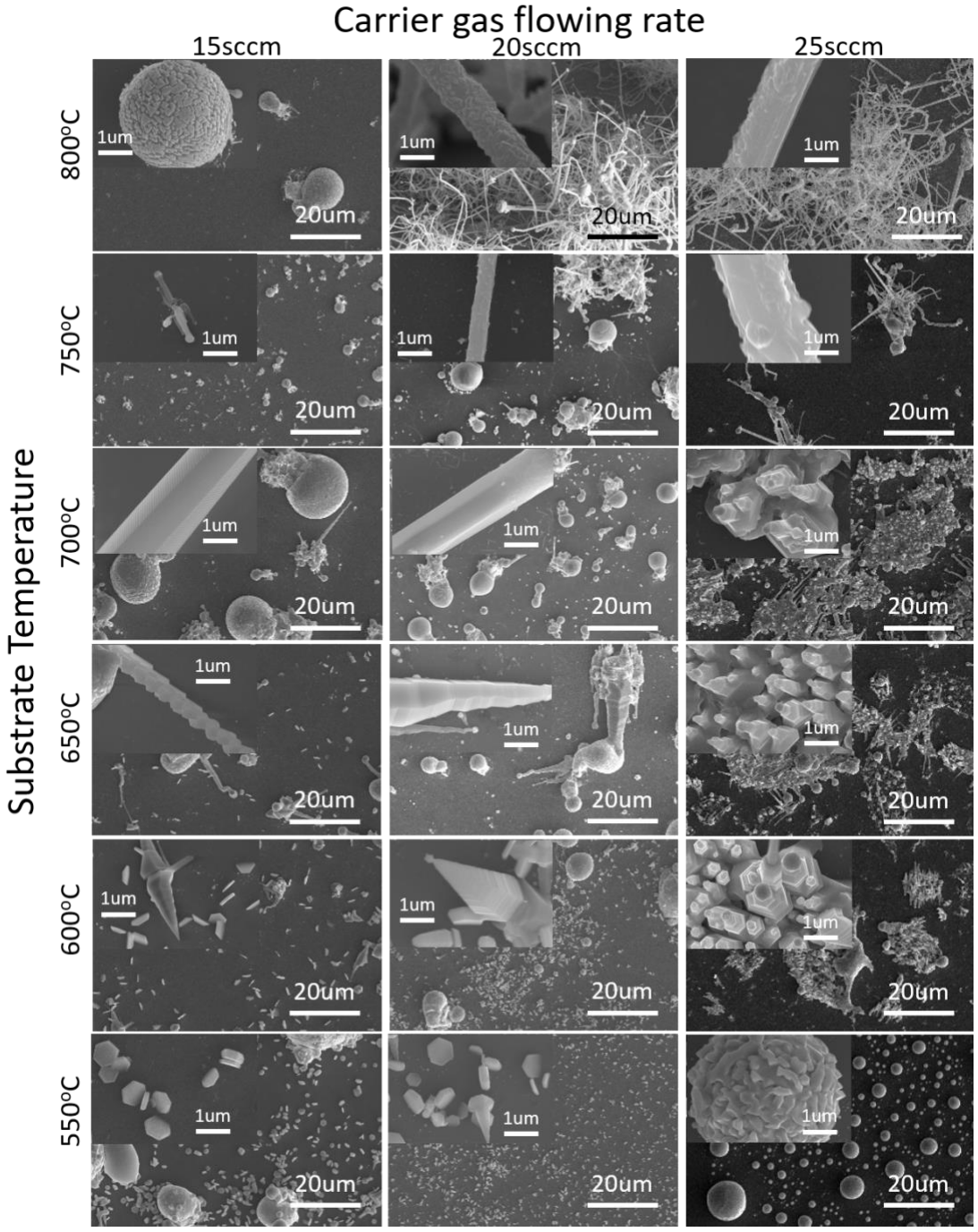

Figure 23: SEM studies of Si_2Te_3 NWs synthesized at three different flowing rates and various substrate temperatures. The vertical direction indicates the substrate temperatures from 600°C to 800°C with a 50°C increment; The horizontal direction shows the carrier flowing rates at 25 sccm, 20 sccm, and 15 sccm.

When the flowing rate is increased to 20 sccm and 25 sccm, the morphologies of Si_2Te_3 NWs for different substrate temperatures are the same. The large micro-sized Si_2Te_3

rods with the smooth surface are formed at 700^{o}C substrate temperature. Once the substrate temperature decreases to 600^{o}C, both the Au catalyst-assisted and the tellurium self-catalyzed tower-like structures are observed.

Si_2Te_3 NW morphological control by growth time.

The growing time also plays an important role on the morphological control of Si_2Te_3 NWs. The growing time of a Si_2Te_3 NW synthesis process is typically reflected from the heating time of the precursor. Typically, the growing time is varied from 1 minute to 10 minutes. A short heating time is hard to promote the silicon powder to react with the tellurium powder to produce the SiTe molecules. A long heating time would evaporate too much tellurium powder in the vapor phase, and during the cooling process the tellurium vapor will deposit onto the substrate and cover every structure on the surface with a tellurium layer. Therefore, the best growing time is limited to the range 3 to 5 minutes.

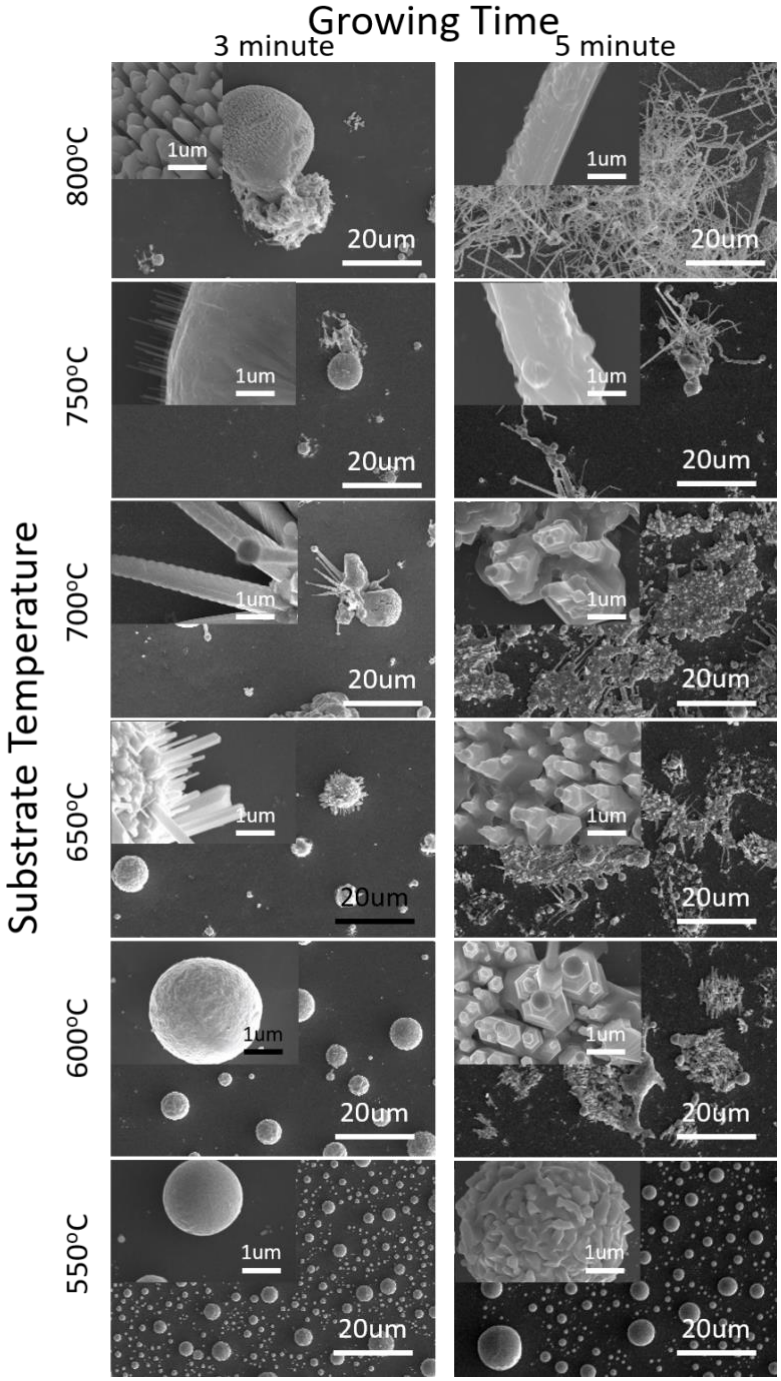

Figure 24: SEM study of samples which are synthesized at two different growing times and various substrate temperatures. The vertical direction shows the substrate temperatures from 600°C to 800°C at a 50°C increment while the horizontal direction shows the growing time at 3 and 5 minutes.

Figure 24 shows various morphologies of Si_2Te_3 NWs which were grown with two different growing times and different substrate temperatures. It appears that the NW

morphologies for 3 minutes growing time show significant differences from that of NWs grown in 5 minutes. For the substrate temperature at 800^{o}C and 3 minutes growing time, large spherical-head structures at tens of micrometer diameters are observed. The hexagonal nanorods are uniformly grown on the surface of these sphere structures. For the 5 minutes growing time we observed long Si_2Te_3 NWs grown in all directions. The NWs appear to have diameter around 1 micrometer and length of several tens of micrometers. For the substrate temperatures from 550^{o}C to 750^{o}C similar results are observed.

Chapter 4. Electrical measurements and resistive switching in Si_2Te_3 nanowires

In this chapter, we investigate the structural and electrical properties of Si_2Te_3 nanowires. It was found that the nanowires grow along the c-axis, (along the [0001] direction) with a stacking of layered nanosheets via the van der Waals force forming 1-D single crystalline structures. These 1-D NWs, which are composed of 2-D Si_2Te_3 layers, exhibit a unique resistance switching behavior under an applied electrical potential. A stable low-resistance state (LRS) is defined by an initial voltage applied to a freshly prepared NW. One can switch the LRS to the high-resistance state (HRS) by changing the polarity of the applied electrical potential. Our study indicates that the resistance switching behavior of the unique silicon-based Si_2Te_3 NWs is of great interest for both fundamental understanding and practical applications in memory devices.

SEM and TEM characterizations of the resistant switching Si_2Te_3 NWs

Si_2Te_3 NWs were synthesized by using CVD method as described in chapter 3. In brief, the NWs were grown on Au-coated fluorine-doped tin oxide (FTO) substrates in a quartz tube at 650^{o}C by using silicon and tellurium as sources materials. The Si_2Te_3 NWs grown on the edge of the FTO glass were used for electrical study by contacting the NWs with a liquid gallium (Ga) electrode, while the conducting FTO on which the NWs grow was used as another electrode. A micromanipulator is used to move the Ga electrode and approach the NWs to make electrical contact while the electrical current is monitored. Note that the liquid gallium is used as an electrode to avoid mechanical damage to the NWs once physical contact is established.

The morphology and crystal structure of the Si_2Te_3 NWs were studied by SEM and TEM, as shown in Figure 25 (a) and (b). One can see that the NWs show diameters ranging

from tens to hundreds of nanometers and lengths of up to 60 µm. Each NW has a very uniform diameter over the whole length scale and is mostly straight with Au catalyst nanoparticles at the tip of the NWs.

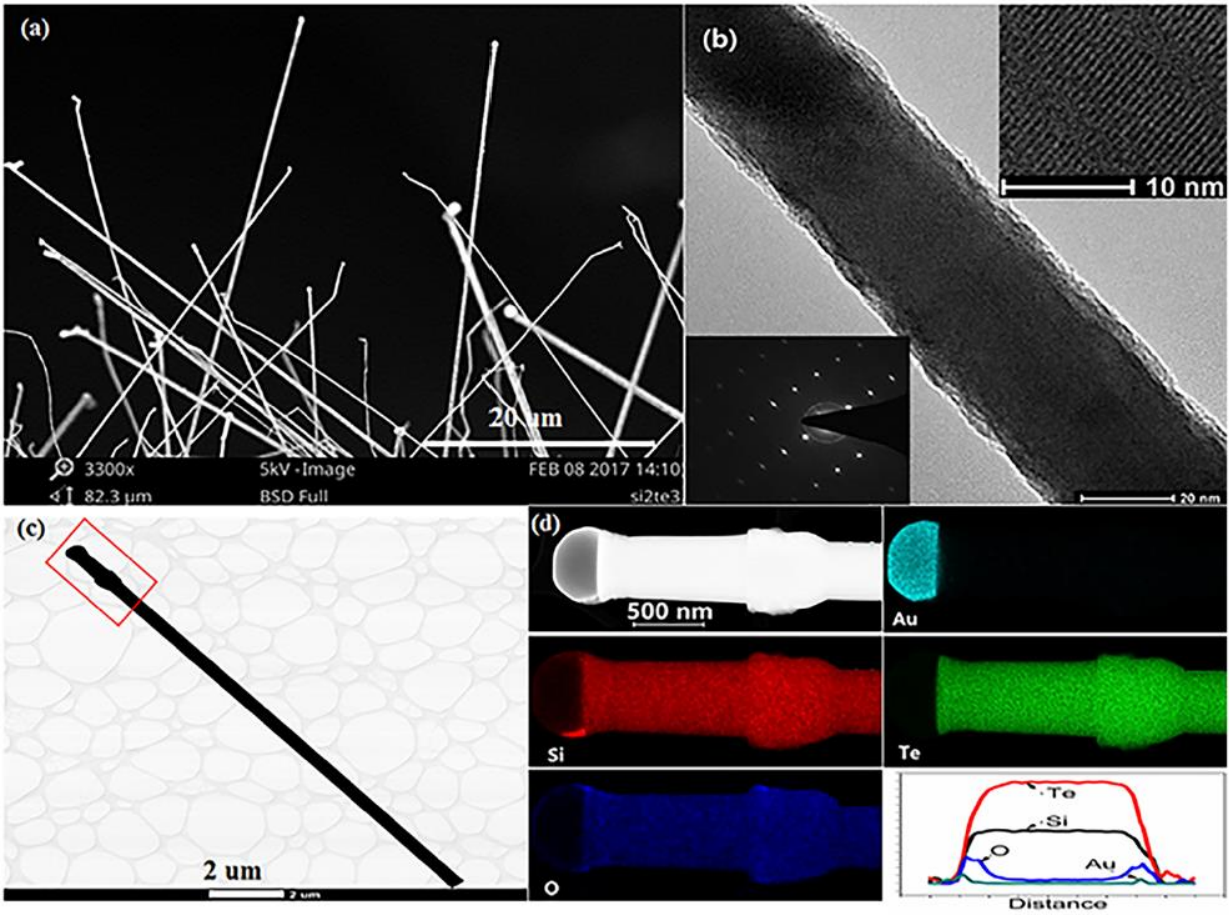

Figure 25: SEM and TEM images of Si_2Te_3 NWs for electrical measurements (a) SEM image for Si_2Te_3 NW sample used for electrical measurements. (b)TEM image for a single Si_2Te_3 NW, the insets show high-resolution TEM and SAED images of the NW. (c) Bright-field TEM image of an individual NW, and (d) EDX elemental mapping for Au, Si, Te, O, and the cross-sectional line scan for each element.

Figures 25 (b) and (c) show a typical TEM image obtained for a thin NW with a diameter of 40 nm. The high resolution TEM (HRTEM) image in the inset clearly shows the fringes of the Si_2Te_3 NW, which indicates that the NW is composed of stacked layers along the [0001] direction via a weak van der Waals interaction. The periodicity for the alternating fringes along the NW growth direction is 0.65 nm, corresponding to the distance between the

(0002) planes for hexagonal Si_2Te_3. The selected area electron diffraction (SAED) pattern shown in the inset of Figure 25 (b) also confirms that the growth direction of the NWs is along [0001]. EDX spectroscopy was used to determine the NW's composition, which shows an elemental ratio of 2:3 for Si and Te in the NWs. The elemental compositions were also confirmed by the X-ray photoemission spectroscopy. Figure 25 (d) shows a TEM image, bright field scanning transmission electron microscopy (STEM) image, and spatial distribution for the Si, Te, O and Au elements of a Si_2Te_3 NW. Gold atoms were found only at the tip of the nanowire. Both Si and Te atoms are uniformly distributed across the NW. The EDX elemental line scans across the NW do not reveal a variation for the Si and Te elemental distributions within the NW. It is also noted that the O element exists on the surface of the nanowire. This is because the Si_2Te_3 has pronounced hygroscopic properties and its surface can easily react with water vapor when exposed to air.

Electrode approach to single NWs

The setup for electrical contacts is illustrated in the Figure 15 in Chapter 2. An experimental procedure is shown Figure 26. The electrical current as a function of time is recorded under a constant voltage of 0.1 V for a NW moving towards the Ga electrode. In Figure 26 (a), the initial current is zero because there is no contact between the NW and Ga electrode. As the Ga electrode approaches the Si_2Te_3 NW, the current jumps from 0 to approximately 0.9 nA at time t = 103 seconds, indicating that a nanowire is in contact with the Ga electrode. If one continues to move the Ga electrode toward the NW sample, the current stays unchanged until it jumps from 0.9 to 1.8 nA is observed at approximately 107 seconds due to an additional NW making contact with the Ga electrode. Further moving of the Ga electrode closer to the NW sample leads to the observation of a large jump in the current of up

to 7 nA, which may be caused by a large NW or a group of NWs contacting with the Ga electrode. As the translational stage with the Ga electrode moves away from the NWs, the current suddenly drops to 0.9 nA and further to zero. This experimental approach confirms that it is possible to make electrical contact with the fragile NWs using a liquid electrode and measure the current-voltage (I-V) curve for a single Si_2Te_3 NW. Once contact with the NWs by the Ga electrode is established, an I-V curve can be measured, as shown in Figure 26 (b). A nonlinear characteristic I-V curve is observed, which shows that the as-prepared Si_2Te_3 NW is a semiconductor. In the low voltage range between -1 and 1 V, the I-V curve is repeatable when sweeping the voltage back and forth. Note that the current for the individual NWs may vary due to their different diameters.

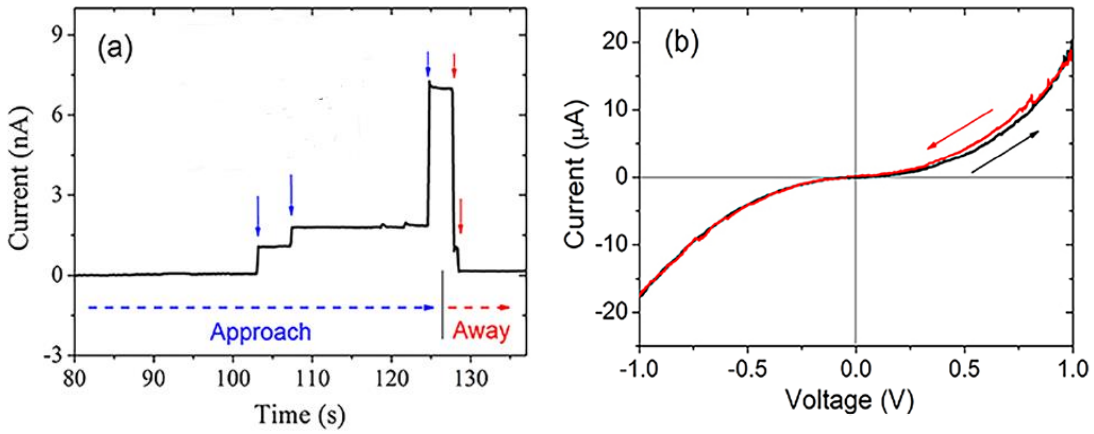

Figure 26: Electrode approaching to a Si_2Te_3 NW. (a) Variation in time of the current through Si_2Te_3 NWs under an applied voltage of 0.1 V as a gallium electrode is moved toward and away from the NW(s). (b) I-V curve measured between -1 and +1 V.

Resistant switching behavior of single Si_2Te_3 NWs

The resistance switching behavior is observed for a Si_2Te_3 NW when the applied voltage is increased. The current jumps from low to high corresponding to a sudden drop in resistance at the applied voltage. This process is referred as a SET process for switching from high resistant state (HRS) to low resistant state (LRS). If one continues to increase the voltage, a few current jumps occur at different voltages. When the voltage sweeps back from

+3.0 to -3.0 V, the LRS is initially preserved until a negative voltage of -1.1 V is applied. The resistance switching from LRS to HRS is referred to as a RESET process. When the voltage is scanned from -3.0 to 0 V, the resistance of the NW does not change.

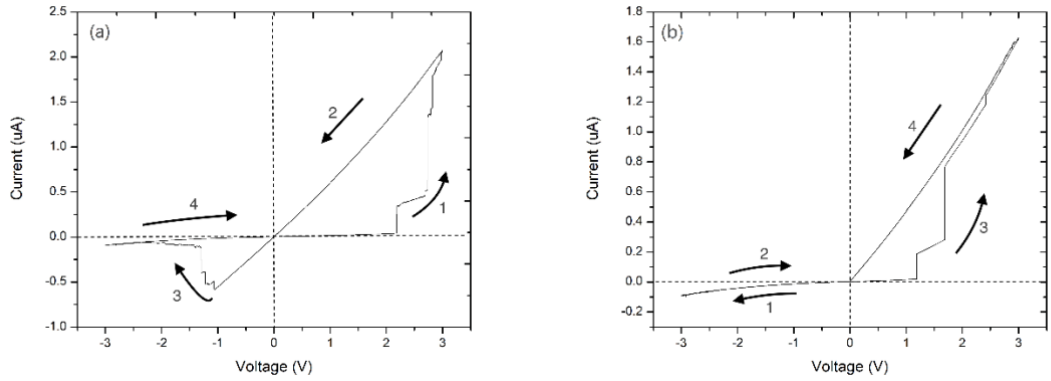

Figure 27: Electrical switching behavior of single Si_2Te_3 NWs (a) Resistance switching behavior of a SET process from HRS to LRS with an initial polarization of a positive voltage. A RESET process occurs when the voltage sweeps back from +3.0 to -3.0 V. (b) The NW remains in the HRS when a negative voltage is applied initially as an opposite voltage scan sequence. A SET process for switching when the voltage sweeps from -3.0 to +3.0 V. For both (a) and (b) the voltage sweep sequences are indicated by arrows labeled 1, 2, 3, and 4.

An opposite voltage scan sequence is used to test if the switching behavior shows an asymmetric change. As shown in Figure 27 (b), the NW remains in the HRS when a negative voltage is applied. The switching behavior only occurs once a positive voltage is first applied. Therefore, the switching process as SET occurs only with a positive applied voltage, while the RESET process only occurs with a negative applied voltage. In other words, the switching behavior is not symmetric.

To further explore the directional switching behavior another set of experiments were designed to reveal the switching mechanism. Figure 28 (a) shows the I-V curve obtained for another Si_2Te_3 NW, which was measured by applying an initial voltage in the opposite direction compared with the previous measurement. The voltage direction was applied from 0 to a negative value. The first SET process occurs at -0.6 V. Additional current switching

events occurred at larger negative voltages. As the voltage scanned back from -3.0 V to 0 V, the LRS stays unchanged. Furthermore, once a positive voltage was reached, the RESET process occurs at approximately 0.9 V. It took a few steps for the NWs to complete the RESET process and then back to its original resistance. Experiments were also carried out by starting the voltage first scanned from zero to +3.0 V for this sample. Interestingly, no current switching with applied positive voltage was observed but switching did occur for a negative applied voltage, as shown in Figure 28 (b). This observation shows that the SET process from the HRS to LRS occurs only at a negative voltage, while the RESET process occurs only at positive voltage.

The experimental data shown in Figure 27 and Figure 28 clearly indicate that the SET and RESET processes depend on the initial voltage applied. In other words, the SET and RESET processes determined by the first scan direction, a positive or negative voltage. If the first scan starts from 0 to a positive voltage, a SET process from the HRS to LRS is programmed to occur at positive voltage. The NWs permanently inherit the SET at positive voltage and RESET at negative voltage sequence. However, if the initial applied voltage scans from 0 to a negative value for the SET process, then the device shows a SET at negative voltage and a RESET at positive voltage. Therefore, the polarity of the voltage applied to a Si_2Te_3 NW for inducing resistance switching for the first time permanently defines the SET and RESET conditions in the NW. This initial applied voltage for switching is believed to cause a permanent change in the NWs, which is difficult to completely reverse afterwards. The resistance switching behavior is repeatable for individual NWs as well as many NW samples.

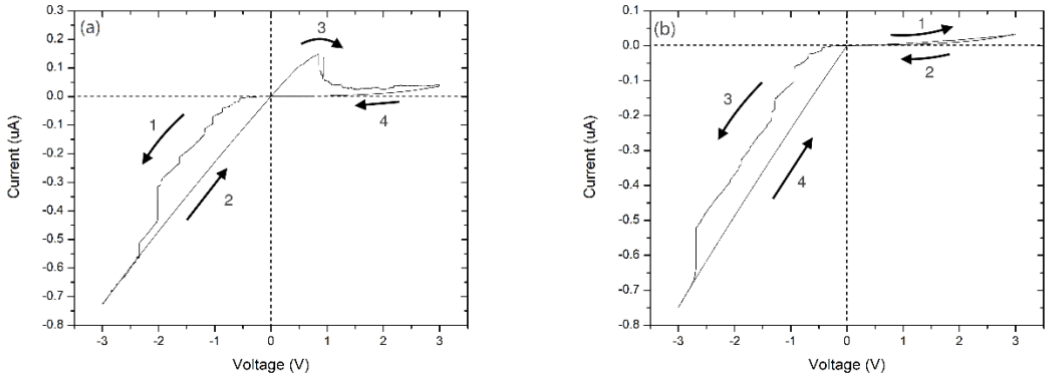

Figure 28: Directional dependent switching behaviors of Si_2Te_3 NWs (a) Resistance switching behavior as a SET process from high resistant state (HRS) to low resistant state (LRS) with an initial polarization using a negative voltage. A RESET process when the voltage sweeps back from -3.0 to +3.0 V. (b) The NW remains in the HRS when a positive voltage is applied initially as an opposite voltage scan sequence. A SET process for switching occurs when the voltage sweeps back from +3.0 to -3.0 V. The voltage sweep sequences are indicated in the figures by arrows labeled 1, 2, 3, and 4.

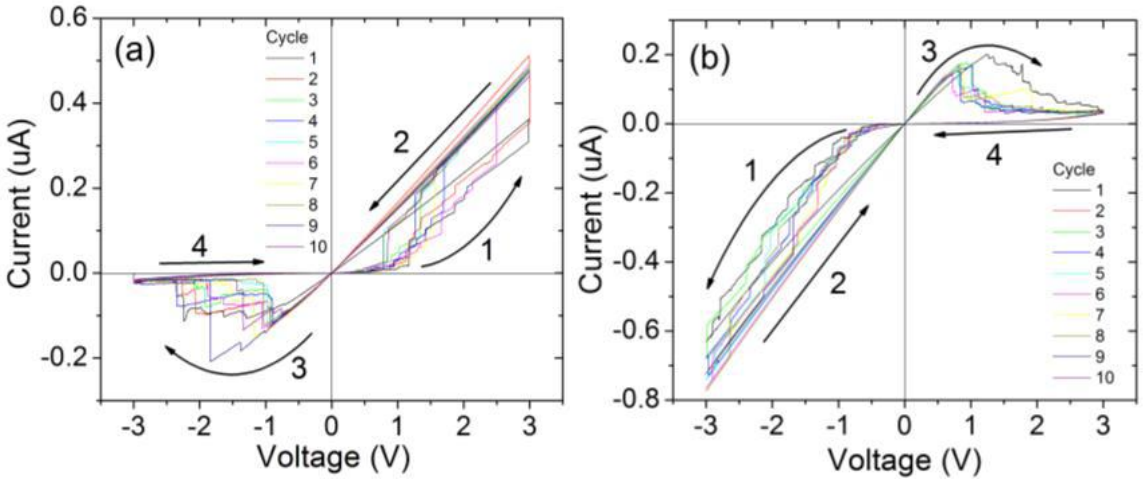

Figure 29: Repeated I-V scanning for a single nanowire through 10 cycles in positive (a) and negative (b) directions. The numbered arrows in (a) and (b) show the voltage scan sequences.

To confirm the switching behavior of Si_2Te_3 NWs is repeatable, repeated SET and RESET for resistance switching for two types of "programmed" NWs using different polarities for the initial voltages were performed. Figure 29 (a) and (b) show the obtained results. Each experiment was carried out by scanning the voltage for 10 cycles. Clearly, the SET and RESET voltages at each cycle are slightly different from each one, however the switching behavior is still well-reproduced each time.

The stability of the NWs in the HRS and LRS states was also studied by monitoring the current under a constant voltage of 0.1 V over time. The currents in both states were extremely stable without a noticeable change observed over 2000 seconds as shown in Figure 30.

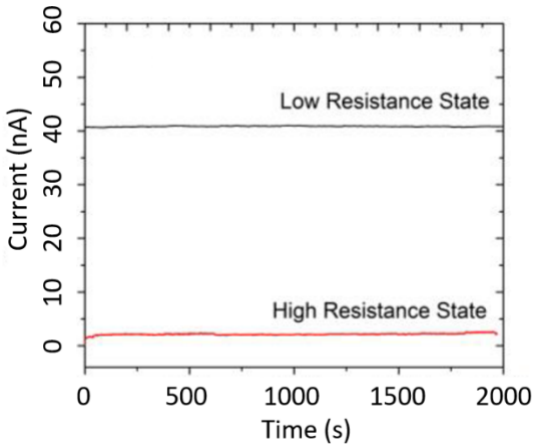

Figure 30: Stability test for devices in the HRS and LRS with an applied constant voltage of 100 mV for 2000 seconds.

Theoretical investigation of the switching behavior in Si_2Te_3 NWs

The resistance switching properties have been studied for other semiconductors. The switching mechanism generally involves formation of metal filaments, phase change from crystalline to amorphous upon application of the voltage, and Schottky barrier and Poole-Frenkal emission. The resistance switching behavior in the Si_2Te_3 NWs cannot be explained by the crystalline to amorphous phase change as such a mechanism is usually unipolar rather than bipolar as observed in in Si_2Te_3. It is also unlikely due to the formation/rupture of nanoscale metal filaments, as no mobile metal ions are present. The contact effect is also excluded because the switching behavior is independent of electrode materials as being used in this study. The role of surface SiO_x if any played in the switching can be also excluded because the field strength along the NW is too low and the current mainly through Si_2Te_3 NW is not high enough to induce filament formation from SiO_x. In addition, the I-V curve

becomes linear after switching to LRS, which suggest metallic phase is achieved. Filament and other current mechanisms cannot explain the metallic conducting in Si_2Te_3 NWs.

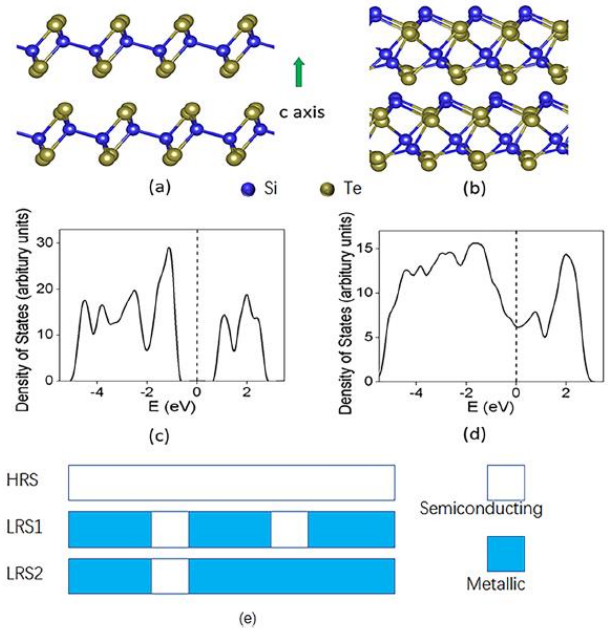

Figure 31: Theoretical prediction of the switching behavior in Si_2Te_3 NWs. (a) Structure of semiconducting Si_2Te_3; (b) structure of metallic Si2Te3 after restructuring; (c) density of states for semiconducting Si_2Te_3; (d) density of states for metallic Si_2Te_3 calculated by density functional theory (DFT); and (e) illustration of switching from the high-resistance state (HRS) to multiple low-resistance states (LRSs).

Based on the results obtained from first-principles calculations, we propose that the resistive switching in Si_2Te_3 NWs originates from a unique phase transition: when an external voltage is applied along the NWs, the Si-Si dimers in Si_2Te_3 dissociate under the effect of Joule heating, with one of the two Si atoms in the dimer migrating across the top of the Te bilayer under the electric field, causing the Si_2Te_3 to restructure into a metastable metallic phase (Figure 31). We have carried out structural optimization of the model for restructured Si_2Te_3 (Figure 31 (b)) using density functional theory and found that this structure is indeed metastable. We also calculated the electronic density of states for the restructured phase, which shows a metallic feature (Figure 31(d)) compared to the original semiconducting Si_2Te_3 phase (Figure 31(c)). Therefore, the restructuring shown in Figure 31 (a) and (b) can explain

the resistive switching in Si_2Te_3 NWs. This switching mechanism explains the bipolar switching behavior because an opposite voltage is required to move the migrated Si atom back to its original position. This mechanism also explains the multiple resistance states observed for the NWs during switching because restructuring can occur in different segments of the NWs instead of the whole NW, as illustrated in Figure 31(e).

This mechanism is also further supported by the experimental data obtained for the number of SET and RESET steps. When only one SET occurs (i.e., one resistance switching), only one recovering step is needed and observed. This corresponds to one segment of nanowires being switched. As the number of SET steps increases, i.e., more segments participate in the transition from semiconducting to metallic, the RESET process also requires more RESET steps of the same number to switch the NWs back to their original state. This observation agrees well with the proposed mechanism that involves switching of the different segments of the NWs, as shown in Figure 31 (e).

It should be noted that the as-fabricated NWs show symmetric switching, as the first SET process can occur under either positive or negative voltages. However, after the first SET, the polarity of the NW is fixed. This phenomenon can be understood by the fact that it is likely that after the first SET and RESET, not all atoms of the restructured metallic Si_2Te_3 are switched back to the original position. The metallic phase of the Si_2Te_3 shows a permanent electrical dipole moment due to the asymmetric distribution of Si and Te along the c-axis (Figure 31 (b)), and the parts of the NW that have not switched back to the semiconducting phase will show an electrical dipole moment in the same direction as the first SET voltage. If one attempted to SET the NWs using the opposite voltage, the remaining electrical dipole moments will cancel the external electric field and prevent the SET process.

Conclusion of the resistive switching of Si_2Te_3 NWs

In conclusion, the resistance of the nanowires can be reversibly switched between high or low resistance states by applying an electric potential, which demonstrates that the Si_2Te_3 nanowires are a promising candidate for resistive memory devices. The polarity of the bipolar switching can be “programmed” by the polarity of the initial voltage applied to a freshly prepared nanowire. The resistance switching behavior is explained by a phase transition between metallic and semiconducting segments along the nanowires, as supported by both experimental data and theoretical calculations.

Chapter 5. Temperature dependent photoluminescence and carrier dynamics of Si_2Te_3 nanowires

In this chapter, we study the dynamics of photoexcited carriers in ensembles of Si_2Te_3 NWs as functions of temperature and excitation power. The Si_2Te_3 NWs were grown directly on silicon substrates, making them possible to integrate with other future optoelectronic devices. We observed that the photoluminescence (PL) intensity and decay time of photoexcited carriers vary significantly under different measurement conditions. Specifically, the emitted photons exhibited a long decay time (>10.0 ns) at low temperatures (<100K) but much shorter (~1.8 ns) at room temperature, which is associated with an abrupt reduction in the intensity. Further, at any given temperature, the decay time reduced as a result of the increasing excitation power. These results indicate a significant non-radiative recombination rate associated with defects/surface states. Increased temperature could also change the crystal structure of the NWs, which led to the modification of the band structure and the carrier dynamics. Our study offers an insight into the decay dynamics of the photoexcited carriers and hints at possible applications of the Si_2Te_3 NWs in optoelectronics.

Optical setup for measurements of Si_2Te_3 NWs

In the experimental procedure, ensembles of Si_2Te_3 NWs were optically excited by an ultrafast laser (Coherent Chameleon Ultra II, 80 MHz, 150 fs). The output (950 nm) of the laser was frequency doubled (to 475 nm) and focused onto the sample, via a 20× objective lens, with an excitation spot size~3 μm. The average laser excitation power was 100 μW (measured before the objective lens); however, for the power dependent experiments, the laser power varied. Si_2Te_3 NW sample was mounted onto the cold finger of a closed-cycle cryostat (Janis model CCS-XG-M/204N). The temperature of the cryostat can be controlled to allow

optical measurements from 9 to 300 K. The PL signal was collected by the same objective lens, analyzed by a spectrometer (Horiba iHR550), and then detected by a CCD (Charged-Coupled Device) camera (Horiba Synapse). For the time-resolved single photon counting measurements, PL signal was filtered by a long pass filter and collected by a fast-timing avalanche photodiode (APD-PDM, Micro Photon Device). A time-correlated single photon counting module (PicoHarp 300), with a time bin of 4 ps, was used to analyze the number of photons as a function of time when they arrived at the photodiode. Final lifetimes were obtained from fits to the data de-convolved with the instrument response function.

Si_2Te_3 NWs were first characterized by the scanning electron microscopic (SEM) method. Figure 32 (a) shows a representative SEM image where as-grown Si_2Te_3 NWs were randomly oriented on a silicon substrate. Individual NWs have diameter and length varying around 300nm and 10μm, respectively. Even though most of NWs were straight and relatively uniform in diameter, it appeared that the NWs exhibited rough surfaces which could eventually affect the optical properties as will be discussed below. Further, due to the random orientation of the NW ensembles in the optical experiments, we have circularly polarized the laser excitation so that several NWs were somewhat equally excited in terms of polarization.

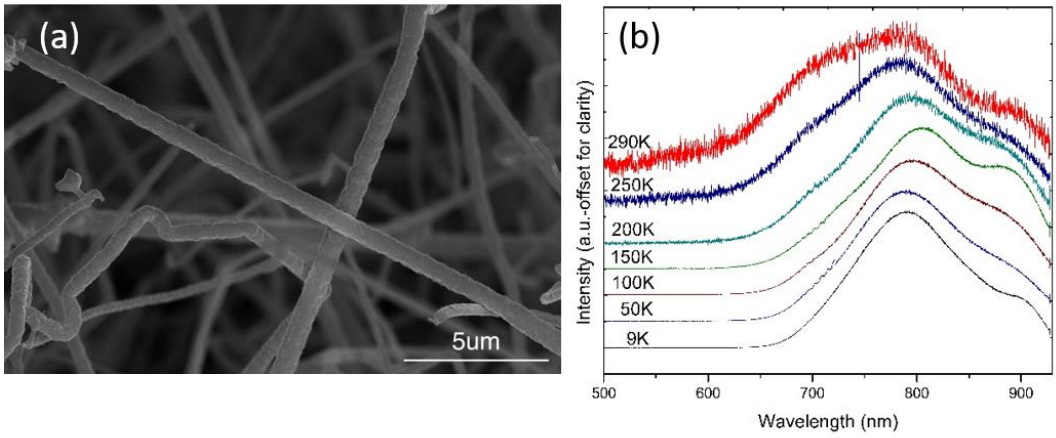

Figure 32: SEM image of the NWs and the PL spectra. (a) SEM image of the NWs used for PL measurement. (b) Temperature dependent PL measured at a fixed laser excitation power P=100μW

Photoluminescence study of Si_2Te_3 NWs

Figure 32 (b) shows the normalized PL emission spectra of a NW ensemble at various temperatures (9–290 K) and at a fixed laser excitation power P=100μW. At low temperatures (<100 K), the PL spectrum featured a broad peak at around 790 nm with a full-width-half-maximum (FWHM)~90 nm and a shoulder at a longer wavelength (~890 nm). Similar results were observed earlier by Wu et al.[109] for Si_2Te_3 nanoplates where these two emission bands were assigned as defect emissions associated with thermal quenching as the temperature increased. However, it is noted that in this work we did not observe the bandgap PL emission near 563 nm (2.2 eV for bulk Si_2Te_3). This could be due to different excitation conditions (pulsed vs continuous laser), crystal quality, or a modification of the band structure in these NWs, which are caused by the reorientation of the Si dimers. Due to the recombination at trap states above the valence band, we can also note that some PL emission bands from bulk Si_2Te_3 were previously observed to exhibit at very low energies (~1.1eV or >1100nm). These emission bands were not detected in our experiment due to a limitation of the silicon CCD and other optics. At higher temperatures, another shoulder appeared at around 700 nm and became more dominant at 290 K. This additional shoulder likely originated from defect centers located at higher energy levels (within the bandgap) and will only be populated at high temperatures or at high excitation powers. The PL emission at various temperatures is further analyzed in Figure 33 (a), which displays the temperature dependence of the integrated PL intensity at temperatures from 9 K to 290 K. At low temperatures (<75 K), the total emitted intensity is high and fairly constant; however, above 75 K, the intensity is abruptly reduced. This is similar to previously observed behavior of Si_2Te_3 nanoplates. The inset in Figure 33

(b) displays the laser excitation power dependence of the total integrated PL intensity at temperature T=9 K. It is clear that below a certain excitation value (<250 μW), the PL intensity increased linearly with the increasing excitation power. Above 250 μW, a saturation behavior occurred which was a result of the reduction in the absorption efficiency. It was also possible that at high excitation powers, the high average number of photoexcited carriers led to the non-radiative recombination with the surface states and resulted in nonlinear relaxation processes (i.e., Auger recombination) which are characterized by a reduction in the photon decay time.

In the previous study by Wu et al. by measuring the PL spectra at different temperatures of Si_2Te_3 nanoplates [115], the authors have extracted very large activation energies, which indicated that several thermal related processes have occurred. Here, we also observed a large activation energy of E=39 meV at temperatures above 75 K. The red lines in Figure 33 (a) were the fits according to $I_0/I - 1 = \exp\left(-\frac{E}{K_B T}\right)$, where I and I_0 are the PL intensities at temperatures T and at 0 K, respectively. This activation energy is even larger than the value of the thermal energy of $K_B T$ at room temperature (~25.7 meV), which suggests that the energy transition of the photoexcited carriers was not purely promoted by the thermal energy but rather a thermal-induced modification of the defect related state energy levels. For instance, defects related to impurities, rough surfaces (Figure 32 (a)), or structural/ chemical modifications could transform to metastable configurations with different energy levels under thermal and optical excitations. A well-known case is the DX center in III-V semiconductors. Such metastable configurations can affect the decay of photoexcited carriers differently, and their populations depend on the temperature and excitation rate. This

hypothesis is further supported by the decay dynamic measurements of the photoexcited carrier as will be presented below.

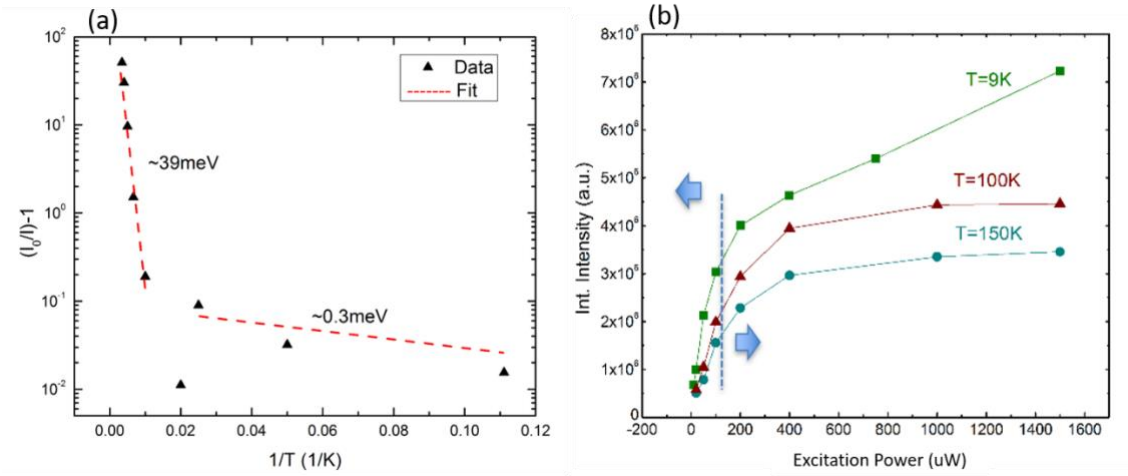

Figure 33: Temperature and excitation power dependent PL emission analysis. (a) Temperature dependent integrated PL intensity at a fixed average excitation power P=100 μW. (b) Excitation power dependent PL emission intensity at temperature T = 9 K, 100 K and 150 K.

Dynamics of photoexcited carriers in Si_2Te_3 NWs

In order to gain further insight into the dynamics of the photoexcited carriers, we performed the temperature dependent time-resolved measurements (Figure 34). At low temperatures (<100 K) and low excitation powers (<100 μW), the decay time of the photoexcited carriers was characterized by a straight line, indicating a long decay time of the excitonic states. Indeed, given 80 MHz of the laser used for this study, we could not perform a fitting procedure to deduct the long decay times for these measurement conditions. This result is consistent with a previous study which concluded a long hole's lifetime in bulk Si_2Te_3. At around 150 K, a decay trace could be observed with a single decay component that has a decay time~10 ns at 100 μW excitation power. At higher temperatures, the decay time became faster and at 290 K, it was determined to be 1.83 ns.

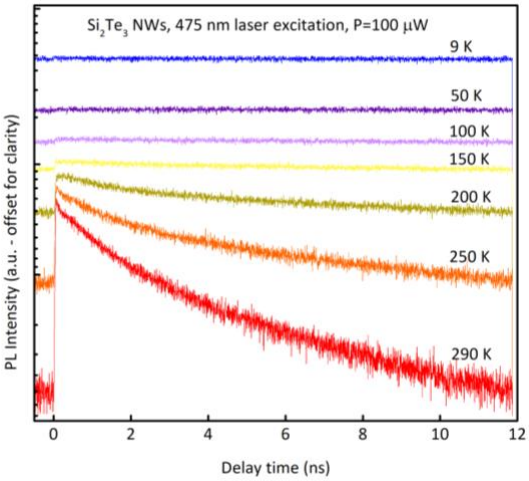

Figure 34: Measured decay curves at different temperatures and at a fixed average excitation power P=100 μW.

A significant reduction of the decay time when the temperature increased indicated several effects. First, there was a thermalization process of neutral donors and thermal quenching of the photoexcited carriers. This is consistent with the observation that there was a significant reduction in the total integrated PL emission intensity (Figure 33 (a)). The thermal processes led to an increase in the nonradiative recombination rate and eventually a reduction in the decay time of the emitted photons. Second, following the work by Shen et al.[106], there could be a re-arrangement in the structural configuration of the Si_2Te_3 lattice at different temperatures, which resulted in a modification in the band structure and carrier dynamics.

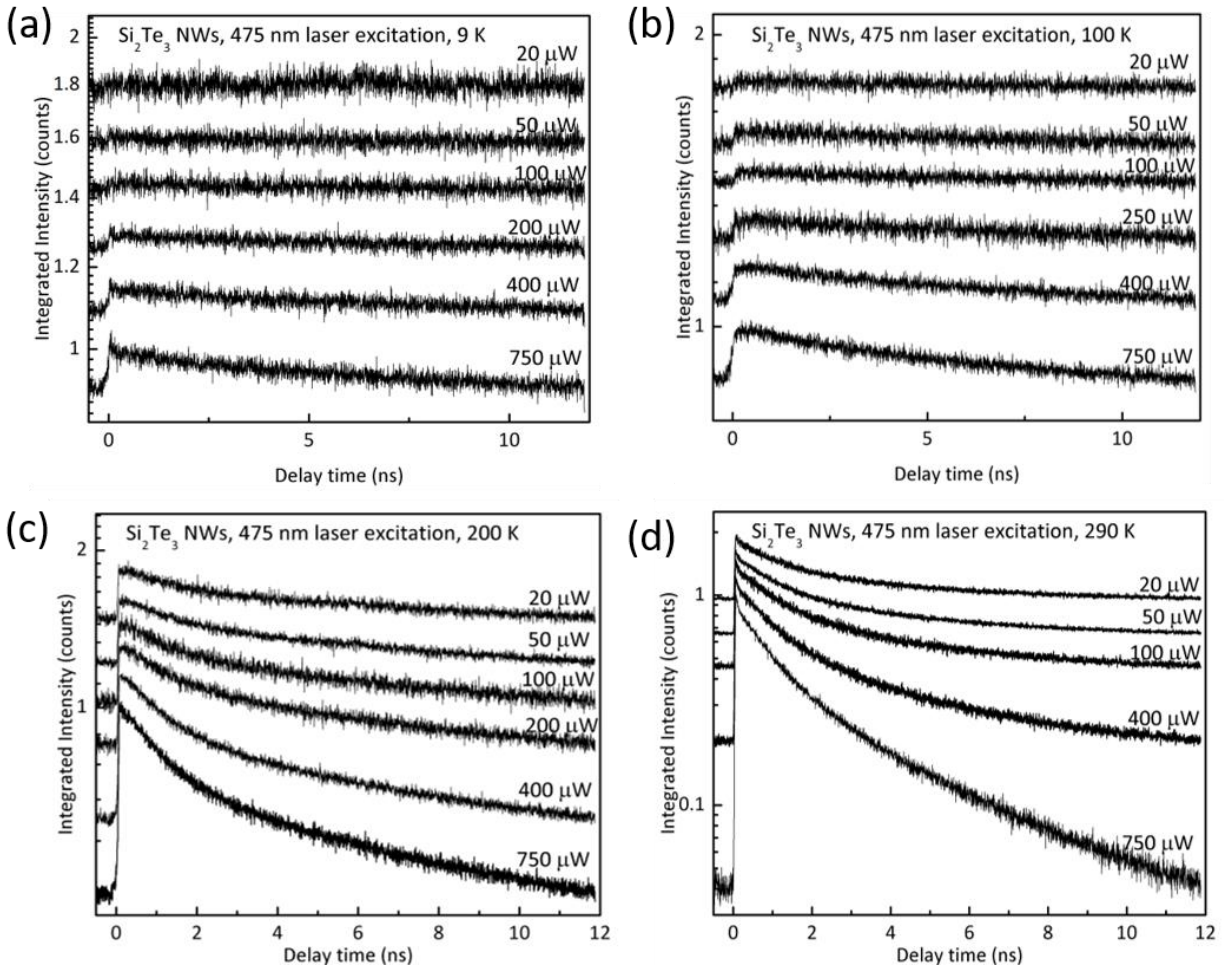

Figure 35: Excitation power dependent decay dynamics at different temperatures (9–290 K) ((a)–(d)). At each temperature, the excitation power was varied from 20 μW to 750 μW.

The decay dynamics of the photoexcited carriers in Si_2Te_3 NWs could also be associated with the carrier generation rate, which is directly related to the incident laser excitation power. Figure 35 shows the decay dynamics of Si_2Te_3 NW ensembles in a matrix of parameters. Specifically, we have measured the decay times of these NWs at various incident laser excitation powers and temperatures. At low excitation powers (<100 μW) and low temperatures (<100 K), the decay curves featured by flat lines from which the decay time could not be determined at least from our current apparatus. Below 100 K, by increasing the excitation power (to above 150 μW), a single exponential decay component could be observed. For instance, at 9 K, the decay time was determined to decrease from 7.25 ns to

6.08ns when the excitation power increased from 200 to 750μW (Figure 35 (a)). Other similar measurements at temperatures 50–290 K are shown in Figures 35 (b) to (d). At room temperature (290 K), the decay time reduced from 1.88 ns to 1.73 ns, as the excitation power increased from 20 to 750 μW. The temperature and power excitation dependences implied that, even at low temperature, the high excitation rate led to a non-radiative recombination of the photoexcited carriers (due to surface states, for instance). At higher temperatures (>150 K), the decay became faster even at low excitation rates, which was the result of thermal effect.

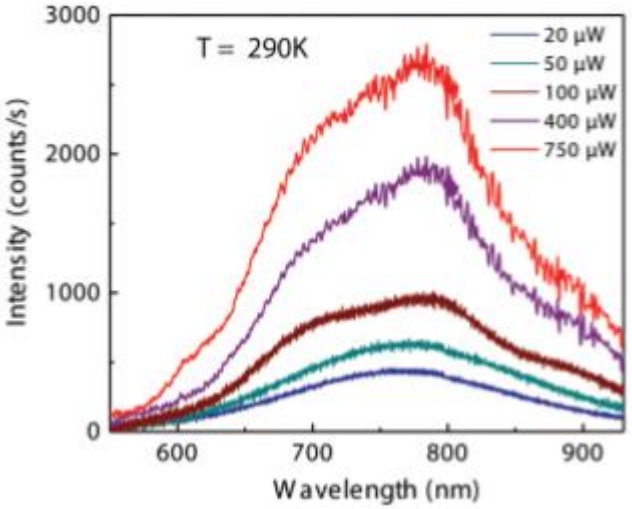

Figure 36: Excitation power dependent PL emission spectra at T=290 K.

At high temperatures (>150 K), the decay times from Si_2Te_3 NWs decreased with increasing excitation power and indeed exhibited bi-exponential decay behavior. Besides the fast decay component [for instance, decay time∼1.73 ns at 750 μW, Figure 35 (e), there was also a slower component which varied from 3.05 to 2.40 ns depending on the excitation power and temperature. The bi-exponential decay behavior of the photoexcited carriers in Si_2Te_3 NWs was associated with a spectral modification under various excitation powers. Figure 36 shows the emission spectra for different excitation powers at T=290 K which clearly indicates

that at high excitation powers, there was an additional shoulder peak at around 680nm. It is likely that this additional energy transition peak, which associated with defect centers, surface states, or band structure modification, has contributed to the bi-exponential decay components of the decay curves shown in Figure 35 (c) and (d). A spectrally resolved decay time measurement in the future could potentially help to relate the emission energies with the fast and slow decay components.

Another possible mechanism which could lead to the shorter decay time at higher temperature and excitation rate is due to the modification of the band structure as the result of changes in the orientation of the Si dimers with respect to the Te atoms. This could be further complicated by the fact that there were boundaries between different crystal domains, which may have different orientations of the dimers. The energy offsets between domains, depending on the temperature, could result in an indirect transition and therefore a different decay time. The current available data achieved in this study did not allow us to draw a direct conclusion regarding a specific band alignment but rather hinted several mechanisms for the decay dynamics of the photoexcited carriers. Nevertheless, we would like to point out that several previous experimental studies on bulk Si_2Te_3 have indicated that different domains of the Si dimers' orientation do exist. Density functional theory calculation has also suggested that different domains exist with different orientations of the Si dimers. Future measurements such as polarized decay dynamics from single Si_2Te_3 NWs in different excitation conditions and in combination with structural characterizations (SEM or TEM) to correlate structural characteristics with optical properties of the same single NWs could potentially provide further information. Finally, we would like to note that even though the Si_2Te_3 NWs used for this study were grown at high temperature (~850°C) and used Au nanoparticles as catalysts,

other Si_2Te_3 nanostructures such as Si_2Te_3 nanoplates can be grown at lower temperature (~600°C) and without use of Au catalysts and have a potential for CMOS-compatible devices. Stacking of many nanoplates in the vertical direction could also lead to Si_2Te_3 NWs formation.

Conclusion on the PL emission and decay dynamics of the photoexcited carriers in Si_2Te_3 NWs

In conclusion, we have investigated the decay dynamics of the photoexcited carriers in ensembles of Si_2Te_3 NWs as functions of temperature and excitation rate. We have observed a combination of carrier thermalization and possible band structure modification. Our results have revealed the decay dynamics of Si_2Te_3 NWs in a matrix of parameters, which could be used to control the physical characteristics of the material for possible applications in optoelectronics and thermo-electrics.

Chapter 6. Anisotropic optical properties of single Si_2Te_3 nanoplates

In this chapter, we present the anisotropic optical properties of Si_2Te_3 NPs by combining a set of experiments and theoretical calculations. The reflection and Raman spectroscopies are explored by various measurement configurations. Temperature- and polarization-dependent measurements are also conducted. At temperatures below 150 K, a direct band structure is observed with a band gap value of 2.394 eV at 7 K. Polarized reflection measurements at different temperatures show an anisotropic behavior that is related to an anisotropy in the dielectric functions along different crystal directions due to the orientation of the Si-Si dimer. Similarly, polarized Raman scattering measurements also indicate an anisotropic absorption property. The measured polarized Raman and reflection results agree well with the first-principles calculations, which reveals the role of the Si-Si dimer orientations.

Optical setup for measurements of single Si_2Te_3 NPs.

Si_2Te_3 NPs are synthesized by the CVD method, which was described in chapter 3. In optical studies, the reflection and Raman measurements are conducted by using a spectrometer (Horiba iHR550) and charged coupled device camera (Horiba Jobin-Yvon Synapse). In the reflection measurement, the incident white light source is from a Xenon arc lamp with a broad, unpolarized spectrum from 350 to 1000 nm. The incident light is focused onto a single Si_2Te_3 NP via a 20x objective lens, and the reflection is collected by the same lens. For the polarized reflection measurement, the reflected light from a single Si_2Te_3 NP is analyzed by a linear polarizer (Thorlabs, LPVISC100-MP2) before being dispersed by the spectrometer. In the Raman measurements, a single Si_2Te_3 NP is excited by a 488 CW laser (Coherent Sapphire SF 488) via the 20x objective lens. The reflected Raman signal is

collected by the same objective lens, dispersed, and analyzed by the spectrometer and camera. The 488 nm excitation laser is filtered by a notch filter (Semrock 488 nm laser clean-up filter) from the excitation side and by a long-pass filter (488 nm ultra-steep long-pass edge filter) from the detection side. For the polarized Raman measurements, the incident excitation laser is polarized by a half waveplate (Thorlabs AHWP05M-600) for different incident linear polarizations. For low-temperature measurements, the Si_2Te_3 NP temperature (7-293 K) is controlled by using a closed-cycle cryostat (Janis model CCS-XG-M/204N).

The morphology of the Si_2Te_3 NPs is characterized by scanning electron microscopy (SEM, Nova 650), as presented in Figure 37 (b). The NPs appear as a uniform hexagonal structure approximately 20 - 40 μm wide and 100 - 300 nm thick. Figure 37 (c) shows the X-ray diffraction pattern of the Si_2Te_3 NPs. The pattern indicates a series of diffraction peaks at 26.5°, 27.5°, 36.1°, 40.2°, 54.5°, and 60.5°, which correspond to the indices (004), (112), (114), (006), (008) and (118) of Si_2Te_3, respectively. The strong diffraction peak at 26.5° reveals that the growth of the Si_2Te_3 NPs is along the (001) direction. The results of the lattice structure study match well with previous studies. Figure 37 (d) shows the absorption (blue) and the photoluminescence (PL) emission (red) curves of a single Si_2Te_3 NP. The Si_2Te_3 NP exhibits a strong and broad absorption spectrum with a maximum around 2.25 eV, which is close to the band gap of bulk Si_2Te_3 of 2.21 eV at room temperature. The broad absorption spectrum that extends from orange to near infrared is a result of the inter-band absorption of the Si_2Te_3 NP. The PL emission from the Si_2Te_3 NP also exhibits a broad spectrum in the near-infrared region, which indicates a defect-related emission. This result is similar to previous studies where the PL emission is mainly attributed to recombination at trap states above the valence band.

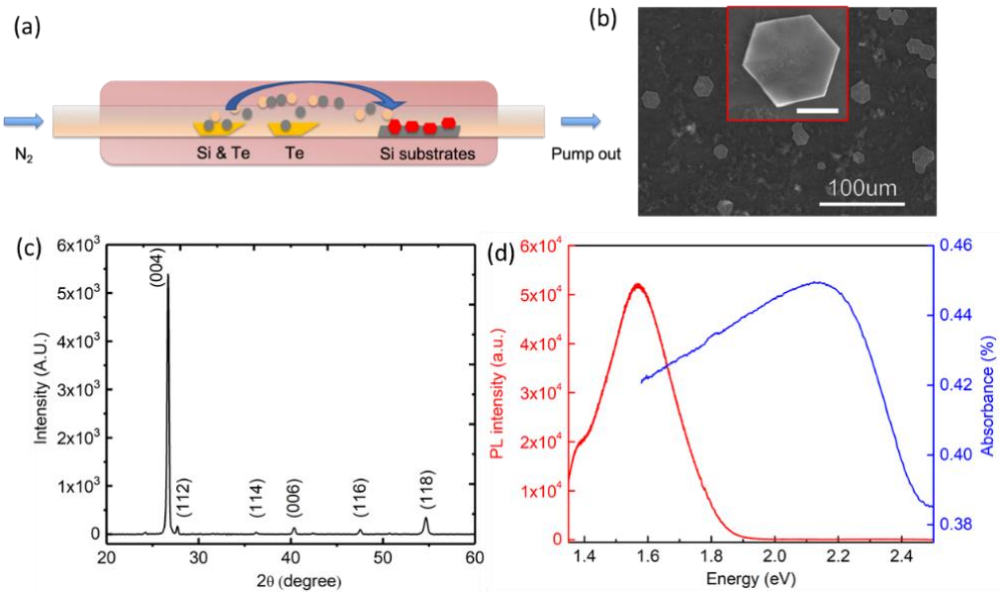

Figure 37: Growth and characterization of Si_2Te_3 NPs. (a) Schematic of the CVD synthesis process for synthesis of the Si_2Te_3 NPs. (b) SEM image of the Si_2Te_3 NPs, the inset (scale bar: 5 μm) is an enlarged image of a single NP. (c) Measured XRD pattern of the Si_2Te_3 NPs. (d) Typical absorption and emission curves of Si_2Te_3 NPs at room temperature.

Temperature-dependent light reflection and electronic bandgap of single Si_2Te_3 NPs

Figure 38 (a) shows a typical low-temperature (7 K) unpolarized reflection spectrum of a single Si_2Te_3 plate. The value of the reflectance is calculated by the following equation:

$$Reflection = \frac{I - I_{noise}}{I_{sub} - I_{noise}}$$

Here I, I_{sub} and I_{noise} are the reflected light intensities from the NP, silicon substrate, and camera thermal noise, respectively. To verify our measurement, Figure 38 (a) also shows a reflection spectrum (dashed black curve) of the incident light on the silicon substrate ($I = I_{sub}$ in this case). As expected, the reflection from the silicon is close to 100%, after normalization to the same substrate. The reflection spectrum from a single Si_2Te_3 NP shows two interesting features. First, above the energy of approximately 2.38 eV the, reflectance value is smaller than 100%. This indicates that above this energy (2.38 eV), the incident photons are absorbed by the NP. This observation hints at the idea that the band gap of a Si_2Te_3 NP at 7 K is near 2.38 eV and that photons above this energy will be absorbed. The

absorbed photons then promote electrons from the valence band to the conduction band or other defect centers to form excitonic states, which are subsequently annihilated to emit photons. Second, below the energy of 2.38 eV, the normalized reflectance value is greater than 100%, which indicates that additional light is emitted from the NP. It is very likely that the emitted light, such as PL, results from absorption at an energy larger than the band gap and is followed by a re-emission process. For instance, a high-energy photon is absorbed to promote an electron to an excited state, which can then be relaxed or scattered by defects or phonons before returning to the ground state and emitting a photon at lower energy. This is consistent with previous observations that Si_2Te_3 has complicated defect/surface states that can result in PL emission in the 1.37 - 2.05 eV range, as shown in Figure 37 (d).

To further understand the band structures of single Si_2Te_3 NPs, we performed the temperature- dependent reflection spectroscopy. Figure 38 (b) shows the reflection spectra from a single plate, which are measured at several temperatures between 7 K and 290 K. Indeed, the data in Figure 38 (b) indicate several interesting properties. First, below 150 K, there are clear energy redshifts of the reflection spectra as the temperature increases. Specifically, when the temperature increases from 7 to 150 K, the crossing point between the reflection spectrum and the horizontal line (at 100% reflection) decreases from 2.38 eV to 2.32 eV. This is a strong indication of the bandgap shrinkage of Si_2Te_3 NPs due to an increasing temperature. Second, at temperature above 150 K, it is very abnormal that the crossing point between the reflection spectrum and the horizontal line (at 100% reflection) suddenly jumps to 2.44 eV and remains at this energy as the temperature approaches the room temperature of 290 K. This observation is consistent with previous studies that the band structures of Si_2Te_3 nanostructures exhibit an abrupt change as the temperature transits

through a critical temperature around 150 K. The mechanism of such a transition is not exactly clear at this moment. Nevertheless, there have been two possible explanations, including a modification of the band structures due to a reorientation of the Si-Si dimers and the domination of the defect/surface-related states at high temperatures.

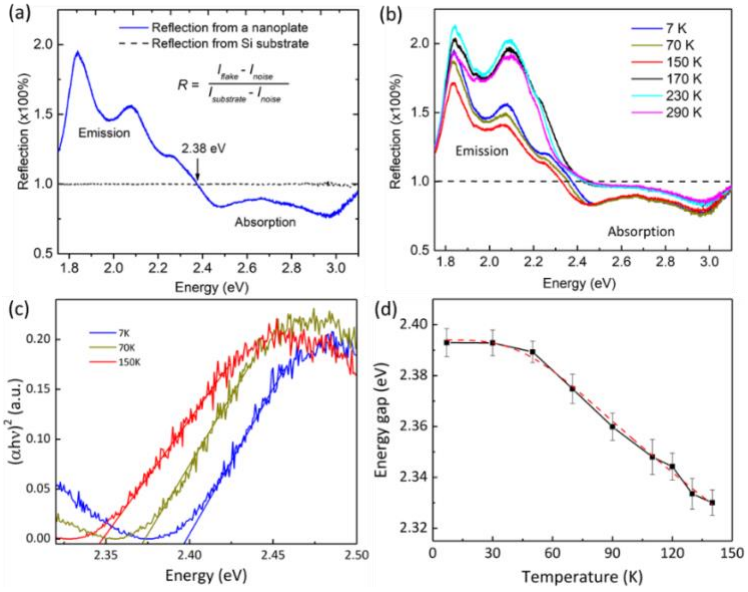

Figure 38: Temperature-dependent reflection spectroscopy (a) Reflection spectra from a single Si_2Te_3 NP at 7 K (solid, blue) and from a Si substrate (dashed, black). (b) Reflection spectra measured at different temperatures. The black dashed line indicates a reference value where the NP is absent. (c) Tauc plots at several representative temperatures. (d) Extracted band gap energy as a function of the temperature. The red dashed line is fit to the extended Varshni equation.

The reflection spectra at temperatures below 150 K presented in Figure 38 (a) and (b) hint at the idea of transition energies between the absorption to emission processes but do not yield accurate band gap energy values. To extract the value of the band gap energy, we employ a Tauc plot, which is often used to determine the optical band gaps of semiconductors. In a Tauc plot, the absorbance is calculated from the reflectance, and the intercept with the x-axis of the linear fit in the absorption edge region yields the value of the band gap energy (Figure 38 (c)). Further, in a Tauc plot the vertical axis represents the quantity $(\alpha hv)^n$, where α is the absorption coefficient and hv is the photon energy. In this

quantity, the exponent n represents the nature of the transition, i.e $n = 2$ for direct band gap transitions and $n = 1/2$ for indirect band gap transitions. Previous work by Bletskan et al. indicated an indirect band gap value of 2.13 eV for crystalline Si_2Te_3 at room temperature. Roma et al.6 has also shown that the stress has a strong effect on the band gap energy as well as the nature of the transition (i.e., direct or indirect). Earlier work by Shen et al.[106] also demonstrated an interesting variability of the Si_2Te_3 band structures with respect to the orientation of the Si-Si dimers. In our measured data, while the Tauc plot for $n = 1/2$ (indirect transition) does not offer a meaningful result, the plot for $n = 2$ (direct transition) indicates a band gap value that is close to the crossing point between the reflection spectrum and the horizontal line, as described in Figure 38 (b). The fits to the Tauc plots in Figure 38 (c) at temperatures of 7, 70 and 150 K result in band gap energy values of 2.394, 2.372 and 2.345 eV, respectively. It is interesting to note that in an earlier work by Wu et al., the authors showed a comparable redshift of approximately 30 meV for the free exciton energy level in a Si_2Te_3 NP ensemble when the temperature increases from 10 – 90 K. Indeed, if we compare the bandgap energy value of 2.394 eV at 7 K in this work with the free exciton energy level at 10 K as reported by Wu et al., one can estimate an approximate exciton binding energy of 150 meV for Si_2Te_3 NPs. Figure 38 (d) shows the band gap energy values obtained by fitting the Tauc plots for temperatures from 7-150 K. The red, dashed curve is the fit following the extended Varshni equation:

$$E_g(T) = E_g(0) - \frac{\alpha T^4}{\beta + T^3}$$

where $E_g(0)$ and $E_g(T)$ are the bandgap energies at temperatures 0 and T, respectively, and α and β are constants to be determined. The fitting yields a band gap energy $E_g(0) = 2.396 \pm 0.002$ eV and $\alpha = 5.1730E-4 \pm 1.8E-5$, $\beta = 3.35\text{E}5 \pm 6.32\text{E}3$ for

Si_2Te_3 NPs. It is also important to note that at temperatures above 150 K, the Tauc plots do not yield reliable fits to extract band gap energies. Similar to previous studies, this result hints at the idea that at temperatures above 150 K the energy landscape of Si_2Te_3 NPs is complicated, and future additional measurements are needed to probe the band structures.

Anisotropic light reflection from single Si_2Te_3 NPs

To obtain more information from the reflection from a single NP, Figure 39 shows polarized reflection measurements. A single NP is excited by an unpolarized incident light source, and the reflected spectra are analyzed by a linear polarizer. Figure 39 (a) shows a clear analyzer angle dependence of the reflected intensity at 7 K. In this measurement, we are interested in the absorption part of the spectrum, i.e., at the energies above 2.39 eV. Figure 39 (b) plots the reflectance value at a fixed energy of 2.55 eV as a function of the linear analyzer angles at different temperatures. The highest reflectance is observed at 21^o, and the lowest reflectance is observed at 111^o, where the angles are relative to a predefined vertical direction. The result of the polarized reflection indicates an optical anisotropy behavior of the single Si_2Te_3 NP. The anisotropy of the optical absorption of a single Si_2Te_3 NP has a close relationship with the anisotropy of the dielectric functions along different crystal directions, as we will demonstrate later in a computational study. In addition, the anisotropy of the dielectric functions is closely related to the orientation of the Si-Si dimers; therefore, our observed absorption result aligns well with previous studies.

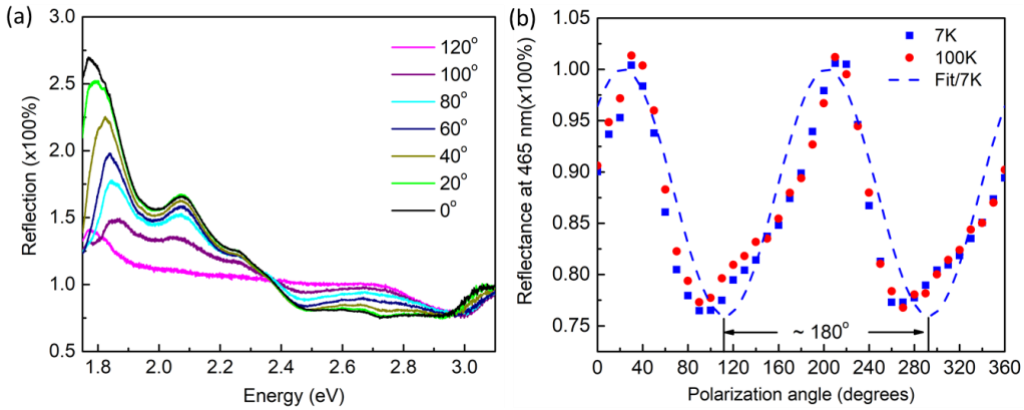

Figure 39: Anisotropic optical absorption for single NPs. (a) Reflection spectra at various analyzer angles at 7 K. (b) Reflectance measured at 2.55 eV at different temperatures and polarization angles. The dashed curve represents the fit by using a cosine function.

Raman scattering study of Si_2Te_3 NPs

To further understand the anisotropy in optical processes, we perform temperature- and polarization-dependent Raman scattering measurements. Figure 40 (a) shows a typical Raman spectrum, which is measured at 20 K with a 30-second acquisition time. In this measurement, several resonant modes are observed. A doublet pattern appears at 130.5 and 154.1 cm^{-1} from the A_{1g} modes. This is similar to a previous measurement from single Si_2Te_3 NPs by Keuleyan et al [105]. In their work, Keuleyan et al. have reported two additional peaks at 275.6 cm^{-1} and 484 cm^{-1} from E_g modes. In our measurement, however, we observe several additional relatively weak peaks at 223.4, 336.5, 486.4, and 506.4 cm^{-1}. Figure 40 (b) presents a Raman scanning measurement from a single Si_2Te_3 NP at room temperature. The inset shows an optical image of the NP, and the dashed red line indicates the scanning across the NP. The scan step is 500 nm, which is approximately equal to the optical resolution, and the acquisition time is 10 seconds. We also note that to avoid heating and oxidation issues at room temperature, we avoid using a long acquisition time for each spot; therefore, several scattering peaks with lower intensity do not appear in this measurement. Nevertheless, the doublet pattern at 130.5 and 154.1 cm^{-1} shows a persistently uniform scattering profile across

the NP, indicating the high quality of the Si_2Te_3 sample. Further, we observe that the Raman frequencies at the edge of a single plate are essentially the same as those at the center of the NP. This observation indicates that, perhaps due to the relatively thick NPs used in our experiment, there is no strong evidence of edge states, as previously observed in other 2-D nanomaterials such as MoS_2 and WSe_2. In any case, if a single Si_2Te_3 NP is thinned down (by mechanical exfoliation, for example) to a thickness of a few monolayers, then it is possible to study the edge states in these materials.

Figure 40 (c) shows the Raman peak position of an A1g peak from a single Si_2Te_3 NP at various temperatures. It is interesting that at temperatures from 7 to 150 K, the peak position shifts from 151.7 cm^{-1} to 149.7 cm^{-1} and remains at this frequency in the temperature range of 150-290 K. In addition, when the temperature increases, we observe that the shape of the Raman peak (not shown here) does not change. Indeed, Raman mode variation at different temperatures has been observed in other 2-D materials and is related to thermal expansion. However, for Si_2Te_3 NPs, there could be two reasons. First, the divergence behavior of the Raman peak at temperatures below 150 K is related to the thermal expansion of the relatively large thickness of the plate. As the temperature increases, the anharmonicity of the temperature expansion and the volume of the plate reach a saturation point before the lattice becomes stable. Second, the Raman shift is related to the band structure, which in turn is related to the orientation of the Si-Si dimers. The latter reason is supported by the reflection measurements and the band structure findings discussed above, where there is an abrupt change in the reflection and band gap energy at approximately 150 K.

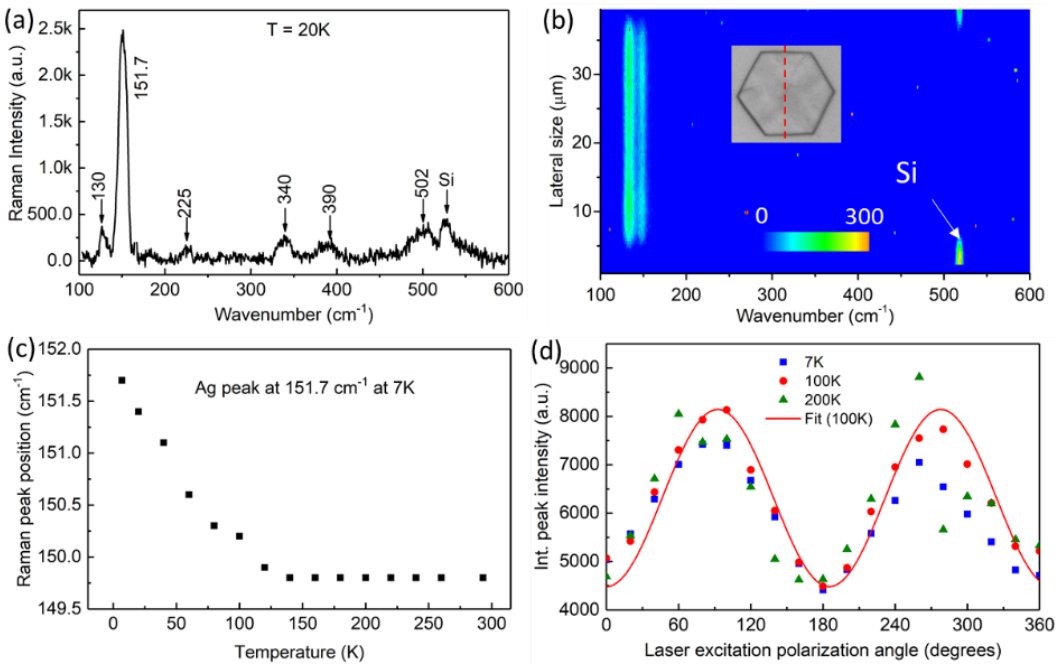

Figure 40: Temperature-dependent and polarized Raman spectroscopy of single Si_2Te_3 NPs. (a) Raman spectrum of a single Si_2Te_3 plate at 7 K. (b) Scanning Raman measurement across a single plate as indicated in the inset. (c) Temperature-dependent Raman peak position measured from 7 K to 290 K. (d) Polarization excitation-dependent Raman intensity. Both (c) and (d) correspond to the peak that appear at 151.7 cm^{-1} at 7 K.

Further, the Raman frequency of a single Si_2Te_3 NP is closely related to the crystal structure, including the orientation of the Si-Si dimers, as we will discuss in the computational study below. In such a case, one would expect a polarization dependence of the Raman signal. Figure 40 (d) shows the polarization-excitation dependent Raman integrated intensity of the peak at 151.7 cm^{-1} at several different temperatures. In this experiment, the laser excitation is linearly polarized by a half waveplate before being focused onto the sample. Similar to the reflection measurement data presented in Figure 39 (b), the Raman signal is polarized by 90°. The degree of polarization, which is defined as $P = \frac{I_{max}-I_{min}}{I_{max}+I_{min}}$, where I_{max} and I_{min} are the maximum and minimum intensities, respectively, is approximately 30%. The anisotropy in the Raman scattering intensity results from the anisotropic absorption coefficient of Si_2Te_3

NPs along different crystal directions, which is influenced by the orientation of the Si-Si dimers.

Conclusion of the anisotropic optical properties of Si_2Te_3 NPs

In conclusion, in this work we study the anisotropic optical properties of single CVD-grown Si_2Te_3 NPs. Polarized reflection and Raman spectroscopies of single Si_2Te_3 NPs at various temperatures are presented. We observe the semiconducting Si_2Te_3 direct band gap at 2.394 eV at 7 K and an estimated free exciton energy of 150 meV. Polarized reflection and Raman measurement results are related to the anisotropy in the orientation of the Si-Si dimer and the dielectric response functions along different crystal directions. Our study thus indicates interesting structural and optical properties of Si_2Te_3 nanostructures, which hold great potential for applications in optoelectronics and chemical sensing, especially because these materials have a clear advantage of compatibility with silicon-based devices.

Chapter 7. Si_2Te_3 thin films and potential applications

In previous chapter, we have discussed the synthesis, morphological controls, and electrical/optical properties of Si_2Te_3 the NPs and NWs. Although, as an emerging 2-D nanomaterial, the most critical parameter is the thickness reduction and potential applications. In this chapter, ultrathin film (sub 10 nm thick) fabrication and potential applications of Si_2Te_3 will be discussed.

2-D layered thin film fabrication techniques.

The fabrication of 2-D ultrathin films can be achieved by several techniques. The direct way to reduce a NP thickness is the parameter control during the synthesis process. The reduction of the precursor quantity and the growth time are reasonable approaches; however, they are not reliable when applied to Si_2Te_3 because of a single heating zone tube furnace in our CVD method. On the other hand, a mechanical exfoliation is another quick and convenient technique to reduce the thickness of Si_2Te_3 NPs. Mechanical exfoliation has been a popular technique to reduce the thickness of the 2-D materials since the discovery of graphene, which is an atomically thin layer of graphite. Indeed, graphene was first demonstrated via the mechanical exfoliation and this original work earned the Nobel Prize in 2010. There is also a chemical exfoliation technique, and, like mechanical exfoliation, both techniques rely on the weak Van der Waals' force between the neighboring atomic layers.

Direct mechanical exfoliation of Si_2Te_3 NPs.

We employed the mechanical exfoliation technique (Figure 2) to fabricate ultrathin Si_2Te_3 film. First, we used a direct exfoliation method to peel-off Si_2Te_3 thin films from thick NPs. An adhesive tape is initially stuck onto one edge of the sample substrate. A small force

is applied parallel to the side of the substrate's surface from the first applied edge to the opposite edge. The purpose of this step is to make sure the tape fully adheres on the substrate. After sticking the tape to the substrate, the vertical force of one's hand will be applied from the sample's top. The exfoliation speed is an important parameter that influences the quality of the thin films. If the tape is exfoliated at a slow speed, it may damage the films and only exfoliates parts from NPs. Moreover, there could be residual organic paste (which comes directly from the adhesive substance of the tape) on the surface of the sample. Therefore, after a large number of tests, we figured it out the most suitable speed to finish the exfoliation is to peel the tape in half a second. In our procedure, several tapes were tested for the exfoliation, and we came to a conclusion that a simple scotch tape (Scotch Brand Magic Tape) and VWR tape (VWR general-purpose cleanroom vinyl tape) can be used together to improve the quality and the efficiency of the exfoliation procedure. A simple scotch tape has a low adhesive force and is hard to peel the NPs from the original sample (the Van der Waals interaction between the layers more significant than the tape adhesive). A VWR tape has good adhesive ability to stick on the top of the sample, but some organic residual will remain on the thin films after the exfoliation. Therefore, a VWR tape is first applied to exfoliate the NPs, and then a scotch tape is used to pick up the organic residual on the substrate.

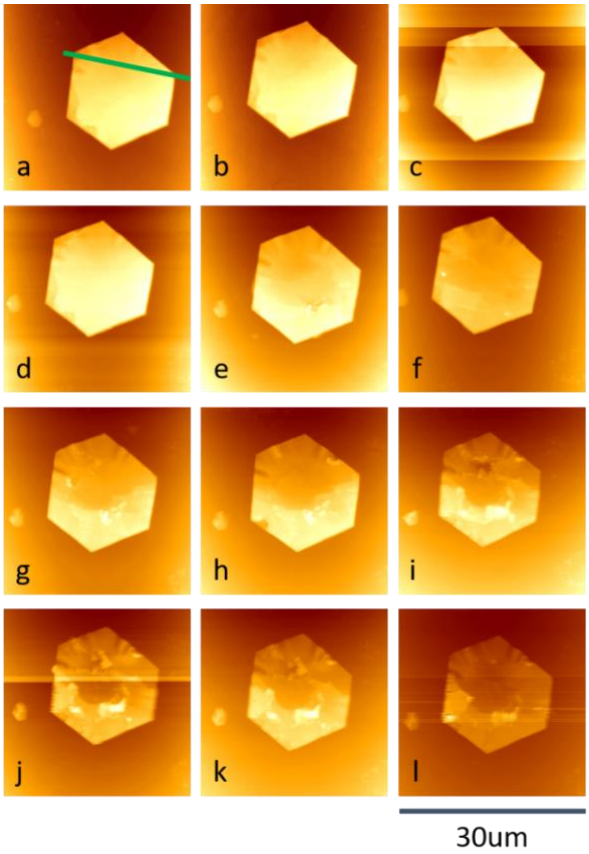

Figure 41: AFM images of a same NP after a number of successive exfoliations. (a) Original sample without exfoliation. (b) after 50 times; (c) 100 times; (d) 150 times; (e) 200 times; (f) 250 times; (g) 300 times; (h) 350 times; (i) 400 times; (j) 405 times; (k) 410 times; (l) 415 times; (m) 419 times.

The results of the mechanical exfoliation procedure are shown in Figures 41 and 42. Figure 41 shows the AFM images of a NP, which were measured after a series of successive exfoliations. Figure 42 (a) shows the thickness of the sample, which measured through the green line shown in Figure 41 (a). Figure 42 (b) shows the final thickness of the NP after a total of 419 exfoliations. As shown in Figure 42 (a), the sample's thickness is reduced from around 850 nm to 5 nm by after the exfoliation sequence. After each exfoliation, the thickness of the NP reduced between 0 to 10 nm. The final rough surface is a result of the organic residual which remains on the top of the NP.

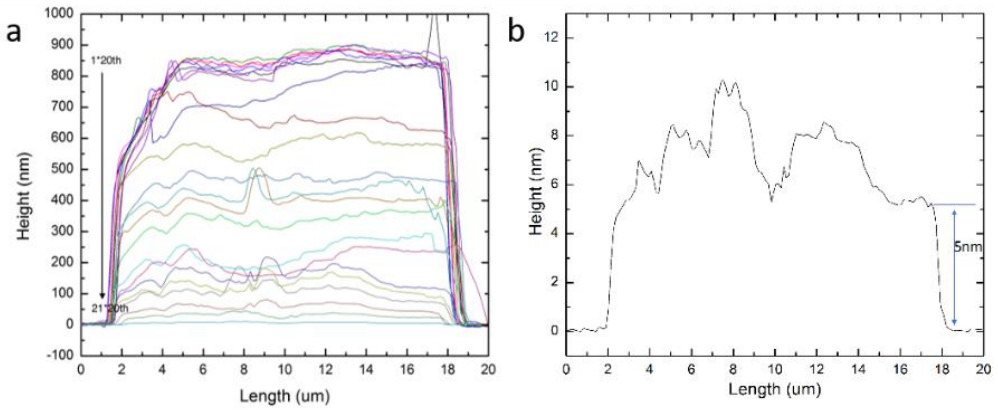

Figure 42: Thickness reduction, as measured by AFM, after a number of successive exfoliations. (a) Thicknesses measured after each 20-successive-exfoliation, (b) A final thickness of the NP is around 5 nm.

Transferred exfoliation of Si_2Te_3 NPs.

A challenge of the direct mechanical exfoliation method is to locate the thinned Si_2Te_3 NPs under an optical microscope after each peel-off. Another mechanical method of exfoliation is to transfer the thin films, which are attached to the tape after the peeling, to another substrate such as SiO_2. For our studies, we transferred the exfoliated Si_2Te_3 thin films to Si substrate which is coated by a 100 nm SiO_2 film.

In order to avoid the organic residual and the moisture contents, the surface of a transferred SiO_2 substrate is strictly treated by the piranha solution (H_2SO_4:HNO_3=3:1, and heat for 30 minutes at 50^{o}C) then washed and dried by nitrogen gas. Furthermore, a typical way to increase the surface energy to improve the atomic force between the substrate and the Si_2Te_3 layers is to treat the substrate by a plasma generator. However, in this project, a SiO_2 transfer substrate treated by the plasma generator will generate more organic residual from the tape during the exfoliation. This in turn causes more damage to the Si_2Te_3 transferred films. Figure 43 (a) shows a substrate which was treated with the plasma and Figure 43 (b) shows

the substrate which was not treated by the plasma. Clearly, after the plasma treatment the substrate did not adhere nicely the Si_2Te_3 thin films.

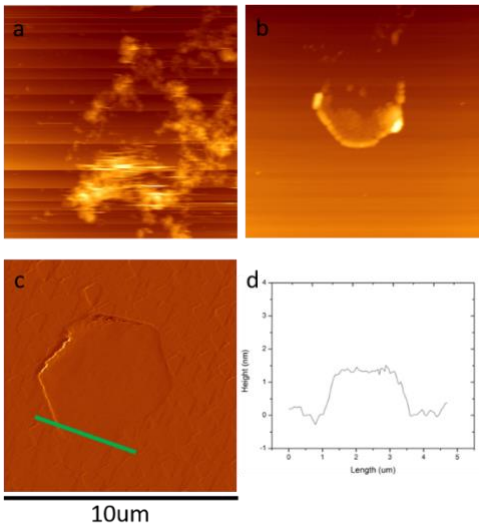

Figure 43: AFM images of NPs on the transferred substrate after the exfoliations. (a) AFM image of the sample after the plasma treatment; (b) AFM image of the sample without the plasma treatment; (c) An exfoliated NP on the SiO_2 substrate; (b)The thickness measured along the green line shown in (c).

A general procedure for transferred exfoliation is to apply a tape on to an original NP sample and then on a transferred substrate. The expectation is to peel very thin, in order of a few atomic layers, films from the original substrate then transfer them to a new substrate. The exfoliation results are shown in Figure 43 (c) and (d). For this method, it happens that a large number of NPs can break into pieces. Only a few NPs can remain in their original hexagonal shape. The best flake obtained in our experiments after transferred to a SiO_2 substrate was round 1.5 nm thick as shown in Figure 43 (d).

In conclusion, the transferred exfoliation method is more reliable for producing ultrathin film, and the quality of the exfoliated thin film is much better than the direct exfoliation method.

Electrical properties of single Si_2Te_3 NPs

Electrical property measurements were set to study single Si_2Te_3 NPs, which were synthesized on a highly doped n-type Si wafer substrate. A conductive AFM tip was used as an electrode to measure the electrical current through a NP. Two different electrical measurement setups were employed as we describe below.

Current measurement by using a conductive AFM tip.

The first set up to measure an electrical current from a single Si_2Te_3 NP is sketched in Figure 44 below. For this study, a NP was scanned by an AFM conductive tip in the contact mode. Once the morphology of the NP is identified, the AFM tip is controlled to scan a small region of the NP (~100 nm in size). The tip is then stop on the surface of the NP and be used as an electrode of the circuit to measure an I-V curve.

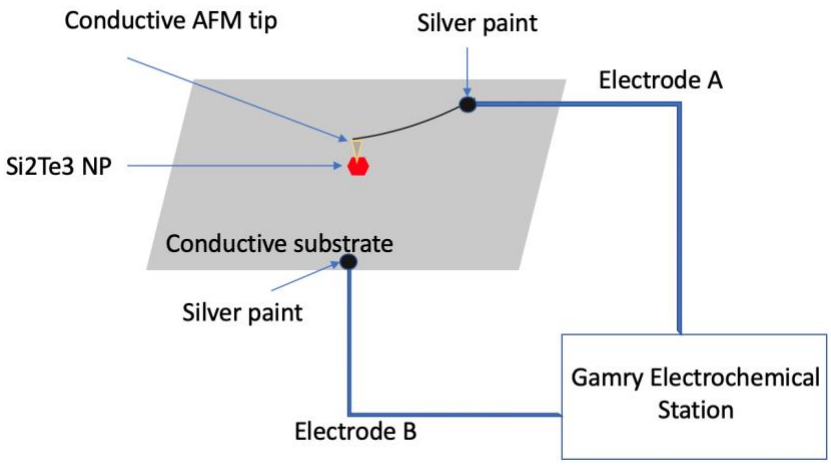

Figure 44: Schematic of a setup for an electrical measurement from a single Si_2Te_3 NP.

The result for the electrical property measurements is shown in Figure 45 below. The single Si_2Te_3 NP in this study was approximately 15 μm diameter and 500 nm thick. Figure 45 (b) shows the I-V measurements at two spots A and B as indicated in Figure 45 (a). The I-V curves show a resistant switching behavior from a high-resistant state to a low-resistant

state. After the current set, the resistance of the NP cannot stably keep at the low resistant state. It is important to note that once the AMF tip approach to the NP is achieved, at the highest voltage the current curvilinear decreases to zero, and the resetting phenomenon cannot be observed. This is because the contact point between the NP and the AFM tip is very small (AFM tip size is less than 10 nm in diameter). Therefore, the highest voltage for this measurement set up is limited to 0.6 V in order to avoid a tip melting from the high heat generated by the high current density. From the I-V measurements of this single NP we did not observe the significant resistant set and reset phenomena. First, a low voltage cannot motivate the switching phenomenon. Second, the switching behavior, if any, can only appear on a very small area on the NP and can quickly be recovered. To verify these two hypotheses, we have conducted a second set I-V curve measurement, by reversing the AFM tip before making contact with the NP as schematically illustrated in Figure 46.

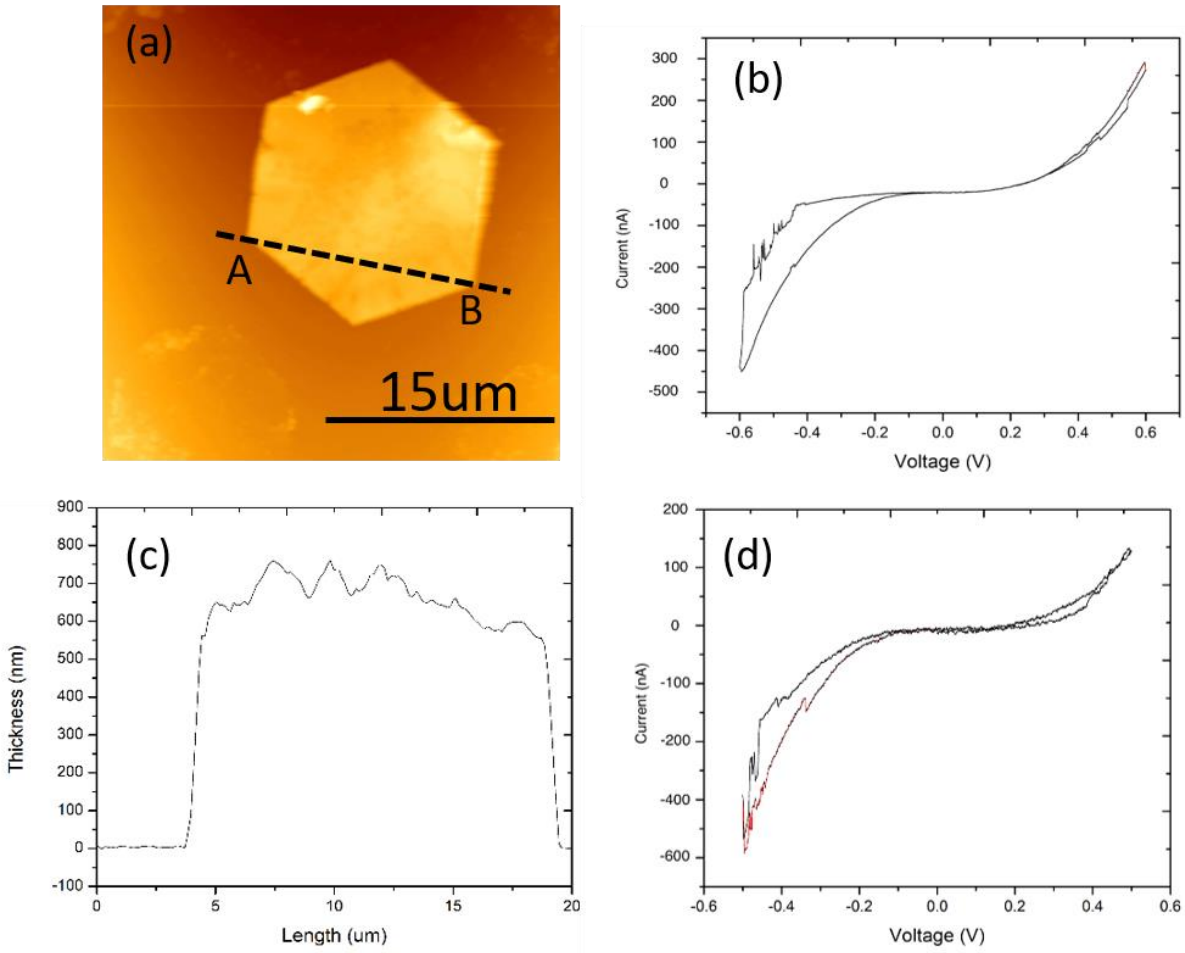

Figure 45: AFM images of a transferred Si_2Te_3 thin film and its electrical switching behavior. (a) Morphology of a single Si_2Te_3 NP scanned by the AFM; (b) Cyclic I-V measurement for spot A; (c) Thickness measured for the line draw on (a); (d) Cyclic I-V measurement for spot B.

Current measurement by using a reversed AFM tip

In this second set measurement the AFM tip is flipped to increase the surface contact area. In other words, we use the backside of a cantilever beam to contact with the NP instead of the 10 nm tip. The contact area between the electrode and the NP is significantly increased to several tens of μm.

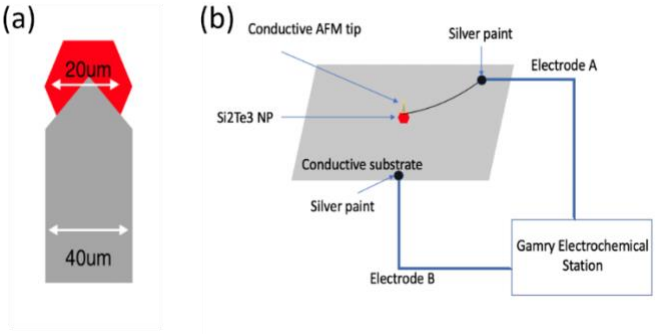

Figure 46: Schematic of a set up for the electrical measurement from a single Si_2Te_3 by a reversed AFM tip. (a) A large view on the cantilever beam contact to the Si_2Te_3 single NP (the width of the beam is 40 μm); (b) Sketch for the I-V measurement.

Figure 46 (b) illustrates how a cantilever beam makes contact with a Si_2Te_3 NP. The cantilever beam is bent to increase the contact area. With this measurement setup, the I-V measurements show a same result as it was observed before for Si_2Te_3 NWs. The resistant set and reset phenomenon can be now observed, as shown in Figure 47.

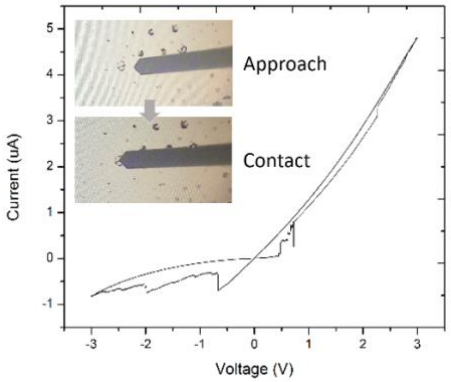

Figure 47: I-V curve for a single NP measurement by using the cantilever beam. The inset shows the tip and the nanoplate.

Chapter 8. Conclusions and outlook

In conclusion, this research can be classified into three parts.

For the fabrication, we have successfully synthesized various Si_2Te_3 nanostructures by using the CVD method. The Si_2Te_3 NPs were directly fabricated by using the tellurium and silicon powders as the precursors. The thicknesses and the sizes of NPs were controlled by adjusting the growing parameters, such as the flowing rate, growing time, chamber pressure, source heating, and the substrate temperatures. Additionally, few-layer Si_2Te_3 NPs were successfully fabricated by using the mechanical exfoliation method. Si_2Te_3 NWs were fabricated by using Au nanoparticles as catalysts and tellurium, silicon powders as precursors. Surface roughness and the size of Si_2Te_3 NWs were controlled by adjusting the various growing parameters based on the vapor-liquid-solid phase transition theory.

We also have conducted electrical and optical measurements on the fabricated NPs and NWs. Electrical measurements showed a switching behavior of Si_2Te_3 NWs. The resistance of Si_2Te_3 NWs can be reversibly switched between high and low resistance states by applying an electric potential along the z-direction of the crystallization. The resistance switching behavior was explained by a phase transition between metallic and semiconducting phases.

For the optical measurements, we have investigated the decay dynamics of the photoexcited carriers in the Si_2Te_3 nanostructures. The results were extracted from low and room temperature PL and time-resolved measurements. We have observed a combination of carrier thermalization and possible band structure modification as functions of temperature and excitation rates. We have also studied the anisotropic optical properties of single NPs by using polarized reflection and Raman spectroscopies. From the reflection measurements,

which were performed at various temperatures, we observed that single NPs exhibit a direct bandgap at approximately 2.394 eV at 7 K and estimated free exciton energy of 150 meV. Polarized reflection and Raman measurement results were related to the anisotropy in the orientations of the Si-Si dimers and the dielectric response functions along different crystal directions.

Results of electrical measurements have revealed that Si_2Te_3 nanostructures are promising candidates for resistive memory devices. Further, thanks to the unique crystal structures of Si_2Te_3, our optical measurements have also hinted at their possible applications in nanoscale optoelectronics, thermo-electrics, and chemical sensing. Additionally, it is important to mention that due to the high sensitivity of Si_2Te_3 to the moisture in a surrounding environment, any future applications of the Si_2Te_3 nanomaterials will have to face a challenge when it comes to packaging and real manufactory use. On the other hand, if compared with the other mature TMDCs such as MoS_2 and WSe_2, Si_2Te_3 nanomaterials still hold many physical properties that need to be explored in the future.

As mentioned in the early chapters, the physical properties of the Si_2Te_3 are highly related to the Si dimer orientations due to the unique crystal structure. The anisotropic optical response is related to the Si dimer orientation either. Hence, the dimer orientation in Si_2Te_3 act a crucial role relates to the physical properties. However, due to the limitations in technique, it is necessary to protect the layered structure from the moisture penetration. The size effect of the dimensional reduction in Si_2Te_3 2-D thin film is not clear in this research project. There is still difficulty in keeping the fabricated thin film alive in the atmosphere.

Recently there has been a great interest in using optical platforms such as optical micro- and nano-cavities to engineer the optical and electronic properties of nanomaterials,

including 2-D TMDCs. The general idea stems from the light-matter interactions that occur at the nanoscale. An optical nanocavity, such as a plasmonic nanocavity formed by a metallic nanoparticle, provides a highly concentrated electromagnetic field (or photonic states) through the localized surface resonance in a small volume. When integrated with a TMDC structure, the TMDC's quantum states level with photonic states allowing the spontaneous emission rate of an emitter to be significantly enhanced through the Purcell effect. Integrating nanomaterials with optical nanocavities extends beyond an engineering challenge, as it offers rich physics of the light-matter interaction at the nanoscale which will eventually lead to exotic properties and applications.

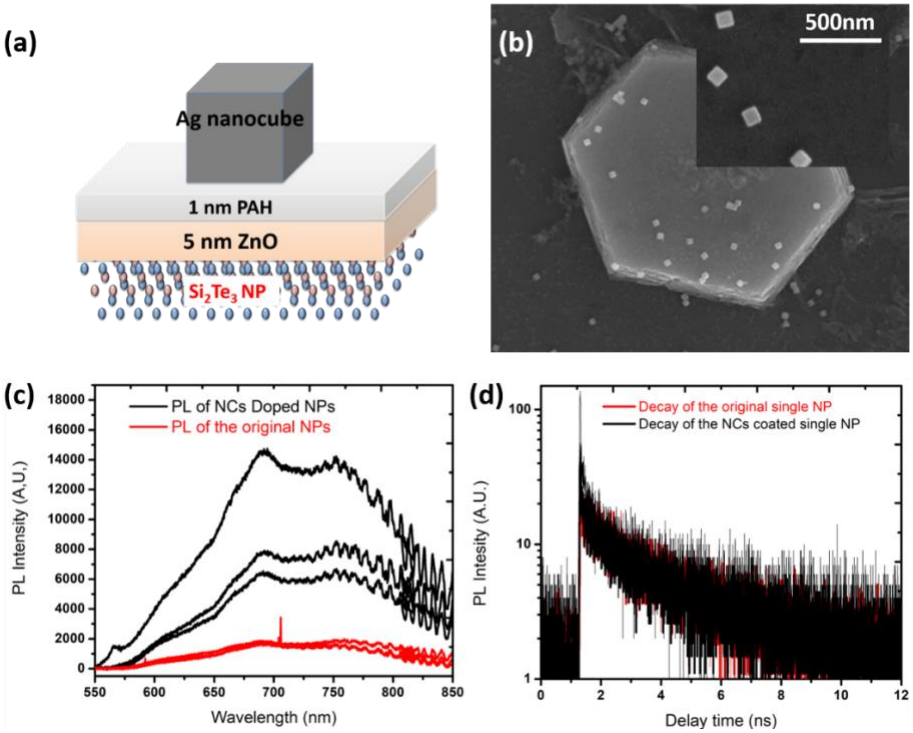

Figure 48: Optical properties of coupled Si_2Te_3 NPs and Ag nanocubes (a) Schematic of a Si_2Te_3 NP integrated with a Ag nanocube; (b) SEM image of an experimentally demonstrated structure. The inset shows an enlarged image of Ag nanocubes on top of a NP; (c) Enhanced PL emission: red shows the PL spectra from as grown Si_2Te_3 NPs and black shows PL spectra from Si_2Te_3 NPs coupled with Ag nanocubes; (d) Decay curves of the as grown Si_2Te_3 NPs (red) and coupled with Ag nanocubes (black).

Aligning with this general trend in recent developments of nanophotonics and especially in quantum optics, we are developing a technique to integrate Si_2Te_3 NPs with plasmonic silver (Ag) nanocubes. Ag nanocubes (size ~ 100 nm) exhibit a strong plasmonic resonance in the 600-800 nm wavelength range. Indeed, such a resonance wavelength range matches perfectly with the PL emission of Si_2Te_3 NPs as shown in Chapter 6. Our preliminary results are shown in Figure 48. Briefly, Si_2Te_3 NPs are coated with a 5 nm ZnO protection layer and followed by the deposition of 100 nm Ag nanocubes. Figure 48 (a) shows a schematic of the structures along with several parameters and Figure 48 (b) shows SEM image of an actual device. The integrated Si_2Te_3/nanocube structure demonstrates a significant PL enhancement as shown in Figure 48 (c). A preliminary time-resolved PL measurement is shown in Figure 48 (d)

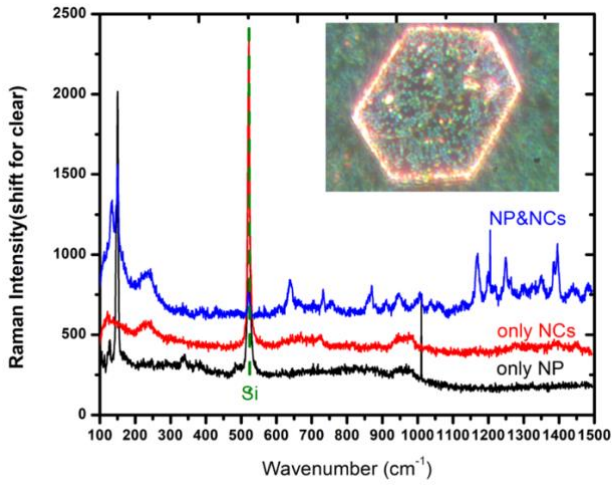

Figure 49: Raman characterization of coupled Si_2Te_3 NPs and Ag nanocubes. Raman spectra of Si_2Te_3 NPs on a silicon substrate (black), Ag nanocubes on silicon substrate (red), and coupled Si_2Te_3 NP/ Ag nanocubes silicon substrate (blue). The inset shows PL/Raman image of a single Si_2Te_3 NP covered by Ag nanocubes.

The Raman scattering spectra of several sample configurations (as grown Si_2Te_3 NP, Si_2Te_3 NP/Ag nanocubes and Ag nanocubes on a Si substrate) are shown in Figure 49. Compare with as grown Si_2Te_3 NP, the Si_2Te_3 NP/Ag nanocube structure exhibit a series of

new vibration peaks from 600 to 1500 cm $^{-1}$. The peaks are observed in this wavenumber range, which are correlated with the nanocube blinking on the NP's surface. The inset of Figure 49 shows an optical image which is a combination of Raman and PL signal from a single NP covered by Ag nanocubes. It appears that the signal (PL and Raman) is very strong and indeed significantly enhanced at locations where Ag nanocubes are situated. This is a result of the enhanced PL/Raman due to the local surface plasmon resonance of the metallic nanoparticles as discussed above. Several recently published works have also reported a similar result of Raman enhancement for 2-D materials and their applications toward the surface-enhanced Raman spectroscopy (SERS) [131][132][133]. Thus, the Si_2Te_3 NP/Ag nanocubes photonic structure hints at a promising alternative application regarding the SERS imaging technique.

References

[1] Pokropivny, V. and Skorokhod, V. (2007). Classification of nanostructures by dimensionality and concept of surface forms engineering in nanomaterial science. *Materials Science and Engineering: C*, 27(5-8), pp.990-993.

[2] Park, J., Nalwa, K., Leung, W., Constant, K., Chaudhary, S. and Ho, K. (2010). Fabrication of metallic nanowires and nanoribbons using laser interference lithography and shadow lithography. *Nanotechnology*, 21(21), p.215301.

[3]] Lei, L. and He, D. (2009). Synthesis of GaN Crystals Through Solid-State Metathesis Reaction Under High Pressure. *Crystal Growth & Design*, 9(3), pp.1264-1266.

[4] Tiwari, J., Tiwari, R. and Kim, K. (2012). Zero-dimensional, one-dimensional, two-dimensional and three-dimensional nanostructured materials for advanced electrochemical energy devices. *Progress in Materials Science*, 57(4), pp.724-803.

[5] Suryanarayana, C. (1994). Structure and properties of nanocrystalline materials. *Bulletin of Materials Science*, 17(4), pp.307-346.

[6] Hu, J., Odom, T. and Lieber, C. (2010). ChemInform Abstract: Chemistry and Physics in One Dimension: Synthesis and Properties of Nanowires and Nanotubes. *ChemInform*, 30(29), p.no-no.

[7] Haghi, A. (2015). Foundations of Nanotechnology - Three Volume Set.

[8] Iijima, S. (1991). Helical microtubules of graphitic carbon. *Nature*, 354(6348), pp.56-58.

[9] Geim, A. (2009). Graphene: Status and Prospects. *Science*, 324(5934), pp.1530-1534.

[10] Marcano, D. C., Kosynkin, D. V., Berlin, J. M., Sinitskii, A., Sun, Z., Slesarev, A., ... & Tour, J. M. (2010). Improved synthesis of graphene oxide. *ACS nano*, 4(8), 4806-4814.

[11] Zhu, Y., Murali, S., Cai, W., Li, X., Suk, J. W., Potts, J. R., & Ruoff, R. S. (2010). Graphene and graphene oxide: synthesis, properties, and applications. *Advanced materials*, 22(35), 3906-3924.

[12] Manzeli, S., Ovchinnikov, D., Pasquier, D., Yazyev, O. V., & Kis, A. (2017). 2-D transition metal dichalcogenides. *Nature Reviews Materials*, 2(8), 17033.

[13] Nath, M., Govindaraj, A., & Rao, C. N. R. (2001). Simple synthesis of MoS_2 and WS_2 nanotubes. *Advanced Materials*, 13(4), 283-286.

[14] Remskar, M., Mrzel, A., Skraba, Z., Jesih, A., Ceh, M., Demšar, J., ... & Mihailovic, D. (2001). Self-assembly of subnanometer-diameter single-wall MoS_2 nanotubes. *Science*, 292(5516), 479-481.

[15] Lee, H. S., Min, S. W., Chang, Y. G., Park, M. K., Nam, T., Kim, H., ... & Im, S. (2012). MoS_2 nanosheet phototransistors with thickness-modulated optical energy gap. *Nano letters*, 12(7), 3695-3700.

[16] Steinhoff, A., Kim, J. H., Jahnke, F., Rösner, M., Kim, D. S., Lee, C., ... & Gies, C. (2015). Efficient excitonic photoluminescence in direct and indirect band gap monolayer MoS_2. *Nano letters*, 15(10), 6841-6847.

[17] Qiao, S., Zhang, B., Feng, K., Cong, R., Yu, W., Fu, G., & Wang, S. (2017). Large lateral photovoltage observed in MoS_2 thickness-modulated ITO/MoS_2/p-Si heterojunctions. *ACS Applied Materials & Interfaces*, 9(21), 18377-18387.

[18] Lu, C. P., Li, G., Mao, J., Wang, L. M., & Andrei, E. Y. (2014). Bandgap, mid-gap states, and gating effects in MoS_2. *Nano letters*, 14(8), 4628-4633.

[19] Vu, Q. A., Fan, S., Lee, S. H., Joo, M. K., Yu, W. J., & Lee, Y. H. (2018). Near-zero hysteresis and near-ideal subthreshold swing in h-BN encapsulated single-layer MoS_2 field-effect transistors. *2-D Materials*, 5(3), 031001.

[20] Yin, Z., Zhang, X., Cai, Y., Chen, J., Wong, J. I., Tay, Y. Y., ... & Yang, H. Y. (2014). Preparation of MoS_2–MoO_3 Hybrid Nanomaterials for Light-Emitting Diodes. *Angewandte Chemie International Edition*, 53(46), 12560-12565.

[21] Tsai, M. L., Su, S. H., Chang, J. K., Tsai, D. S., Chen, C. H., Wu, C. I., ... & He, J. H. (2014). Monolayer MoS2 heterojunction solar cells. *ACS nano*, 8(8), 8317-8322.

[22] David, L., Bhandavat, R., & Singh, G. (2014). MoS_2/graphene composite paper for sodium-ion battery electrodes. *ACS nano*, 8(2), 1759-1770.

[23] Xie, X., Ao, Z., Su, D., Zhang, J., & Wang, G. (2015). MoS_2/Graphene Composite Anodes with Enhanced Performance for Sodium-Ion Batteries: The Role of the Two-Dimensional Heterointerface. *Advanced Functional Materials*, 25(9), 1393-1403.

[24] Choi, S. H., Ko, Y. N., Lee, J. K., & Kang, Y. C. (2015). 3-D MoS_2–graphene microspheres consisting of multiple nanospheres with superior sodium ion storage properties. *Advanced Functional Materials*, 25(12), 1780-1788.

[25] Zhou, X., Wang, Z., Chen, W., Ma, L., Chen, D., & Lee, J. Y. (2014). Facile synthesis and electrochemical properties of two dimensional layered MoS2/graphene composite for reversible lithium storage. *Journal of Power Sources*, 251, 264-268.

[26] Corso, M., Auwärter, W., Muntwiler, M., Tamai, A., Greber, T., & Osterwalder, J. (2004). Boron nitride nanomesh. *Science*, 303(5655), 217-220.

[27] Watanabe, K., Taniguchi, T., & Kanda, H. (2004). Direct-bandgap properties and evidence for ultraviolet lasing of hexagonal boron nitride single crystal. *Nature materials*, 3(6), 404-409.

[28] Watanabe, K., Taniguchi, T., Niiyama, T., Miya, K., & Taniguchi, M. (2009). Far-ultraviolet plane-emission handheld device based on hexagonal boron nitride. *Nature photonics*, 3(10), 591-594.

[29] Kumar, A., Low, T., Fung, K. H., Avouris, P., & Fang, N. X. (2015). Tunable light–matter interaction and the role of hyperbolicity in graphene–hBN system. *Nano letters*, 15(5), 3172-3180.

[30] Kang, S., Prasad, N., Movva, H. C., Rai, A., Kim, K., Mou, X., ... & Banerjee, S. K. (2016). Effects of electrode layer band structure on the performance of multilayer graphene–h-BN–graphene interlayer tunnel field effect transistors. *Nano letters*, 16(8), 4975-4981.

[31] Wang, J. I. J., Yang, Y., Chen, Y. A., Watanabe, K., Taniguchi, T., Churchill, H. O., & Jarillo-Herrero, P. (2015). Electronic transport of encapsulated graphene and WSe_2 devices fabricated by pick-up of prepatterned h-BN. *Nano letters*, 15(3), 1898-1903.

[32] Zhang, J., Yang, Y., & Lou, J. (2016). Investigation of hexagonal boron nitride as an atomically thin corrosion passivation coating in aqueous solution. *Nanotechnology*, 27(36), 364004.

[33] Ebbesen, T. W. (1996). Carbon nanotubes: preparation and properties. *CRC press*.

[34] Yang, Q., Sha, J., Wang, L., Wang, Y., Ma, X., Wang, J., & Yang, D. (2004). Synthesis of MgO nanotube bundles. *Nanotechnology*, 15(8), 1004.

[35] Zhang, Y. F., Tang, Y. H., Zhang, Y., Lee, C. S., Bello, I., & Lee, S. T. (2000). Deposition of carbon nanotubes on Si nanowires by chemical vapor deposition. *Chemical Physics Letters*, 330(1-2), 48-52.

[36] Yang, J., Luo, F., Kao, T. S., Li, X., Ho, G. W., Teng, J., ... & Hong, M. (2014). Design and fabrication of broadband ultralow reflectivity black Si surfaces by laser micro/nano-processing. *Light: Science & Applications*, 3(7), e185-e185.

[37] Khusaimi, Z., Amizam, S., Mamat, M. H., Sahdan, M. Z., Ahmad, M. K., Abdullah, N., & Rusop, M. (2010). Controlled growth of zinc oxide nanorods by aqueous-solution method. *Synthesis and Reactivity in Inorganic, Metal-Organic, and Nano-Metal Chemistry*, 40(3), 190-194.

[38] Yi, M., & Shen, Z. (2015). A review on mechanical exfoliation for the scalable production of graphene. *Journal of Materials Chemistry A*, 3(22), 11700-11715.

[39] Xu, J., Zhang, L., Shi, R., & Zhu, Y. (2013). Chemical exfoliation of graphitic carbon nitride for efficient heterogeneous photocatalysis. *Journal of Materials Chemistry A*, 1(46), 14766-14772.

[40] Sherman, A. (1999). U.S. Patent No. 5,916,365. Washington, DC: U.S. Patent and Trademark Office.

[41] Lee, Y. H., Zhang, X. Q., Zhang, W., Chang, M. T., Lin, C. T., Chang, K. D., ... & Lin, T. W. (2012). Synthesis of large-area MoS_2 atomic layers with chemical vapor deposition. *Advanced materials*, 24(17), 2320-2325.

[42] Tevet, O., Von-Huth, P., Popovitz-Biro, R., Rosentsveig, R., Wagner, H. D., & Tenne, R. (2011). Friction mechanism of individual multilayered nanoparticles. *Proceedings of the National Academy of Sciences*, 108(50), 19901-19906.

[43] Ottaviano, L., Palleschi, S., Perrozzi, F., D'Olimpio, G., Priante, F., Donarelli, M., ... & Lucia, A. (2017). Mechanical exfoliation and layer number identification of MoS_2 revisited. *2-D Materials*, 4(4), 045013.

[44] Li, H., Lu, G., Wang, Y., Yin, Z., Cong, C., He, Q., ... & Zhang, H. (2013). Mechanical exfoliation and characterization of single-and few-layer nanosheets of WSe_2, TaS_2, and $TaSe_2$. *Small*, 9(11), 1974-1981.

[45] Zhang, L., Liang, J., Huang, Y., Ma, Y., Wang, Y., & Chen, Y. (2009). Size-controlled synthesis of graphene oxide sheets on a large scale using chemical exfoliation. *Carbon*, 47(14), 3365-3368.

[46] Xia, Z. Y., Pezzini, S., Treossi, E., Giambastiani, G., Corticelli, F., Morandi, V., ... & Palermo, V. (2013). The exfoliation of graphene in liquids by electrochemical, chemical, and sonication-assisted techniques: A nanoscale study. *Advanced Functional Materials*, 23(37), 4684-4693.

[47] Qi, M., Ren, Z., Jiao, Y., Zhou, Y., Xu, X., Li, W., ... & Bai, J. (2013). Hydrogen kinetics on scalable graphene growth by atmospheric pressure chemical vapor deposition with acetylene. *The Journal of Physical Chemistry C*, 117(27), 14348-14353.

[48] Ling, X., Lee, Y. H., Lin, Y., Fang, W., Yu, L., Dresselhaus, M. S., & Kong, J. (2014). Role of the seeding promoter in MoS_2 growth by chemical vapor deposition. *Nano letters*, 14(2), 464-472.

[49] Jang, J., Son, M., Chung, S., Kim, K., Cho, C., Lee, B. H., & Ham, M. H. (2015). Low-temperature-grown continuous graphene films from benzene by chemical vapor deposition at ambient pressure. *Scientific reports*, 5(1), 1-7.

[50] Saenz, G. A. L., Biswas, C., Yamaguchi, H., Villarrubia, C. N., Mohite, A. D., & Kaul, A. B. (2016). Effects of synthesis parameters on CVD molybdenum disulfide growth. *MRS Advances*, 1(32), 2291-2296.

[51] Losurdo, M., Giangregorio, M. M., Capezzuto, P., & Bruno, G. (2011). Graphene CVD growth on copper and nickel: role of hydrogen in kinetics and structure. *Physical Chemistry Chemical Physics*, 13(46), 20836-20843.

[52] Lemme, M. C., Li, L. J., Palacios, T., & Schwierz, F. (2014). Two-dimensional materials for electronic applications. *MRS Bulletin*, 39(8), 711-718.

[53] Gong, C., Hu, K., Wang, X., Wangyang, P., Yan, C., Chu, J., ... & Li, L. (2018). 2-D nanomaterial arrays for electronics and optoelectronics. *Advanced Functional Materials*, 28(16), 1706559.

[54] Oh, S. W., Bang, H. J., Bae, Y. C., & Sun, Y. K. (2007). Effect of calcination temperature on morphology, crystallinity and electrochemical properties of nano-crystalline metal oxides (Co_3O_4, CuO, and NiO) prepared via ultrasonic spray pyrolysis. *Journal of Power Sources*, 173(1), 502-509.

[55] Kuang, Q., Wang, X., Jiang, Z., Xie, Z., & Zheng, L. (2014). High-energy-surface engineered metal oxide micro-and nano-crystallites and their applications. *Accounts of chemical research*, 47(2), 308-318.

[56] Boltersdorf, J., King, N., & Maggard, P. A. (2015). Flux-mediated crystal growth of metal oxides: synthetic tunability of particle morphologies, sizes, and surface features for photocatalysis research. *Cryst Eng Comm*, 17(11), 2225-2241.

[57] Wang, X., & Li, Y. (2006). Solution-based synthetic strategies for 1-D nanostructures. *Inorganic Chemistry*, 45(19), 7522-7534.

[58] Arafat, M. M., Dinan, B., Akbar, S. A., & Haseeb, A. S. M. A. (2012). Gas sensors based on one dimensional nanostructured metal-oxides: a review. Sensors, 12(6), 7207-7258.

[59] Song, M. K., Park, S., Alamgir, F. M., Cho, J., & Liu, M. (2011). Nanostructured electrodes for lithium-ion and lithium-air batteries: the latest developments, challenges, and perspectives. *Materials Science and Engineering: R: Reports*, 72(11), 203-252.

[60] Shen, J., Qiao, Z., Zhang, K., Wang, J., Li, R., Xu, H., ... & Nie, F. (2014). Effects of nano-Ag on the combustion process of Al–CuO metastable intermolecular composite. *Applied thermal engineering*, 62(2), 732-737.

[61] Huang, M. H., Mao, S., Feick, H., Yan, H., Wu, Y., Kind, H., ... & Yang, P. (2001). Room-temperature ultraviolet nanowire nanolasers. *Science*, 292(5523), 1897-1899.

[62] Akinwande, D., Brennan, C. J., Bunch, J. S., Egberts, P., Felts, J. R., Gao, H., ... & Liechti, K. M. (2017). A review on mechanics and mechanical properties of 2-D materials - Graphene and beyond. *Extreme Mechanics Letters*, 13, 42-77.

[63] Yu, Z., Ong, Z. Y., Li, S., Xu, J. B., Zhang, G., Zhang, Y. W., ... & Wang, X. (2017). Analyzing the Carrier Mobility in Transition-Metal Dichalcogenide MoS_2 Field-Effect Transistors. *Advanced Functional Materials*, 27(19), 1604093.

[64] Liu, Y., Duan, X., Huang, Y., & Duan, X. (2018). Two-dimensional transistors beyond graphene and TMDCs. *Chemical Society Reviews*, 47(16), 6388-6409.

[65] Ansari, N., Mohebbi, E., & Gholami, F. (2020). Nearly perfect and broadband optical absorption by TMDCs in cover/TMDC/spacer/Au/substrate multilayers. *Applied Physics B*, 126(1), 3.

[66] Hu, Z., Wu, Z., Han, C., He, J., Ni, Z., & Chen, W. (2018). Two-dimensional transition metal dichalcogenides: interface and defect engineering. *Chemical Society Reviews*, 47(9), 3100-3128.

[67] Ding, G., Gao, G. Y., Huang, Z., Zhang, W., & Yao, K. (2016). Thermoelectric properties of monolayer MSe_2 (M= Zr, Hf): low lattice thermal conductivity and a promising figure of merit. *Nanotechnology*, 27(37), 375703.

[68] Somvanshi, D., Kallatt, S., Venkatesh, C., Nair, S., Gupta, G., Anthony, J. K., ... & Majumdar, K. (2017). Nature of carrier injection in metal/2-D-semiconductor interface and its implications for the limits of contact resistance. *Physical Review B*, 96(20), 205423.

[69] Couto, W. R. M., Miwa, R. H., & Fazzio, A. (2017). Tuning the p-type Schottky barrier in 2-D metal/semiconductor interface: boron-sheet on $MoSe_2$, and WSe_2. *Journal of Physics: Condensed Matter*, 29(40), 405002.

[70] Li, X., Zhao, W., Cao, Y., Zhu, Z., Song, J., Bang, D., ... & Yu, N. (2009, September). Pathfinding for 22 nm CMOS designs using predictive technology models. *In 2009 IEEE Custom Integrated Circuits Conference* (pp. 227-230). IEEE.

[71] Li, Y., Duerloo, K. A. N., Wauson, K., & Reed, E. J. (2016). Structural semiconductor-to-semimetal phase transition in two-dimensional materials induced by electrostatic gating. *Nature communications*, 7(1), 1-8.

[72] Poblenz, C., Waltereit, P., Rajan, S., Heikman, S., Mishra, U. K., & Speck, J. S. (2004). Effect of carbon doping on buffer leakage in AlGaN/GaN high electron mobility transistors. *Journal of Vacuum Science & Technology B: Microelectronics and Nanometer Structures Processing, Measurement, and Phenomena*, 22(3), 1145-1149.

[73] Martins, R., Nathan, A., Barros, R., Pereira, L., Barquinha, P., Correia, N., ... & Fortunato, E. (2011). Complementary metal oxide semiconductor technology with and on paper. *Advanced Materials*, 23(39), 4491-4496.

[74] Hosoi, Y., Tamai, Y., Ohnishi, T., Ishihara, K., Shibuya, T., Inoue, Y., ... & Inoue, I. H. (2006, December). High speed unipolar switching resistance RAM (RRAM) technology. *In 2006 International Electron Devices Meeting* (pp. 1-4). IEEE.

[75] Lee, H. Y., Chen, P. S., Wu, T. Y., Chen, Y. S., Wang, C. C., Tzeng, P. J., ... & Tsai, M. J. (2008, December). Low power and high speed bipolar switching with a thin reactive Ti buffer layer in robust HfO_2 based RRAM. *In 2008 IEEE International Electron Devices Meeting* (pp. 1-4). IEEE.

[76] Balamurugan, N. B., Sankaranarayanan, K., & John, M. F. (2009). 2-D transconductance to drain current ratio modeling of dual material surrounding gate nanoscale SOI MOSFETs. *Journal of Semiconductor Technology and Science*, 9(2), 110-116.

[77] Wessely, P. J., Wessely, F., Birinci, E., Riedinger, B., & Schwalke, U. (2013). In Situ CCVD Grown Graphene Transistors with Ultra-High On/Off-Current Ratio in Silicon CMOS Compatible Processing. *In Advances in Science and Technology* (Vol. 77, pp. 258-265). Trans Tech Publications Ltd.

[78] Panda, S., Dash, S., Behera, S. K., & Mishra, G. P. (2016). Delta-doped tunnel FET (D-TFET) to improve current ratio and ON-current performance. *Journal of Computational Electronics*, 15(3), 857-864.

[79] Xia, F., Farmer, D. B., Lin, Y. M., & Avouris, P. (2010). Graphene field-effect transistors with high on/off current ratio and large transport band gap at room temperature. *Nano letters*, 10(2), 715-718.

[80] Liu, H., & Peide, D. Y. (2012). Dual-Gate MOSFET With Atomic-Layer-Deposited as Top-Gate Dielectric. *IEEE electron device letters*, 33(4), 546-548.

[81] Lemme, M. C., Li, L. J., Palacios, T., & Schwierz, F. (2014). Two-dimensional materials for electronic applications. *MRS Bulletin*, 39(8), 711-718.

[82] Jhan, Y. R., Thirunavukkarasu, V., Wang, C. P., & Wu, Y. C. (2015). Performance evaluation of silicon and germanium ultrathin body (1 nm) junctionless field-effect transistor with ultrashort gate length (1 nm and 3 nm). *IEEE Electron Device Letters*, 36(7), 654-656.

[83] Generalov, A. A., Andersson, M. A., Yang, X., Vorobiev, A., & Stake, J. (2017). A 400-GHz graphene FET detector. *IEEE Transactions on Terahertz Science and Technology*, 7(5), 614-616.

[84] Radisavljevic, B., & Kis, A. (2013). Mobility engineering and a metal–insulator transition in monolayer MoS_2. *Nature materials*, 12(9), 815-820.

[85] Sanuki, T., Oishi, A., Morimasa, Y., Aota, S., Kinoshita, T., Hasumi, R., ... & Sunouchi, K. (2003, December). Scalability of strained silicon CMOSFET and high drive current enhancement in the 40 nm gate length technology. *In IEEE International Electron Devices Meeting 2003* (pp. 3-5). IEEE.

[86] Yu, S., Wu, X., Wang, Y., Guo, X., & Tong, L. (2017). 2-D materials for optical modulation: challenges and opportunities. *Advanced Materials*, 29(14), 1606128.

[87] Rao, S. M., Lyons, A., Roger, T., Clerici, M., Zheludev, N. I., & Faccio, D. (2015). Geometries for the coherent control of four-wave mixing in graphene multilayers. *Scientific reports*, 5, 15399.

[88] Rahman, M. Z., Kwong, C. W., Davey, K., & Qiao, S. Z. (2016). 2-D phosphorene as a water splitting photocatalyst: fundamentals to applications. *Energy & Environmental Science*, 9(3), 709-728.

[89] Fu, J., Yu, J., Jiang, C., & Cheng, B. (2018). gC_3N_4-Based heterostructured photocatalysts. *Advanced Energy Materials*, 8(3), 1701503.

[90] Li, X., Dai, Y., Ma, Y., Han, S., & Huang, B. (2014). Graphene/gC_3N_4 bilayer: considerable band gap opening and effective band structure engineering. *Physical Chemistry Chemical Physics*, 16(9), 4230-4235.

[91] Chen, Y., Tian, G., Shi, Y., Xiao, Y., & Fu, H. (2015). Hierarchical MoS_2/Bi_2MoO_6 composites with synergistic effect for enhanced visible photocatalytic activity. *Applied Catalysis B: Environmental*, 164, 40-47.

[92] McCreery, R. L. (1991). Carbon electrodes: structural effects on electron transfer kinetics. *Electroanalytical chemistry*, 17, 221-374.

[93] Iqbal, S., Pan, Z., & Zhou, K. (2017). Enhanced photocatalytic hydrogen evolution from in situ formation of few-layered MoS_2/CdS nanosheet-based van der Waals heterostructures. *Nanoscale*, 9(20), 6638-6642.

[94] Pan, J., Shang, Y., Yin, J., De Bastiani, M., Peng, W., Dursun, I., ... & Mohammed, O. F. (2017). Bidentate ligand-passivated $CsPbI_3$ perovskite nanocrystals for stable near-unity photoluminescence quantum yield and efficient red light-emitting diodes. *Journal of the American Chemical Society*, 140(2), 562-565.

[95] Lin, K., Xing, J., Quan, L. N., de Arquer, F. P. G., Gong, X., Lu, J., ... & Li, W. (2018). Perovskite light-emitting diodes with external quantum efficiency exceeding 20 per cent. *Nature*, 562(7726), 245-248.

[96] Li, Z., Wang, Y., Ni, Y., & Kokot, S. (2015). A rapid and label-free dual detection of Hg (II) and cysteine with the use of fluorescence switching of graphene quantum dots. Sensors and Actuators B: *Chemical*, 207, 490-497.

[97] Sadasivuni, K. K., Kafy, A., Zhai, L., Ko, H. U., Mun, S., & Kim, J. (2015). Transparent and flexible cellulose nanocrystal/reduced graphene oxide film for proximity sensing. *Small*, 11(8), 994-1002.

[98] Gregoriades, P., Bleris, G. and Stoemenos, J. (1983). Electron diffraction study of the Si_2Te_3 structural transformation. *Acta Crystallographica Section B Structural Science*, 39(4), pp.421-426.

[99] Ploog, K., Stetter, W., Nowitzki, A. and Schönherr, E. (1976). Crystal growth and structure determination of silicon telluride Si_2Te_3. *Materials Research Bulletin*, 11(9), pp.1147-1153.

[100] Haneveld, A., van der Veer, W. and Jellinek, F. (1968). On silicon tritelluride, Si_2Te_3, and alleged phosphorus tritelluride. *Recueil des Travaux Chimiques des Pays-Bas*, 87(3), pp.255-256.

[101] Zwick, U. and Rieder, K. (1976). Infrared and Raman study of Si_2Te_3. *Zeitschrift Physik B Condensed Matter and Quanta*, 25(4), pp.319-322.

[102] Ziegler, K. and Birkholz, U. (1977). Photoelectric properties of Si_2Te_3 single crystals. *Physica Status Solidi* (a), 39(2), pp.467-475.

[103] Bauer, H. and Birkholz, U. (1978). Electrical conductivity of passivated Si2Te3 single crystals. *Physica Status Solidi* (a), 49(1), pp.127-131.

[104] Exsteen, G., Drowart, J., Vander Auwera-Mahieu, A. and Callaerts, R. (1967). Thermodynamic study of silicon sesquitelluride using a mass spectrometer. *The Journal of Physical Chemistry*, 71(12), pp.4130-4131.

[105] Keuleyan, S., Wang, M., Chung, F., Commons, J. and Koski, K. (2015). A Silicon-Based Two-Dimensional Chalcogenide: Growth of Si_2Te_3 Nanoribbons and Nanoplates. *Nano Letters*, 15(4), pp.2285-2290.

[106] Shen, X., Puzyrev, Y., Combs, C. and Pantelides, S. (2016). Variability of structural and electronic properties of bulk and monolayer Si_2Te_3. *Applied Physics Letters*, 109(11), p.113104.

[107] Wu, K. and Cui, J. (2018). Morphology control of Si_2Te_3 nanostructures synthesized by CVD. *Journal of Materials Science: Materials in Electronics*, 29(18), pp.15643-15648.

[108] Wu, K., Chen, J., Shen, X. and Cui, J. (2018). Resistive switching in Si_2Te_3 nanowires. *AIP Advances*, 8(12), p.125008.

[109] Wu, K., Sun, W., Jiang, Y., Chen, J., Li, L., Cao, C., Shi, S., Shen, X. and Cui, J. (2017). Structure and photoluminescence study of silicon based two-dimensional Si_2Te_3 nanostructures. *Journal of Applied Physics*, 122(7), p.075701.

[110] Chen, J., Wu, K., Shen, X., Hoang, T. and Cui, J. (2019). Probing the dynamics of photoexcited carriers in Si_2Te_3 nanowires. *Journal of Applied Physics*, 125(2), p.024306.

[111] Stokes, D. (2008). Principles and Practice of Variable Pressure/Environmental Scanning Electron Microscopy (VP-ESEM).

[112] Lin, M., Wu, J., Liu, X. and Tan, P. (2017). Probing the shear and layer breathing modes in multilayer graphene by Raman spectroscopy. *Journal of Raman Spectroscopy*, 49(1), pp.19-30.

[113] Jie, W., Yang, Z., Bai, G. and Hao, J. (2018). Luminescence in 2-D Materials and van der Waals Heterostructures. *Advanced Optical Materials*, 6(10), p.1701296.

[114] Perkampus, H. H. (2013). UV-VIS Spectroscopy and its Applications. Springer Science & Business Media.

[115] McIntyre, J. D. E., & Aspnes, D. E. (1971). Differential reflection spectroscopy of very thin surface films. *Surface Science*, 24(2), pp.417-434.

[116] Song, J. J., Lee, J. H., & Levenson, M. D. (1978). Picosecond relaxation measurements by polarization spectroscopy in condensed phases. *Physical Review A*, 17(4), p.1439.

[117] Wang, Y., Cong, C., Qiu, C., & Yu, T. (2013). Raman spectroscopy study of lattice vibration and crystallographic orientation of monolayer MoS_2 under uniaxial strain. *Small*, 9(17), pp.2857-2861.

[118] Aslan, O. B., Chenet, D. A., Van Der Zande, A. M., Hone, J. C., & Heinz, T. F. (2016). Linearly polarized excitons in single-and few-layer ReS_2 crystals. *ACS Photonics*, 3(1), pp.96-101.

[119] Zhu, B., Zeng, H., Dai, J., Gong, Z., & Cui, X. (2014). Anomalously robust valley polarization and valley coherence in bilayer WS_2. Proceedings of the National Academy of *Sciences*, 111(32), pp.11606-11611.

[120] Whittig, L. D., & Allardice, W. R. (1986). X-ray diffraction techniques. *Methods of Soil Analysis: Part 1 Physical and Mineralogical Methods*, 5, pp.331-362.

[121] Dietzel, D., Mönninghoff, T., Jansen, L., Fuchs, H., Ritter, C., Schwarz, U. D., & Schirmeisen, A. (2007). Interfacial friction obtained by lateral manipulation of nanoparticles using atomic force microscopy techniques. *Journal of Applied Physics*, 102(8), 084306.

[122] Gusev, A. A., Zehnder, M. M., & Suter, U. W. (1996). Fluctuation formula for elastic constants. *Physical Review B*, 54(1), 1.

[123] Muñoz, R., & Gómez-Aleixandre, C. (2013). Review of CVD synthesis of graphene. *Chemical Vapor Deposition*, 19(10-11-12), pp.297-322.

[124] Li, Y., Wang, F., Tang, D., Wei, J., Li, Y., Xing, Y., & Zhang, K. (2018). Controlled synthesis of highly crystalline CVD-derived monolayer $MoSe_2$ and shape evolution mechanism. *Materials Letters*, 216, pp.261-264.

[125] Wong, S. L., Liu, H., & Chi, D. (2016). Recent progress in chemical vapor deposition growth of two-dimensional transition metal dichalcogenides. *Progress in Crystal Growth and Characterization of Materials*, 62(3), pp.9-28.

[126] Lu, Z., Sun, L., Xu, G., Zheng, J., Zhang, Q., Wang, J., & Jiao, L. (2016). Universal transfer and stacking of chemical vapor deposition grown two-dimensional atomic layers with water-soluble polymer mediator. *ACS nano*, 10(5), pp.5237-5242.

[127] Zhou, D., Shu, H., Hu, C., Jiang, L., Liang, P., & Chen, X. (2018). Unveiling the growth mechanism of MoS_2 with chemical vapor deposition: from two-dimensional planar nucleation to self-seeding nucleation. *Crystal Growth & Design*, 18(2), pp.1012-1019.

[128] Hong, S., Sheng, C., Krishnamoorthy, A., Rajak, P., Tiwari, S., Nomura, K. I., ... & Vashishta, P. (2018). Chemical vapor deposition synthesis of MoS_2 layers from the direct sulfidation of MoO_3 surfaces using reactive molecular dynamics simulations. *The Journal of Physical Chemistry C*, 122(13), pp.7494-7503.

[129] Elliott, J. A., Shibuta, Y., Amara, H., Bichara, C., & Neyts, E. C. (2013). Atomistic modelling of CVD synthesis of carbon nanotubes and graphene. *Nanoscale*, 5(15), pp.6662-6676.

[130] Kwak, J., Thiyagarajan, K., Giri, A., & Jeong, U. (2019). Au-Assisted catalytic growth of Si_2Te_3 plates. *Journal of Materials Chemistry C*, 7(34), pp.10561-10566.

[131] Sun, B., Wang, Z., Liu, Z., Tan, X., Liu, X., Shi, T., . . . Liao, G. (2019). Tailoring of silver nanocubes with optimized localized surface plasmon in a gap mode for a flexible MoS_2 photodetector. *Advanced Functional Materials*, 29(26), 1900541. doi:10.1002/adfm.201900541

[132] Xia, M. (2018). 2-D Materials-coated plasmonic structures for SERS Applications. *Coatings*, 8(4), 137. doi:10.3390/coatings8040137

[133] Lee, H. K., Lee, Y. H., Zhang, Q., Phang, I. Y., Tan, J. M., Cui, Y., & Ling, X. Y. (2013). Superhydrophobic surface-enhanced Raman Scattering Platform fabricated by assembly of Ag nanocubes for Trace Molecular Sensing. *ACS Applied Materials & Interfaces*, 5(21), pp.11409-11418. doi:10.1021/am403655g

[134] Erlandsson, R., Birkholz, U., & Karlsson, S. E. (1978). Study of Si_2Te_3 surface reactions with Auger electron spectroscopy. *physica status solidi* (a), 47(1), pp.85-90.

[135] Rau & Kannewurf (1966). Intrinsic absorption and photoconductivity in single crystal $SiTe_2$. *j. phys. chem. solids* 21, p.1097

[136] Wang, M., Lahti, G., Williams, D., & Koski, K. J. (2018). Chemically tunable full spectrum optical properties of 2-D silicon telluride nanoplates. *ACS nano*, 12(6), pp.6163-6169.

[137] Weiss, A., Weiss, A.Z. *Anorg. Allg. Chem*. 1953,273,124